GEORG-AUGUST-UNIVERSITÄT GÖTTINGEN

II. Physikalisches Institut

Alignment Studies of the ATLAS Silicon Trackers with Overlap Residuals

von

Kathrin Störig

II.Physik-UniGö-Dipl-2008/03

A method for identifying global deformations of the ATLAS Silicon Tracker with overlap residuals has been developed. Both, the robustness of this method for a perfect detector and the sensitivity of overlap residuals on global detector deformations are studied.

Post address:
Friedrich-Hund-Platz 1
37077 Göttingen
Germany

II. Physikalisches Institut
Georg-August-Universität Göttingen
April 2008

GEORG-AUGUST-UNIVERSITÄT

GÖTTINGEN

II. Physikalisches Institut

Alignment Studies of the ATLAS Silicon Trackers with Overlap Residuals

von

Kathrin Störig

II.Physik-UniGö-Dipl-2008/03

Dieser Forschungsbericht wurde als Diplomarbeit von der Fakultät für Physik der Georg-August-Universität zu Göttingen angenommen.

Angenommen am:	25. April 2008
Referent:	Prof. Arnulf Quadt
Korreferent:	Prof. Markus Klute

Preface

The ATLAS experiment is one of four large experiments currently under construction at the Large Hadron Collider (*LHC*) in Geneva, Switzerland. Data-taking of proton-proton-collisions at an initial centre-of-mass energy of 10 TeV is scheduled for 2008.
The ATLAS Inner Detector consists of a Silicon tracking and drift-tube system mainly dedicated to the reconstruction of charged particle tracks. The necessary precision of this tracking system is one of the various requirements to fulfil in order to achieve the ambitious physics goals. Thereby, especially obtaining detailed knowledge about the real detector geometry is crucial (*alignment*). Beside hardware techniques, track-based alignment procedures exist - mainly comparing the differences (*residuals*) between the measured hit position and that of reconstructed tracks.

Various types of global detector deformations are known, which in a simple model can be described as functions of three main parameters, radius R, angle φ and length Z. Among these, there are special classes of deformations, especially radius-dependent ones, which in general are very difficult to identify.

Overlap residuals originate in particles hitting the edge (or overlap) regions of two neighbouring silicon sensors. This direct distance measurement of neighbouring modules on the same layer results in a special sensitivity to the detector circumference, granting access to certain types of detector deformations which influence the module's distances and which are difficult to detect with the conventional approaches. Thus, overlap residuals are introduced as add-on.

In this thesis, overlap residuals will be defined both for the Semiconductor Tracker and the Pixel detector. Their behaviour at nominal geometry will be explored from different points of view - including several detailed studies concerning e.g. Lorentz-drift and -correction, diffusion and geometrical aspects. Finally, the method of overlap residuals is applied to identify and distinguish global weak deformations.

Chapter 1 gives a short introduction to the *Standard Model of Particle Physics* and today's physics challenges.

In Chapter 2 a short overview of the particle accelerator LHC and a detailed description of the ATLAS experiment is presented with an emphasis on its Inner Detector and the Silicon trackers.

Chapter 3 introduces the technical details of the alignment procedure and especially global detector deformations. Overlap residuals are introduced as examination tool and their expected impact on the alignment with respect to the global deformations is discussed.

In Chapter 4, the characteristics of overlap residuals at nominal geometry are studied both with analytical methods and toy Monte Carlos. Possible reasons for the discrepancies between naive theoretical expectations and the actual overlap residual behaviour are discussed.

The impact of global deformations on overlap residuals is presented in Chapter 5. Typical observables are chosen to point out the sensitivity of overlap residuals.

Conclusions are drawn in Chapter 6. Finally, an outlook on possible future developments is given.

Contents

1. Introduction

1.1. The Standard Model of Particle Physics

The Standard Model of Particle Physics (*SM* [1–3]) might be one of the most successful theories in history. It is a quantum field theory based on the symmetry groups $SU(3)_C \times SU(2)_L \times SU(1)_Y$. Further details can be found e.g. in [4]. From today's standard of knowledge the Universe consists of twenty-four fermions and thirteen bosons with the SM arranging them into different groups according to their spin (cf. Figure 1.1). The fermions (spin-$n/2$-particles, n odd integer), which all matter consists of, show a well defined structure: they split into $3 \times 3 \times 2$ quarks and 3×2 leptons. They are grouped pairwise in *electro-weak doublets*. There are three similar manifestations of each doubled (*family* or *generation*). Furthermore, the quark-doublet of each family exists in three different colours: red, green and blue.

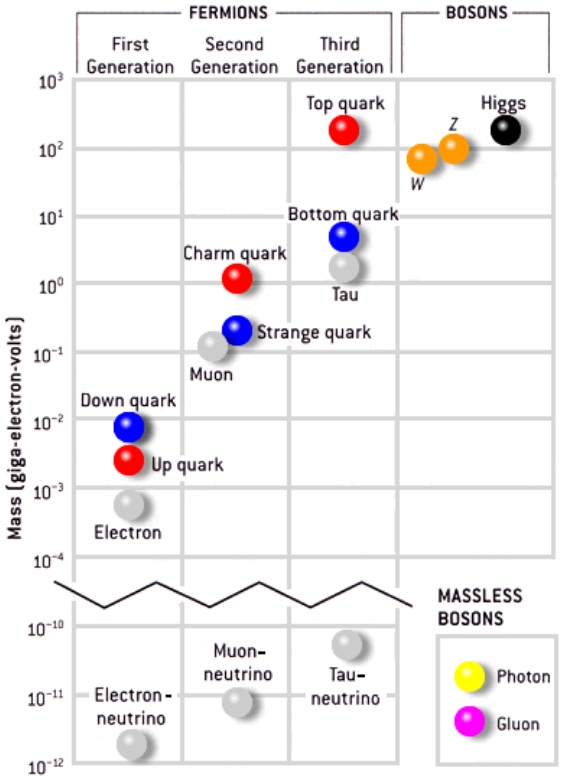

Figure 1.1.: Particle content of the Standard Model of Particle Physics [5]. With higher generation, particle masses increase significantly, both for quarks and leptons. Only the absolute neutrino mass hierarchy has not been confirmed yet.

The first and lightest family is build by the up-quark (u), the down-quark (d), the electron (e^-) and the electron-neutrino (ν_e). All stable matter is made of these particles, e.g. uud form a proton, udd a neutron. Protons, neutrons and electrons finally combine to atoms, atoms to molecules, molecules to solid state bodies. The second family is given by the charm-quark (c), the strange-quark (s), the muon (μ) and the muon-neutrino (ν_μ). Outside of experiments, muons can be found mainly in cosmic radiation. The masses of these particles are higher than the ones of particles from the first generation - these particles have a limited life time and decay into particles of the first family. Finally there is the third generation with the top-quark (t), the bottom-quark (b), the tau (τ) and the tau-neutrino (ν_τ), which are again heavier than the particles of the second generation. But no law for this increasing mass hierarchy has been found yet. Moreover, many orders of magnitude lay between the heaviest particle (the t-quark mass of 175 GeV reaches nearly the mass of an Au-atom) and the lightest ones (neutrinos are nearly massless, $O(< 1\text{ eV})$).
Within a family, the quarks assigned to the upper place carry a charge of $+2/3\ e^-$, the lower ones one of $-1/3\ e^-$. Similar in the lepton sector: the charged leptons carry a charge of $1 \cdot e^-$ and finally the neutrinos are electrically neutral. Additionally an anti-particle exists for every fermion with exactly the same properties besides a complementary sign of electrical charge. In their first encounter, a particle and the corresponding anti-particle annihilate.

The bosons (spin-n-particles, n integer) are thought of as the carriers of the four fundamental forces:

- The *strong force* is mediated by eight gluons (g), which hold together both the quarks as mesons (quark-pairs) and baryons (quark-triplets) as well as the protons and neutrons as nuclei. Its range is limited to about 10^{-15} m.

- The *electromagnetic force* is mediated by the photons (γ), known from Coulomb-force, light, magnetism etc. It is about 137 times weaker than the strong force, but its range is unlimited.

- The *weak force* is mediated by the $W^{+/-}$ and the neutral Z bosons. It is responsible e.g. for the β-decay of a neutron, the radioactive β-decay in general and nuclear fusion in the sun. It is 10^5 times weaker than the electromagnetic force and has a range of about 10^{-18} m.

- *Gravitation*, which is not part of the SM. Yet a further boson is predicted as mediator of the gravitational force: the graviton (G). The range of the gravitational force is unlimited but it is 10^{33} times weaker than the weak force.

In an energy range of about (80-90) GeV/c^2, the electromagnetic and the weak force unite to the *electroweak* force.

A special role is adopted by the Higgs-boson [6–8]. According to the SM, all vector bosons are considered to be massless. Nevertheless, $W^\pm$- and Z-bosons have a mass about 80 to 90 GeV/c^2, which can not be neglected. One possible explanation for the origin of masses of the particles is the Higgs mechanism. Mass could be the result of the interaction of particles with a so called Higgs background field. - This part of theory seems very elegant and fits in the concepts of the SM very well - yet, no Higgs boson has been discovered and this theory still needs to be proved.

1.2. Shortcomings of the Standard Model

The SM is very comprehensive, not only can many parameters be predicted by the SM with astonishing precision (millionth percent) but also have by then unknown particles been found because of its precise predictions. Nevertheless, the SM has its shortcomings.

- The SM contains various free parameters which can not be predicted but must be measured, such as particle masses, strengths of interactions etc.
- Exactly three generations of particles are known, both for leptons and quarks, although no direct relationship between the two groups can be found. Furthermore, all known matter is build up of the first generation exclusively.
- The mass hierarchy of fermions reaches from a few eV (neutrinos) up to atom's weight (top-quark). Nevertheless the SM does not contain any explanation for this huge mass range.
- The electron charge completely balances the charge of a proton, being build up of various quarks and gluons. Besides, protons belong to baryons while electrons are leptons.
- Neutrinos are very special, their flavour can oscillate in time and their mass is many orders of magnitude smaller than other particles, yet they are not massless.
- In the early Universe the formation of a symmetric amount of matter and antimatter is expected. Yet, today a severe asymmetry between matter and antimatter exists, as the Universe is purely made of matter. Although processes with a small asymmetric production of matter and anti-matter are known there is still a large amount of anti-matter missing.
- From precise gravitational and astrophysical measurements it is known, that the Universe must consist of more matter than observed. From its expansion similar conclusions can be drawn concerning energy. This *dark matter* and *dark energy* represents about 96% of the Universe.
- In the SM, the electromagnetic and the weak force can be unified at $O(100)$GeV, but is a further unification with the strong force possible (*Grand Unified Theory*)? The extrapolation of forces at high energies leads to similar results, yet it does not show a unification of all three forces in a certain point, while e.g. for SM extensions this could be achieved.
- Gravitation needs to be included in SM, of which still no quantum field theory exists. Could the gravitational force even be united with the other three forces at higher energies (*Theory of Everything*)?

With respect to these unanswered questions, various extensions of the SM have been proposed. Super symmetry (*SUSY*, [9, 10]) establishes an elementary symmetry between matter and forces thus, that a super-symmetrical partner is predicted for every SM particle: a fermion gets a boson and vice versa. Many variations of this theory exist: the minimal super-symmetric SM (*MSSM*), mSugra etc. Extra dimensions [11] could explain the weakness of the gravitational force, as these might be reserved for gravitons exclusively.
Just as well as different Higgs models or a substructure of fermions might be possible.

2. Experimental Setup

2.1. The Large Hadron Collider

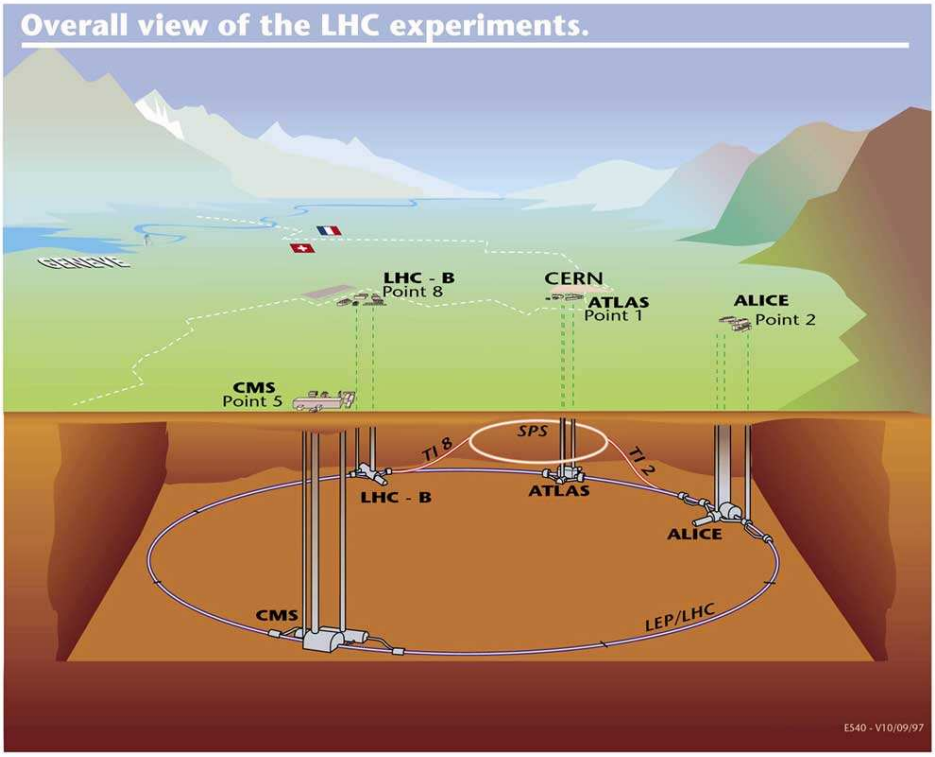

Figure 2.1.: Scheme of the Large Hadron Collider [12]: The accelerator tunnel with its four main experiments Alice, ATLAS, CMS and LHC-b, situated beneath the outskirts of Geneva, between the Alps, the Jura and the Lake Geneva

The Large Hadron Collider (*LHC*) [13–15] at CERN [16], the European Organization for Nuclear Research, is designed for proton-proton collisions at a centre-of-mass energy of 14 TeV. Its planning began in 1984 - anticipatory many of the open questions which arose in the following years (cf. Section 1.2).

During the following years, technical proposals for various magnets, cavities, detectors etc. were examined, approved and then prototypes were developed to show the feasibility of this project before starting the serial production. Finally, after the shutdown of LEP [17, 18] in November 2000, the LEP tunnel could be freed and the installation process for LHC really started.

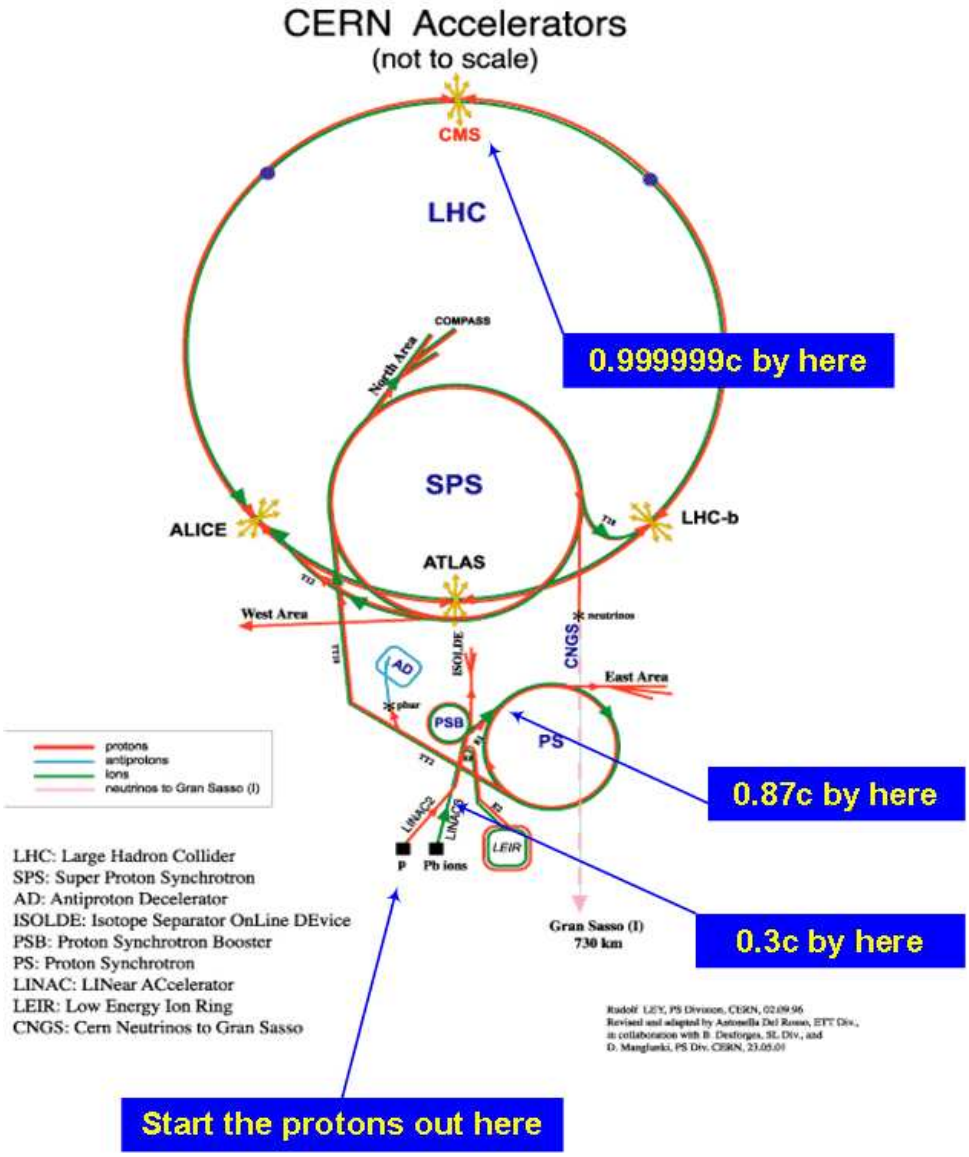

Figure 2.2.: The CERN accelerators [12]. After proton generation, the beam is accelerated in several steps, until it is injected into the LHC ring for collisions.

Geographically, the LHC is situated close to Geneva, Switzerland, between the Lake Geneva, the Alps and the Jura Mountains - in the old twenty-seven kilometre circular LEP underground tunnel in a depth of 75 to 120 metres.
Two counter rotating proton beams (cf. Figure 2.2) are injected from the SPS into two separated beam pipes, located within the same supporting structure, with a nominal energy of 450 MeV. Eight radio frequency cavities per beam with a maximum field strength of about 5.5 MV/m accelerate the protons by alternating magnetic fields to a nominal energy of 7 TeV. A total number of 9,300 magnets with magnetic fields up to 8.33 Tesla are needed to keep the protons inside the evacuated beam pipe: 1,232 dipole magnets, designed to combine the opposite magnetic fields into one magnet bend the trajectories, 858 quadrupole magnets take care of a precise

focusing and 6,208 additional magnets correct small deviations of the beam profile.
A large cryogenic system keeps the operating temperature of the whole accelerator beneath 1.9 K - LHC is the first accelerator completely cooled - as only superconducting [19] magnets can fulfil the enormous requirements concerning the magnetic field strength. Furthermore, the LHC is also designed to collide beams of heavy ions, such as lead, with a maximum total collision energy of $1,250$ TeV- this is about twenty-eight times higher than at the Relativistic Heavy Ion Collider (RHIC) at Brookhaven Laboratory, USA.

The proton beams collide in the four locations of the four main experiments:

- ATLAS [20–22] (*A Toroidal LHC ApparatuS*) and CMS [23–25] (*a Compact Muon Solenoid*) are multi-purpose detectors.
- Alice [26] (*A Large Ion Collider Experiment*) will search for a quark-gluon-plasma in heavy ion collisions - a state where the confinement of quarks and gluons shall be overcome.
- LHC-b [27, 28] (*the Large Hadron Collider Beauty experiment*) concentrates on high-precision measurements concerning b-physics.
- The measurements will be rounded off by two smaller experiments called LHC-f [29, 30], a forward detector for ATLAS, and TOTEM [31, 32] (*Total Cross Section, Elastic Scattering and Diffraction Dissociation at the LHC*), associated with CMS in a joint diffractive/forward physics range.

Typically, a bunch crossing rate of 40 MHz with about 10^{11}protons per bunch will lead to roughly 1 billion proton-proton collisions. This corresponds to a design luminosity of

$$\mathcal{L} = 10^{34}\ \mathrm{cm}^{-2}\mathrm{s}^{-1}$$

After several steps of preselection, done by the *Trigger*, the produced amount of data reaches manageable dimensions. About 100 events per second, each event representing a few hundred MB, result in a final rate of 1 GB/s in total. Considering the normal operation time of the LHC one can extrapolate the amount of data produced in one year to 15 PB (15 *million* GB), including the raw, preprocessed and simulated data.

In order to cope with this quantity of data, which not only needs to be stored safely but also has to be distributed within the community for analyses, a new development for computing has been pushed, the so called *GRID*. The LHC Computing Model [33] divides the GRID into a hierarchical structure, split in four different levels.
The first level, called *Tier-0*, is located at CERN, as it is the source of data. Copies of the data will be distributed to a dozen major national computing centres (*Tier-1*), which will be supplemented by regional *Tier-2*-centres, in total over 130 in research labs and universities, distributed in 31 countries around the world. The analyses done by the physicists shall be done mainly by the *Tier-3*-centres, the lowest and most local level in this structure, while tasks of main interest, such as alignment and a first reconstruction of the data is reserved to the upper levels. To conclude, this LHC Computing Grid project (*LCG*) currently operates the world's largest scientific Grid, including more than 10,000 CPUs and several PB of storage.

2.2. The ATLAS Detector

ATLAS (*A Toroidal LHC ApparatuS*)[20–22, 34] is the largest of the LHC experiments: it has a height of 25 meters and a length of 46 meters with a weight of 7,000 tons.

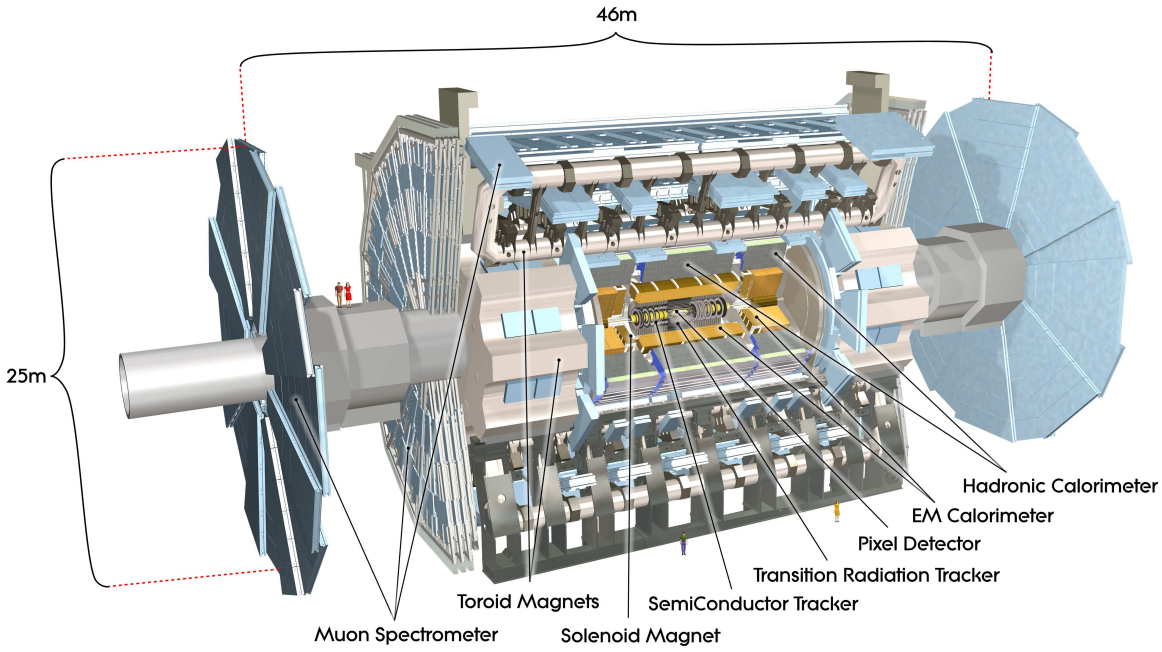

Figure 2.3.: The different sub-detectors of ATLAS[12]: innermost a precise tracking system, in the middle the electromagnetic and hadronic calorimeters and outermost the muon chambers. The tracking system is surrounded by a solenoidal magnetic field while the muon chambers are placed between toroidal magnets.

ATLAS has a typical onion-like structure like most multipurpose detectors (cf. Figure 2.3). The innermost part is a precise tracking system consisting of three sub-detectors: *Pixel, Semiconductor* and *Transition Radiation Tracker*. It is surrounded by a *solenoid magnet* bending tracks of charged particles in the transverse plane and therefore allowing a measurement of their transverse momentum. The *calorimeters* are situated in the middle. Electrons and photons are to be measured precisely and stopped in the *electromagnetic* calorimeter, while the *hadronic* one is dedicated to the detection of hadrons. Also muons deposit a small amount of their energy in both calorimeters. The outermost part of ATLAS is represented by different types of *muon chambers*. They are located in the spaces between a large *toroidal magnet* providing a second and from the Inner Detector independent measurement of the muon momentum.

2.2.1. Required Performance

A set of global requirements for the detector performance can be derived (cf. Table 2.1) from the ambitious physics goals as well as technical needs (high interaction rates, particle multiplicities, -energies and radiation doses). The search for the SM Higgs defines only one of the various levelling bars.

- Coverage in pseudorapitiy η (cf. Equation 2.1) needs to be as high as possible for a minimum loss of particles in the forward region.
- A very good momentum resolution of charged particles is essential in the inner trackers such as a high reconstruction efficiency.
- Due to a very high particle density especially near the beam pipe, a very high granularity must be combined with a fast read-out and radiation hardness, both for sensors and for on-detector electronics.
- Also the calorimeters have to be excellent. Electron and photon identification are most important for the electromagnetic part while for the hadronic part accurate measurements of jets and missing transverse energy are indispensable together with a full η coverage.
- The muon spectrometer has to determine the charge and transverse momentum of muons over a wide range of momenta independently from the inner trackers.
- The trigger needs to reliably reduce the enormous data rates to a manageable level.

Detector component	Required resolution	η coverage	
		Measurement	Trigger
Tracking	$\sigma_{p_T}/p_{\mathrm{T}} = 0.05\%\ p_{\mathrm{T}} \oplus 1\%$	± 2.5	
EM calorimetry	$\sigma_E/E = 10\%/\sqrt{E} \oplus 0.7\%$	± 3.2	± 2.5
Hadronic calorimetry			
barrel and end-cap	$\sigma_E/E = 50\%/\sqrt{E} \oplus 3\%$	± 3.2	± 3.2
forward	$\sigma_E/E = 100\%/\sqrt{E} \oplus 10\%$	$3.1 < \lvert\eta\rvert < 4.9$	$3.1 < \lvert\eta\rvert < 4.9$
Muon spectrometer	$\sigma_{p_T}/p_{\mathrm{T}} = 10\%$ ($at\ p_{\mathrm{T}} = 1$ TeV)	± 2.7	± 2.4

Table 2.1.: Performance goals of the ATLAS detector [34]. Both, momenta and energies are measured in GeV.

2.2.2. Coordinate Frames

The ATLAS global coordinate frame forms a right-handed coordinate system (cf. Figure 2.4) [35]. The x-axis points from the detector vertex towards the centre of the LHC ring and is denoted *GlobalX*. *GlobalY* is directed skywards with an inclination about 1.23°. *GlobalZ* is aligned parallel to beam axis. *End Cap A* is situated in positive z direction, while *End Cap C* entitles the opposite side.

Digit	Value Range Pixel	Value Range SCT	Meaning / Comment
ID1	2	2	Inner Detector
ID2	1	2	detector type
ID3	0	0	barrel
	-2, 2	-2, 2	negative, positive end cap
ID4	[0;2]	[0,3]	layer number
	[0,2]	[0,8]	disc number
ID5 "module-φ"	[0,21]	[0,31]	barrel layer 0
	[0,39]	[0,39]	barrel layer 1
	[0,55]	[0,47]	barrel layer 2
	-	[0,55]	barrel layer 3
	[0,53]	-	end caps 0 - 2
	-	[0,51]	end caps at $ID6 = 0$
	-	[0,39]	end caps at $ID6 \in [1,2]$
ID6 "module-η"	[-6,6]	[-6,6]\{0}	barrel module-η
	0	-	end caps have only one ring
	-	[0,1]	end cap 0
	-	[0,2]	end cap [1,5]
	-	[0,1]	end cap [6,7]
	-	0	end cap 8
ID7	[0;327]	[0,1]	φ-channel / inner/outer wafer
ID8	[0;143]	[0,767]	η-channel / strip number

Table 2.2.: The ATLAS identifiers for the Silicon trackers[36].

GlobalX and GlobalY span the transverse plane in which e.g. the transverse momentum, p_{T}, and the missing transverse energy, $\not{E}_T$, are defined. *Global*φ corresponds to a rotation around GlobalZ in the transverse plane. Globalϑ is measured with respect to the beam pipe inside the longitudinal *R-Z* detector plane. Finally, the pseudo-rapidity η is given by

$$\eta = -\ln \tan \vartheta/2. \tag{2.1}$$

Furthermore, several local coordinate frames exist, whereas only the *Reconstruction local frame for Inner Detector* [35] is presented here. The origin of this coordinate frame is situated at a module's centre of gravity. *LocalX* is defined in the more sensitive direction of the module. For the Semiconductor tracker this is perpendicular to the strips while for the Pixel detector this is along the short side of the pixels. *LocalY* is rectangular to LocalX and is also situated in the module plane. *LocalZ* completes the right-handed coordinate frame, e.g. for barrel modules, it points outwards away from the vertex.

All parts of the ATLAS detector have a unique eight-column identifier, the so called *AtlasID* [36]. The following specifications refer to the Silicon trackers (cf. Table 2.2).
The first digit identifies the Inner Detector (*"2"*), the second one distinguishes between Pixel (*"1"*) and SCT (*"2"*). The third one indicates barrel (*"0"*) or end caps (*"±2"*) and the fourth one marks the layer or disc number. The fifth one represents the φ-coordinate of the module and the sixth one its η-coordinate. For Pixels, the seventh and eighth ones describe the channel numbers in φ and η, while for the SCT, the wafer side and the strip number are coded.

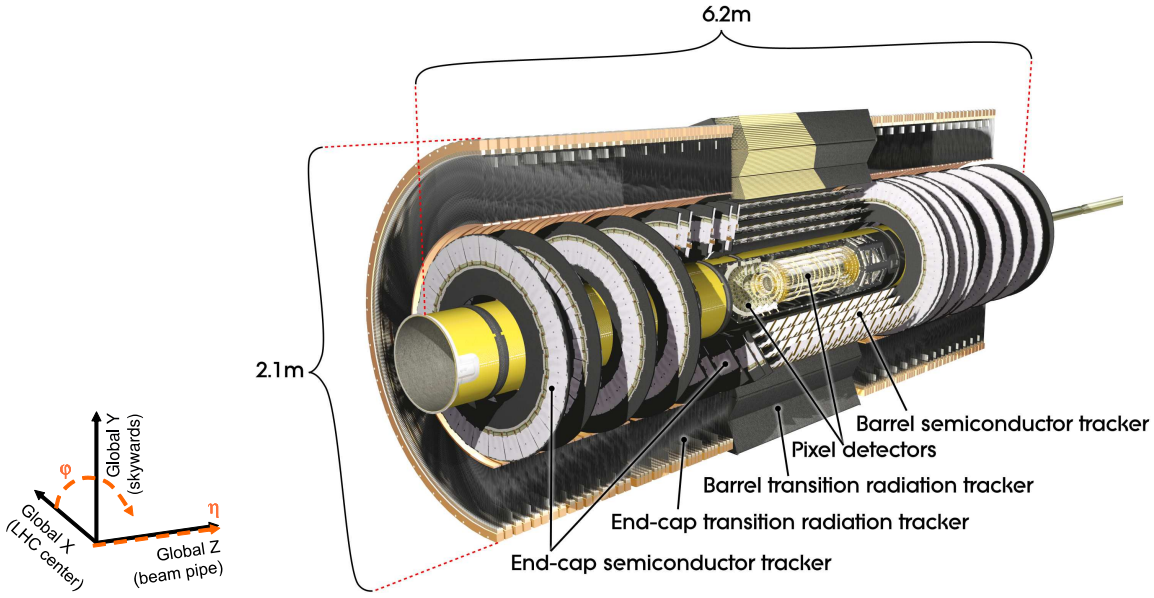

Figure 2.4.: The ATLAS Inner Detector is divided into three sub-detectors. The beam pipe is surrounded by the Pixel Detector, followed by the Semiconductor Tracker, then the Transition Radiation tracker which allows to distinguish between pions and electrons. The ATLAS global coordinate frame is shown on the left side.

2.2.3. The ATLAS Inner Detector

The main purpose of the Inner Detector (*ID*,[34, 37, 38]) is a precise measurement of the transverse momentum and a reliable identification of secondary vertices. Thus, not only the distance between measured hits and the primary vertex is essential but also the number and quality of each single hit.

The Solenoidal Magnet

The tracking system is placed inside a solenoidal magnetic field parallel to the beam axis. The magnet [34, 39, 40] is made out of a superconducting coil. It has an axial field strength of 1.998 T at a nominal current of 7.730 A, an operation temperature of 4.5 K and consists of 9.2 km high-strength Al-stabilised NbTi conductors. The length of the magnet is 5.8 m. Its radius is about 2.5 m and the coil mass is 5.4 t. The adjacent calorimeters serve as support, i.e. the steel of the hadronic calorimeter serves as flux return and the coils vacuum vessel is shared with the electromagnetic calorimeter.

The Pixel detector

About 1000 tracks per event are expected within an $|\eta|$-range of 2.5. Thus, a fine granularity is essential in particular for the vertex detector. Both, Pixel and silicon micro-strip tracker (*SCT*) are arranged in concentric cylinders (cf. Figure 2.4) parallel to the beam axis. The end cap discs are perpendicular to the beam pipe on both sides.

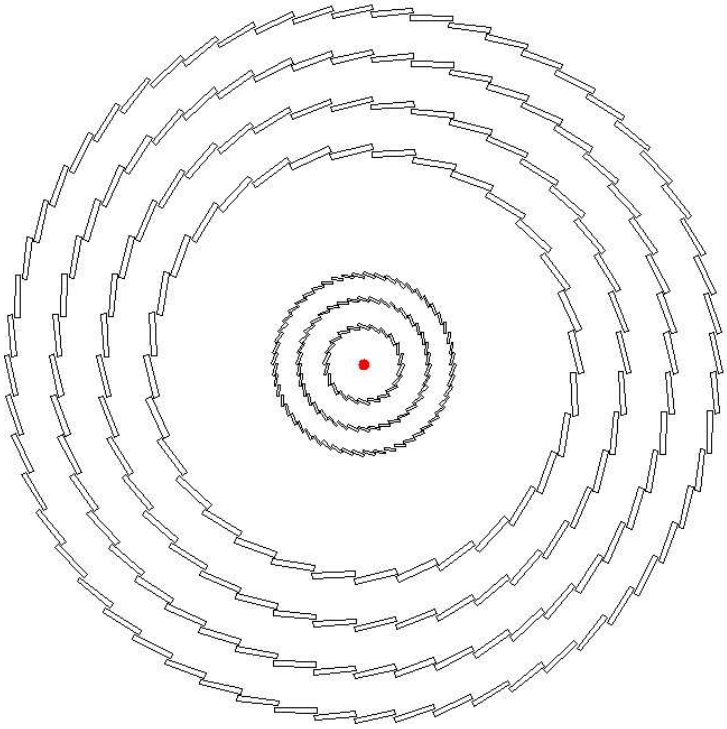

Figure 2.5.: View of the silicon detector geometry [41] in the R-φ-plane. The inner three layers belong to the Pixel detector. Its innermost layer has a radius of 5 cm. The outer four layers belong to the SCT, the outermost layer has a radius of about 55 cm. Modules are arranged with a small overlap in the R-φ-plane. The inclination α of Pixel and SCT modules is directed oppositely.

The Pixel detector [42] consists of 1,744 identical modules. The minimum pixel size is $50 \times 400\ \mu\text{m}^2$. In total, there are about 80.4 million readout channels.
The modules are arranged into three barrel layers and 2×3 end cap discs, grouped in staves (modules with identical module-φ) in the barrel region and segments in the disks. The pixel staves (cf. Figure 2.5) are mounted on the barrel support structures with a tilt angle α of $+20°$ between the module and a barrel tangential vector. Two neighbouring staves overlap about 1 mm in R-φ direction in order to ensure full coverage.

The pixel sensors consist of oxygenated n-type wafers with an n+ doping on the read-out side and a p-type back contact. They have a thickness of 250 μm and their intrinsic resolution is $17 \times 115\ \mu\text{m}^2$ in $(R - \phi) \times z$.
From bottom upwards, a module (cf. Figure 2.6) consists of 16 front-end electronics chips, each with 2,880 channels, adding up to 46,080 readout-channels per module with respect to the *ganged and inter-longed pixels*. Due to a necessary gap between adjacent read-out chips, four pixels per column are sharing a readout-channel with a middle pixel (*ganged pixels*). In a row, there are several *longer* pixels (cf. Figure 2.7).

The read-out chips are bump-bonded via small In- or PbSn balls to the surface of the $63.4 \times 24.4\ \text{mm}^2$ sensor, which is mounted on a flexible circuit board containing the module-control chip (*MCC*). The read-out chips perform the following steps: amplification, subtraction

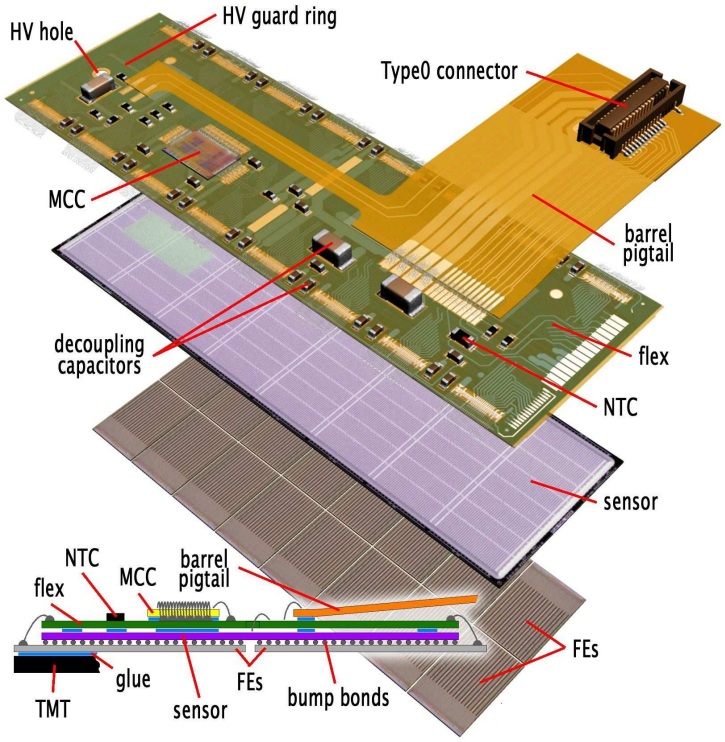

Figure 2.6.: Schematics of a Pixel module The active silicon, split up in 328 × 144 channels, is bumb-bonded via small In- or PbSn-balls to the *time-over-threshold*-readout-chips.

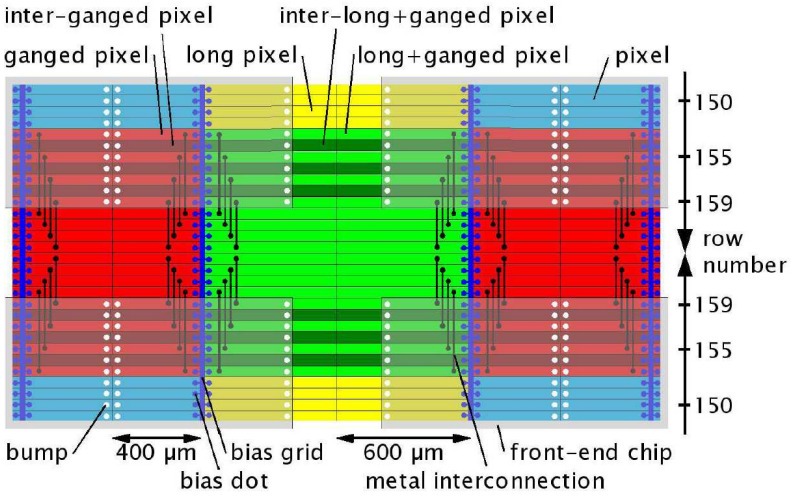

Figure 2.7.: Layout of a Pixel module [43]. In the intersection between adjacent read-out chips, the pixels are longer, respectively two pixels share one read-out channel.

of the leakage current, signal shaping and threshold discrimination. Finally the time over a certain threshold is forwarded with a time-stamp to the module-control chip. The MCC collects the signals and transmits them to the global read-out system.
The modules are mounted onto the support structure such that the sensor side faces the beam line. In order to enhance the performance the best modules were placed in barrel layer 0.

The Semiconductor Tracker

The silicon micro-strip detector (*SCT*) is built up of 4,088 modules, where each is a combination of two single-sided parts. The modules are arranged in four barrel layers and 2×9 disks on each side, providing about four three-dimensional space points per track.
The average strip pitch of the rectangular modules in the barrel region is 80 μm leading to a intrinsic resolution of 17 μm in R-φ direction and 570 μm in z-direction. The strips of the trapezoidal modules in the end cap region have a slightly different pitch of 47-96 μm leading to an intrinsic resolution of again 17 μm in R-φ-direction and 570 μm in radial direction. The SCT covers an area of 63 m^2 active silicon and has approximately 6.3 million read-out channels. Analogue to the Pixel tracker the modules are grouped in segments building discs and in staves for barrel (cf. Figure 2.5)- with a tilt angle α of $-10°$ between the module surface and a barrel tangential vector. A significant overlap between neighbouring staves provides a maximum detector coverage and a minimum of geometrical holes.

Considerations of costs and reliability lead to the chosen classic single-sided design of p-in-n silicon with binary AC-coupled readout-strips which are mounted on the back of each other with a small tilt angle of 40 mrad. In the barrel region, alternating the inner or outer wafer of the modules is aligned parallel to the beam pipe. On the discs always one wafer of the module is aligned radially.
A sensor thickness of (285 ± 15) μm silicon leads to an initial bias voltage of 150 V in order to keep the sensor fully depleted. During runtime, this voltage needs to be increased up to 450 V because of radiation damage.

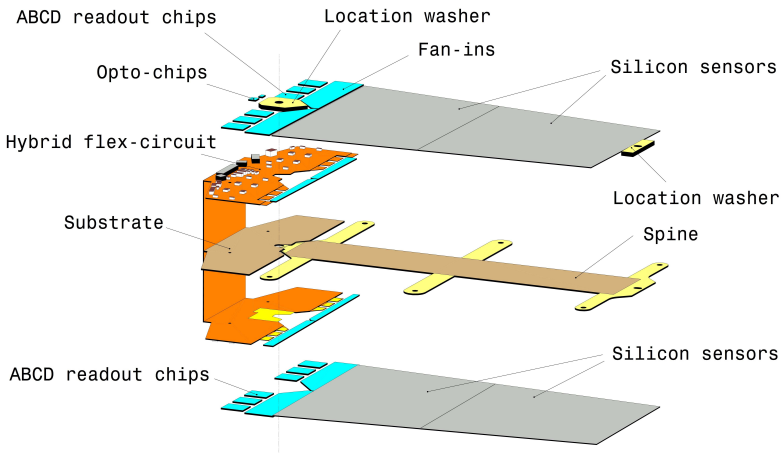

Figure 2.8.: Schematics of an SCT module: The active silicon is split up into 768 strips.

The design of an SCT module is shown in Figure (2.8). Mechanical and thermal stability is guaranteed by a 380 μm thick thermal pyroliticgraphite (*TPG*) base board on which four sensors are mounted. Two of them are located both at the top and bottom side with a stereo angle of

±20 mrad against the module's geometrical centre. These are bridged via a polyamidal hybrid with a carbon-fibre substrate. The high-voltage is supplied via the conducting base-board. The two sides, each divided into 770 strips, 768 active strips plus one on each side additional to define a bias potential, finally build the 12.8 cm long module. The charge is collected in the strips, then the signal is amplified, shaped and discriminated. Finally, the signal is forwarded binary to the global read-out system: "1" corresponds to a hit (signal over threshold) and "0" to none.

The Transition Radiation Tracker

In addition to the high-precision hits delivered by the silicon trackers, the transition radiation tracker (*TRT*) provides slightly different information for an overall robust pattern recognition: it offers a large number of one-dimensional R-ϕ hits (typically 36) per track with an intrinsic resolution of 130 μm. The TRT hit information improves the momentum resolution in the transverse plane. Additionally, the transition radiation signal allows to distinguish between electrons and pions as the amount of transition radiation depends on the mass of the particle.
In the barrel region the TRT consists of 4 mm diameter straw tubes filled with a xenon-based gas mixture, orientated parallel to the beam pipe. The barrel is split up nearly in the middle of the 144 cm long straws. It covers a region of $|\eta| \leq 2$. The end cap design differs slightly from the barrel, as the shorter straws are aligned radially. The TRT consists of approximately 351,000 readout-channels.

2.2.4. The ATLAS Calorimeters

For the ATLAS calorimeters (cf. Figure 2.9) different technologies were chosen according to the requirements concerning physics interests and radiation hardness [44, 45]. The goal is an energy measurement with the highest possible precision.
The electromagnetic calorimeter is a liquid-argon sampling calorimeter, placed outside the solenoidal magnet. It has a very high granularity and a good performance, both for energy and position resolution. It supplements perfectly the precision measurements of the Inner Detector. For the rest of the calorimeter a coarser granularity is sufficient, especially due to a higher particle density in the forward region and relatively lower requirements for the measurement of jets and $\not\!\!E_T$. In the barrel region the hadronic calorimeter consists of three scintillator-tile cylinders - a big one in the middle extended by a smaller part on each side. However, the end caps are also designed with liquid argon technology. A combined forward calorimeter extends up to $|\eta| \leq 4.9$.

One of the main challenges for the calorimeters is given by a good energy resolution and jet containment. The radiation length is a good indicator for the effective thickness of a calorimeter, as it shows the distance in which the particle's energy is reduced by factor e. The larger the radiation length, the less punch-throughs into the muon systems. The EM calorimeter has a total thickness of more than 22 radiation lengths while for the hadronic calorimeters nearly 10 radiation length suffice. In combination with the high η-coverage of the whole system a good $\not\!\!E_T$-measurement is achieved.

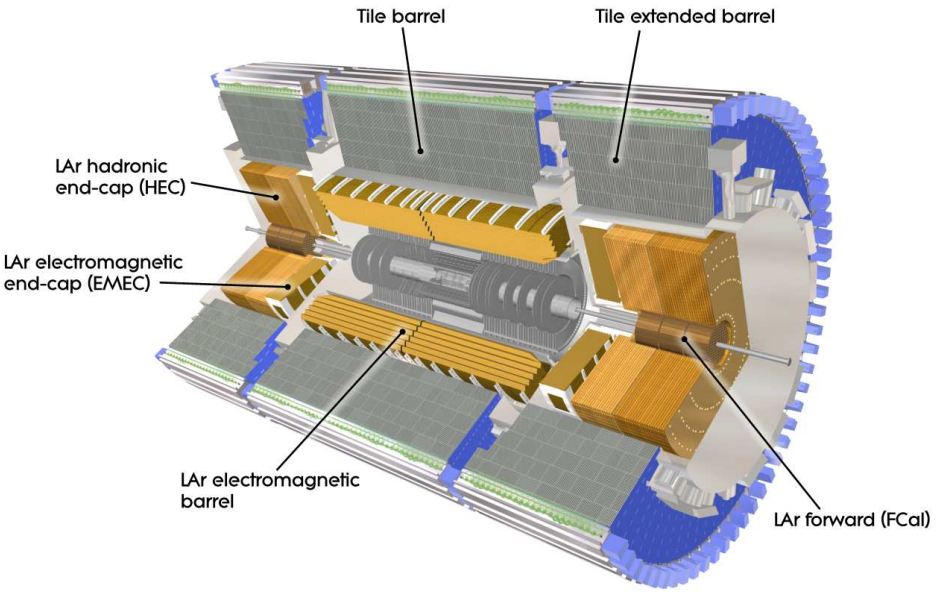

Figure 2.9.: The ATLAS calorimeters. Innermost the liquid-argon electromagnetic calorimeter (LAr), then the scintillator-tile hadronic calorimeter. There is an additional combined forward calorimeter also built with liquid argon technology ($FCal$) adding up to $|\eta| \leq 4.9$.

The Electromagnetic Liquid Argon Calorimeter

The electromagnetic calorimeter is dedicated to the measurement of electrons and photons. Two identical halves form its central part with a small gap of 4 mm at $\eta = 0$. Similarly, the end caps are split into an inner wheel for $|\eta| < 2.5$ and an outer wheel for $2.5 < |\eta| < 3.2$. The transition between barrel and end caps is situated at $|\eta| \approx 1.425$ with a small overlap in-between.
The EM calorimeter combines liquid-argon with lead-absorbers and accordion-shaped Kapton electrodes. It is split into two to three longitudinal sections and providing a totally symmetric φ-behaviour. For a good performance the material in front of the calorimeter has to be minimised. Thus, the solenoidal magnet and the central part share a common vacuum vessel. Additionally, a presampler of liquid-argon is installed in the central region to correct the energy loss in the Inner Detector and the solenoid.

The Hadronic Calorimeter

The central barrel of this sampling calorimeter is placed outside the EM calorimeter. It covers a range of $|\eta| \leq 1$. The two extended barrels reach $|\eta| \leq 1.7$.
The barrel is made of 3 mm thick scintillating tiles as active material and 14 mm thick steel plates which act as an absorber. The calorimeter is segmented azimuthally into 64 modules and longitudinally into three layers.

The liquid-argon hadronic end cap calorimeter (*HEC*) is connected to the outside of the EM end caps and shares the same cryostat. It is split up into two wheels per disk, each consisting of 32 wedge-shaped modules and separated longitudinally in two segments. It covers a range of $2.5 < |\eta| < 3.2$ providing an overlap both with the forward and the extended barrel calorimeters. The wheels are made of 25-50 mm-thick copper plates as absorber with gaps of 8.5 mm active material, liquid argon.

The Forward Calorimeter

The forward calorimeter (*FCal*) is a combined EM-hadronic calorimeter and covers a range of $3.2 < |\eta| < 4.9$. The FCal is divided into three longitudinal segments with a total thickness of nearly 10 radiation lengths. Because of the limited space available, the calorimeter makes use of a high-density design. The first segment is made of copper as an absorber and is mainly dedicated to electromagnetic measurements. The outer layers consisting of Tungsten as absorber serve as hadronic calorimeters. For both segments liquid-argon is the active material. It is filled inside the concentric rods and tubes parallel to the beam pipe.

2.2.5. The ATLAS Muon System

The Toroidal Magnets

The whole ATLAS design is dominated by the choice of its toroidal magnets [39, 46, 47]. The air-core-system (cf. Figure 2.10) consists of a long barrel formed by 8 super-conduction inter-connected coils inside individual cryostats and two smaller end cap toroids, each consisting of 8 coils. Each end cap toroid is put inside one single cryostat. These three magnets generate a magnetic field orthogonal to the muon tracks and facilitate an additional measurement of the muon momentum, independent from the ID. Multiple scattering is minimised because of the light and open design.

The Muon Chambers

The muon spectrometer [48] is situated outside the hadronic calorimeter, between the coils of the toroidal magnets. It covers a total area of $12,000$ m^2. Four different types of muon chambers are in use: the barrel mainly consists of Monitored Drift Tubes (*MDTs*) and Resistive Plate Chambers (*RPC*) while in the end caps there are Cathode Stripe Chambers (*CSC*) and Thin Gap Chambers (*TGC*). Its excellent muon resolution is achieved by three layers of high precision tracking chambers (MDTs and CSCs) and additional trigger chambers (RPCs and TGCs) with a timing resolution of 1.5-4 ns. The chambers of the barrel region are arranged in cylindrical layers around the beam pipe. In the transition and end cap region, the chambers are arranged perpendicular to the beam axis.
The MDTs provide a one-dimensional intrinsic single-hit resolution of 80 μm, the CSCs 40 μm. The RPCs have a two-dimensional spatial resolution of about 1 cm and the TGCs an azimuthal resolution of $2 - 3$ mrad.

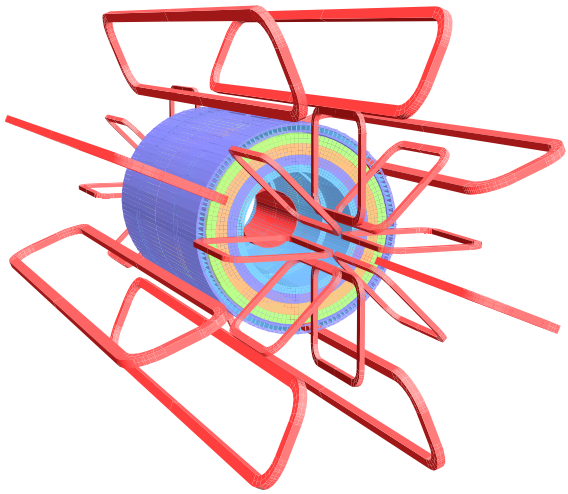

Figure 2.10.: The ATLAS magnetic system with its solenoid surrounding the ID and the three toroids placed in-between the outer layers of the muon system.

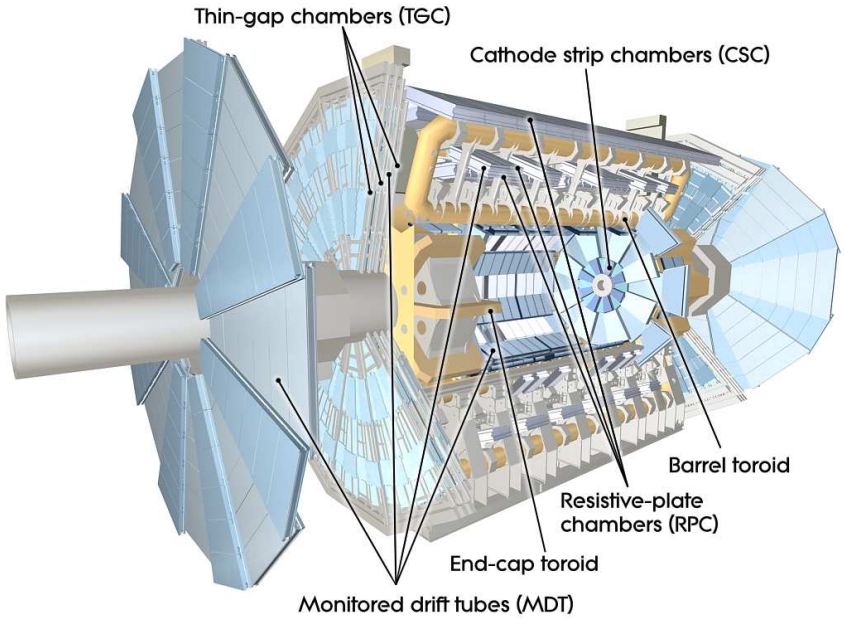

Figure 2.11.: The ATLAS Muon System with its four different types of muon chambers.

2.2.6. Trigger and Data Acquisition

With respect to technological and resource limitations the event data recording needs a severe preselection. A reduction of the 1 GHz proton-proton-interaction-rate at the design luminosity of $\mathcal{L} = 10^{34}$ cm^{-2}s^{-1} by a factor of 5×10^6 is indispensable. Although the total number of recorded events must be reduced drastically possible new physics needs to be enriched at the same time, which makes the decision very hard.

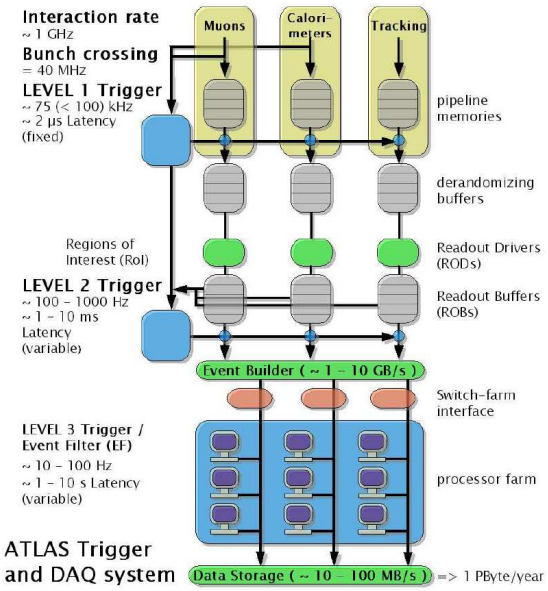

Figure 2.12.: The ATLAS Trigger System [49, 50] is split into three levels. It provides a final data reduction from 1 GHz to approximately 200 Hz.

ATLAS has a 3-levelled trigger system (cf. Figure 2.12). Level-1 (*L1*) [49] uses only information from the calorimeters and the muon trigger chambers to derive its decision and to define *Regions-of-Interest (ROIs)*. L1 reduces the data rate to about 75 kHz with a latency of fewer than 2.5 μs. Meanwhile the event information is buffered by the data acquisition system. Level-2 (*L2*) is only partially hardware-based. Together with the pure software-based event builder (*EF*) it forms the High-Level-Trigger (*HLT*) [50]. They are run on dedicated computing farms and provide a final reduction to approximately 200 Hz. L2 refines the L1-ROIs and applies additional cuts. Finally, the EF combines the full detector information to reconstruct the whole event resulting in a total event size of 1.3 MB.

3. Alignment Strategies for ATLAS

On the one hand ambitious physics aims have been declared, on the other hand, there is this unprecedented huge and very complex tracking system with an excellent intrinsic resolution. A successful combination of these two parts requires a very precise understanding of the detector. For the tracker, using position measurements to reconstruct the four-momenta of particles, is very sensitive to a displacement of its components (*misalignments*). The procedure of obtaining detailed knowledge about the position and orientation of all of the single detector components is called *Alignment* [51].
For example, the requested precision of 25 MeV in the measurement of the W mass significantly constrains track parameters and momentum uncertainties. The degradation of the track parameters of high p_{T} tracks caused by misalignment needs to be smaller than 20%, The momentum resolution has to be smaller than 0.1% [37, 38]. Monte-Carlo studies show that this corresponds to an alignment precision in the R-φ plane (i.e. the uncertainty of the module-to-module distance) of $O(\ll 10\ \mu\mathrm{m})$ as alignment is the dominant source of systematics limiting the W mass measurement.

The alignment procedure of a tracker such as the ATLAS Inner Detector is an endeavour. A careful assembly forms the basis of well aligned modules. But it is limited by the mounting precision, mechanical stress, humidity fluctuations, temperature variations and sagging due to gravity. It is not possible to change the actual position of the detector elements after the assembly. Therefore the following alignment procedures have to determine the irreversible detector shape and create an exact database of it. Neither the mounting precision is sufficient nor the detector layout is constant in time (it is subject to ongoing changes in environmental conditions). Thus, the alignment needs to be adjusted permanently.

One can distinguish between two major alignment approaches: hardware-based alignment, such as survey data or laser interferometry, and track-based alignment, in case of ATLAS represented by three different algorithms: Global-χ^2, Local-χ^2 and Robust Alignment.

3.1. Survey Data and Hardware Alignment

Before final installation, relative positions and orientations of the detector components are measured in a *survey*. This is repeated at later times in order to determine the stability of the modules after extensive handling e.g. transport or modifying single substructures. No significant deviations from original position have been measured within the few μm precision of this method [52].

In addition, the SCT is equipped with a Frequency Scanning Interferometer (*FSI*, cf. Figure 3.1) [53], both for barrel and end caps. It offers the possibility to control the distance between

single barrels, discs and barrel-end cap or the barrel shape. The goal is to resolve thermally induced distortions quasi real-time ($\sim O(10\text{ min})$) with an intrinsic resolution of less than 1 μm. Therefore, hundreds of nodes attached to the support structure provide a geodetic grid of 842 lines. Their elongation is monitored simultaneously. However, the mounting uncertainty of the nodes makes an absolute position measurement impossible, only shape-changes can be detected. Thus, a calibration with an initial alignment is inevitable.

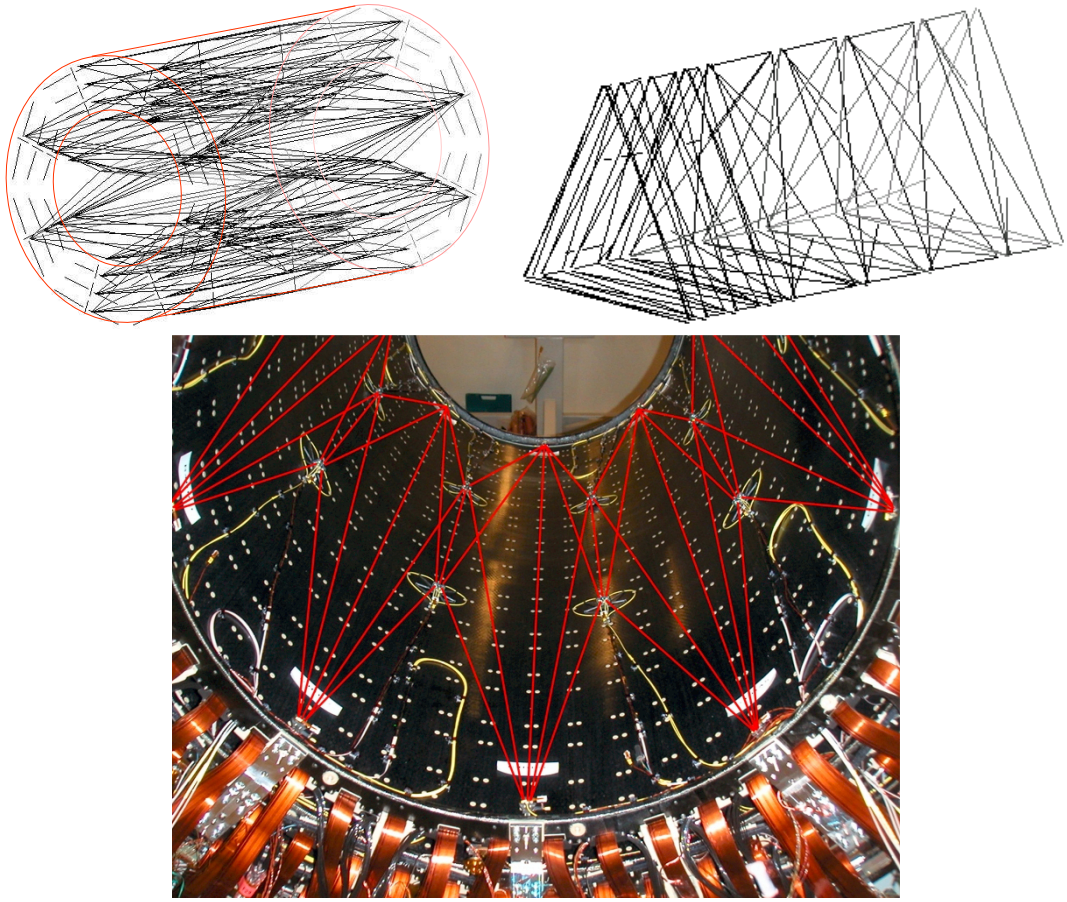

Figure 3.1.: The frequency-scanning interferometry of the SCT [53] provides a real-time monitoring with sub-micron precision. **Top:** Schematics of the 842 grid lines for barrel and end caps **Bottom:** The installation of the FSI on the support structure of an SCT barrel.

3.2. Track-based Alignment

The idea of track-based alignment is very simple (cf. Figure 3.2): high p_{T} tracks should be smooth and straight - in case multiple scattering does not occur. But with a misaligned geometry, tracks become discontinuous. Therefore, geometry must be adjusted to smooth the tracks.

In the beginning a *nominal* alignment must be defined. Typically the ideal detector design is chosen as starting point. With respect to the required precision, statistical concerns, numerical costs and complexity, the detector must be split into small logical units, the building-blocks of alignment.

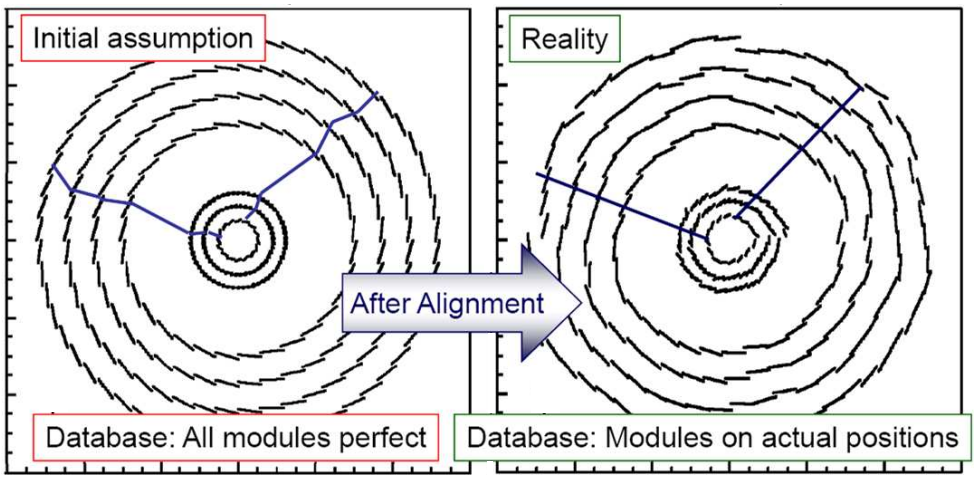

Figure 3.2.: Cross-section of the Inner Detector [54] without **(left)** and with **(right)** a track-based alignment. The real positions of the modules will be kept in an updated geometry database.

For the silicon trackers the choice of the 5,832 single modules is beneficial, each providing 6 degrees of freedom (translation and rotation in a three-dimensional space) adding up to $34,992$ parameters to be determined in total. However, the selection of every single pixel, strip, or for the TRT a selection of every single straw, would be totally unrealistic.

As the alignment parameters can not be measured directly they must be inferred from the fit quality of the measured tracks (cf. Figure 3.3). Let the residual, res, be the distance between the measured hit on a sensor and the intersection of the reconstructed track with the sensor.

This distance can be measured in the module plane (*Inplane residuals*) or perpendicular between track and hit, so called Distance-Of-Closest-Approach residuals (*DOCA residuals*).

$$\begin{aligned} res_{x,\,inplane} &= x_{hit} - x_{track} \\ res_{y,\,inplane} &= y_{hit} - y_{track} \\ res_{x,\,DOCA} &= (x_{hit} - x_{track}) \cdot \sin(\alpha_{x,\,incident}) \\ res_{y,\,DOCA} &= (y_{hit} - y_{track}) \cdot \sin(\alpha_{y,\,incident}) \end{aligned} \tag{3.1}$$

A χ^2 function is built over a large number of tracks from the sum of squared track residuals, depending both on the alignment parameters a and the track parameters π. The minimum then defines the *optimal* detector geometry. With V being the covariance matrix of the hit measurement composed of hit and track uncertainties:

$$\chi^2 = \sum_{data\ sets} \left(\sum_{events} \left(\sum_{tracks} \left(\sum_{hits} res^T(a,\pi) \cdot V^{-1} \cdot res(a,\pi) \right) \right) \right) \tag{3.2}$$

Minimisation of Equation 3.2 leads to a system of tens of thousands of equations.

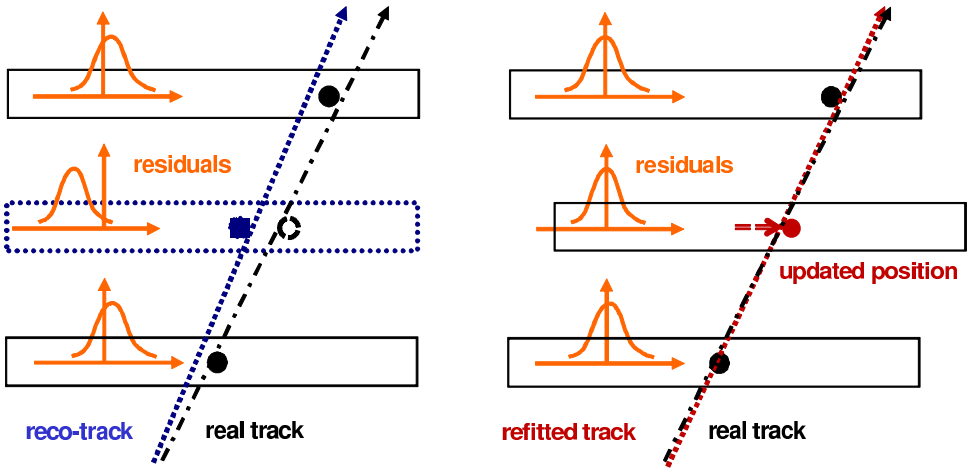

Figure 3.3.: Track fit with three silicon hits. **Left:** As the actual displacement of the module is unknown, the hit is reconstructed in a wrong place and the track fit is pulled to the left. **Right:** With an updated geometry, the hit is reconstructed at its true position and the reconstructed track agrees with the true track very well. - During the alignment procedure, the position of the module is adjusted iteratively in the data base until the combined χ^2 of all modules, a measure for the fit quality, reaches a minimum.

Due to the smallness of misalignments a perturbation theoretical ansatz can be made (*sum over all hits* is an abbreviation for *sum over datasets, events, tracks and hits*) [55]:

$$\delta a = -\left(\sum_{all\ hits} \frac{dres^T}{da} V^{-1} \frac{dres}{da}\right)^{-1} \cdot \left(\sum_{all\ hits} \frac{dres^T}{da} V^{-1} res\right) \tag{3.3}$$

The strategies pursued to solve Equation 3.3 identify the three alignment algorithms, which are discussed in the following.

3.2.1. The Global-χ^2-Algorithm

The *Global-χ^2-Algorithm* [56–58] aims at a direct solution of Eq. (3.3) with simultaneous consideration of all correlations between the different modules. In order to solve this system of equations, a symmetric matrix with size 35,000, being inherently singular due to under-determination and multiple solutions, has to be inverted. This represents a numerical challenge.

$$\frac{dres}{da} = \frac{\partial res}{\partial a} + \frac{\partial res}{\partial \pi} \cdot \frac{d\pi}{da} \tag{3.4}$$

Although the diagonalisation is very time consuming, it offers some advantage as *weakly determined modes* of the system (cf. Section 3.3) can be identified as the eigenvectors of the smallest eigenvalues. Yet, iterative solutions like *fast sparse matrix techniques (MA27 [57])* require fewer operations and less storage, but require preconditioning and do not provide the reliability of the direct solution.

3.2.2. The Robust Algorithm

As already described in Section 2.2.3, a full detector coverage both in φ and z-direction is ensured by an overlap between neighbouring modules. One can make use of this geometric characteristic and define overlap residuals. An overlap residual res_{ov} is composed of the difference between the single residuals of two neighbouring modules hit by the same track, where the *inner* residual means the hit closer to the detector centre:

$$res_{\,overlap} = res_{\,outer\ single\ residual} - res_{\,inner\ single\ residual} \tag{3.5}$$

The *Robust algorithm* [54, 59, 60] centers residual and overlap residual distributions in an iterative way - with focus on simplicity and robustness. However, only the three translational degrees of freedom are considered within this method, while the three rotational DoFs are neglected.

3.2.3. The Local-χ^2-Algorithm

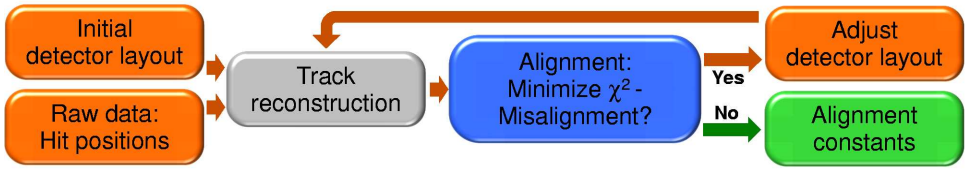

Figure 3.4.: Scheme of the Local-χ^2-algorithm. Initial values (e.g. the ideal geometry or survey data) of geometry are used to do the first reconstruction. Then, in an iterative process, the best-matching detector-layout will be determined which minimises the track quality distribution χ^2.

Also based on Eq. 3.3, the Local-χ^2-algorithm [55, 61] has a slightly different approach. The correlations between different modules are neglected by reducing the full derivative (Eq. 3.4) to a partial derivative:

$$\frac{dres}{da} \rightarrow \frac{\partial res}{\partial a}$$

This is valid, as long as the residual uncertainty is dominated by the hit uncertainty (*error-ratio*):

$$\left(\frac{\sigma_{track}}{\sigma_{hit}}\right)^2 \ll 1 \tag{3.6}$$

The matrix V is diagonal by construction and breaks down to independently calculable 6×6 matrices for each degree of freedom (with σ_i being the uncertainty of the i-th *DoF*).

$$\delta a_i = -\left(\sum_{all\ hits} \frac{\partial res_i^T}{\partial a} \frac{1}{\sigma_i^2} \frac{\partial res_i}{\partial a}\right)^{-1} \left(\sum_{all\ hits} \frac{1}{\sigma_i^2} \frac{\partial res_i^T}{\partial a} res_i\right) \tag{3.7}$$

Again, inter-module correlations are restored via iteratively calculating alignment constants with an updated detector geometry and a re-fit of the tracks (cf. Figure 3.4).

3.3. Weak Modes and Global Deformations

Regarding track-based alignment, some shortcomings concerning weakly constrained DoFs are known which can lead to different scenarios of a systematically misaligned detector geometry. These *weak modes* (cf. Section 3.2.1) are deformations which do not alter the track-χ^2 significantly but yet change the track parameters.
As an example one can consider a track passing a module perpendicularly. An inplane dislocation of the module is reflected by the track fit quality while every movement of the sensor perpendicular to the track is completely invisible (cf. Figure 3.5).

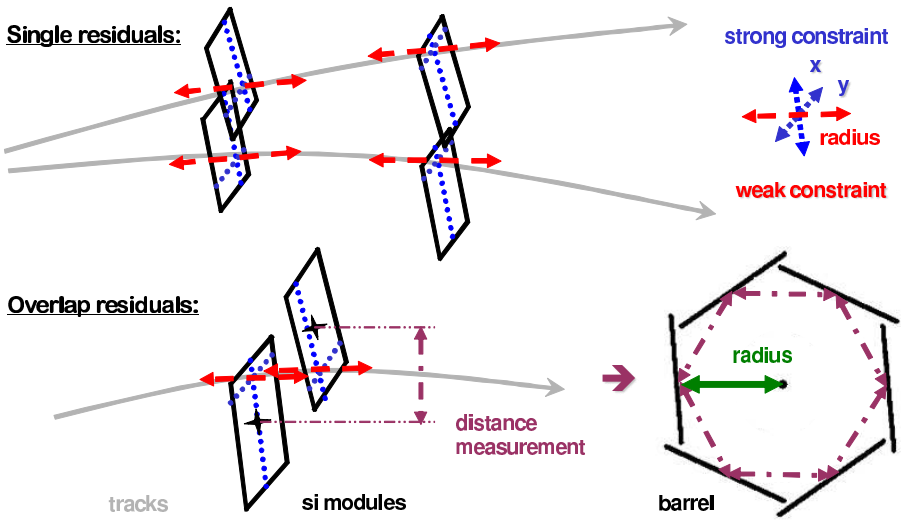

Figure 3.5.: Single residuals are insensitive to translations parallel to the tracks. However, overlap residuals allow to recover this weakness by adding special sensitivity to the distance of neighbouring modules which gives access e.g. to the barrel radius.

When translating this idea to the whole ATLAS barrel geometry, various weak modes of the whole cylinder emerge. Similar considerations can be done for the end caps. Within a simple model, a parametrisation of these deformations as functions of three main parameters can be found [62, 63]: the barrel (end cap) radius R, the polar angle φ and the Z position. Their combination defines a 3×3 matrix (cf. Table 3.1).

	ΔR	$\Delta\varphi$	ΔZ
R	Radial expansion (distance scale)	Curl (charge asymmetry)	Telescope (COM boost)
φ	Elliptical (vertex mass)	Clamshell (vertex displacement)	Skew (COM energy)
Z	Bowing (COM energy)	Twist (CP violation)	Z expansion (distance scale)

Table 3.1.: Global deformations can be described as function of three main parameters: Radius R, angle φ and Z position [62].

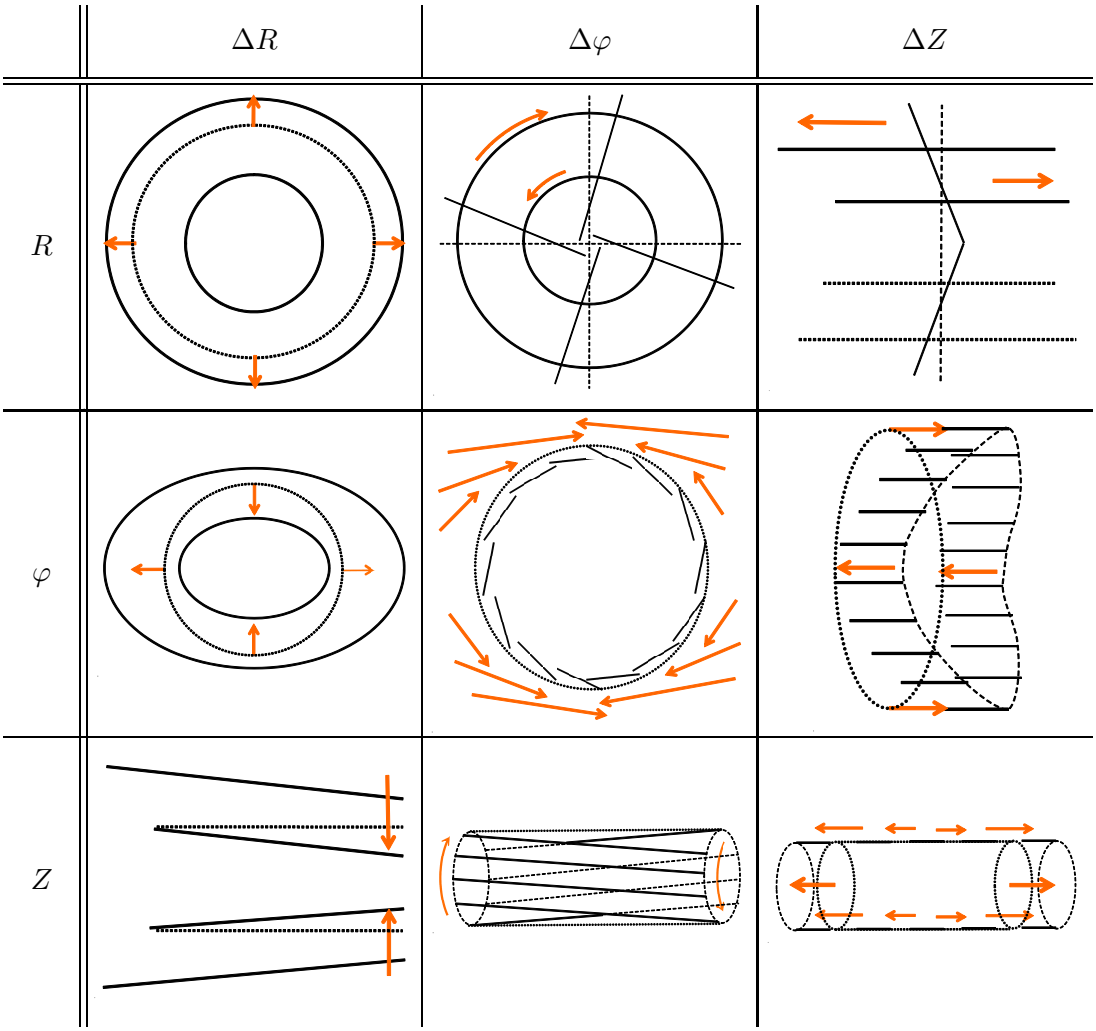

Figure 3.6.: Lowest order implementation of the misalignments (cf. Table 3.1) are shown exemplarily.

Some of these misalignments are represented by quite simple geometrical transformations, others are more complex (cf. Figure 3.6). Yet nearly all kinds of physics measurements are influenced:

- $R\Delta R$ is a radial expansion or shrinking of the whole barrel. Similarly $Z\Delta Z$ stretches the barrel along the beam pipe. All distances are scaled with a certain factor, an absolute length measurement is impossible.
- $\varphi\Delta R$ shapes the barrel cross section elliptically, which influences an invariant mass measurement of particles coming from a common vertex.
- $\varphi\Delta Z$ mimics a change in the centre-of-mass energy, the same is true for ZΔR.
- $R\Delta Z$ simulates a boost along the beam pipe.
- $R\Delta\varphi$ is a radius dependent rotation of complete layers around the beam pipe. It pretends a severe charge asymmetry and leads to biases in the momentum spectrum.

- $\varphi\Delta\varphi$ can create vertex displacements and fake secondary vertices.
- $Z\Delta\varphi$ can simulate a CP violation.

3.4. Overlap Residuals in Detail

Some physics constraints, such as a common vertex or decay properties of particles (J/Ψ, Υ and Z), may provide a first hint of detector deformations because of mass constraints, charge or (a)symmetries in φ or forward-backward. But all of these methods need additional input: for possible charge (a-)symmetries, the initial charge-distribution must be known, p_{T} studies need a well-known p_{T} spectrum of the signal process plus its background, mass constraints need theoretical calculations and the hardware system needs initial alignment values.

Also, a combination of different input datasets such as cosmic muons, muons from beam halo or beam-gas interactions can further improve the alignment as various correlations between different parts of the detector (upper and lower hemisphere, barrel-end cap etc.) are introduced. Yet, even the combination of all these methods is expected to not eliminate all weak modes reliably.

Following the idea of the Robust Alignment Approach (see Section 3.2.2), overlap residuals can be included in the Local-χ^2 algorithm exemplarily. In this case, some benefits emerge:

- No additional assumptions must be made and existing alignment data sets can be interpreted in a different way.
- All six degrees of freedom per module can be aligned.
- A special sensitivity to the distance of neighbouring modules propagates into a circumference measurement, from which the module position perpendicular to the sensor plane can be derived.

There are three different ways of modules i,j forming an overlap residual:

- **Type 1:** *R-φ overlaps* between modules with identical module-η, $\eta_i = \eta_j$, but different module-φ: $\varphi_i = (\varphi_j \pm 1)\, mod(\varphi_{max})$.
- **Type 2:** *z overlaps* with identical module-φ, $\varphi_i = \varphi_j$, and different module-η, $\eta_i = (\eta_j \pm 1)$.
- **Type 3:** *diagonal* overlapping modules with $\eta_i = (\eta_j \pm 1)$ and $\varphi_i = (\varphi_j \pm 1)\, mod(\varphi_{max})$

From purely geometrical considerations, the first case is the most frequent one, while the last one is the rarest.

3.4.1. Expected Behaviour at Nominal Geometry

At nominal geometry, overlap residual distributions have a Gaussian shape and are centred around zero. Naturally, all combinations of overlap residuals show the same behaviour, independent of their position in the detector (φ-, η-coordinate or layer). Moreover, no correlation between participating modules exists as the only correlation could be introduced via the track. In the limit of high statistics, this is negligible.

Overlap residual distributions reflect detector deformations with a non-zero mean as long as the module-to-module distance is affected. A distance between modules which is less than nominal will create a negative residual (cf. Equation 3.2, Equation 3.5 and Figure 3.7), and the other way around. As the smallest alignment element is a complete module, the disadvantage of single residuals appears. Indeed, single residuals of tracks hitting one edge do have an offset, but the ones of the opposing edge have an opposite sign, so the mean over a complete module averages to zero for single residuals. In contrast, overlap residuals increase this shift as the fraction of overlaps closer to the detector centre (i.e. exactly one half of the sensor) is affected by an additional negative sign.

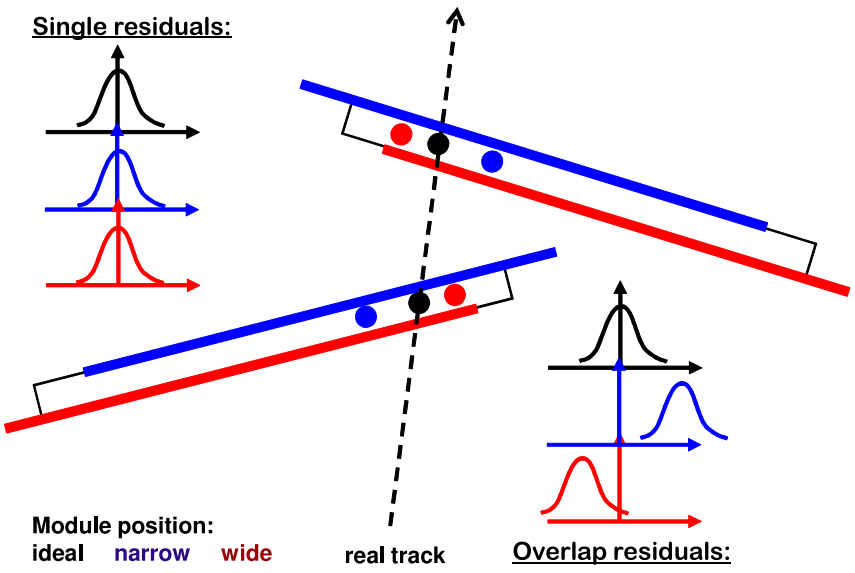

Figure 3.7.: The black modules are situated at their nominal position. An incoming track (dashed) creates the black hits. The average residual distribution is, just as the overlap residual distribution, centered around 0. In the red position, the module distance is less than normal. The red dots represent the positions, where the hits are reconstructed with nominal geometry. Every single residual shows a discrepancy, but the average over a complete module stays centred as both residuals have a different sign. However, as overlaps are defined as difference between outer and inner, the shift increases. Same with opposite sign for the blue position.

3.4.2. Expected Impact of Global Deformations

Due to overlaps being sensitive to the distance of neighboured modules, the deformations split into three groups according to their influence on this distance. The bigger this influence, the more sensitive are the overlap residuals. In principle, all the deformations are detectable:

- Overlaps of type 1 are expected to detect any changes in the R-φ plane, being all deformations of the first column (cf. Table 3.1) and $\varphi\Delta\varphi$, the rest of the second column depending on their implementation.
- Overlaps of type 2 are expected to identify $\{R, Z\}$-ΔZ and $\varphi\Delta Z$ possibly.
- Overlaps of type 3 provide additional information, especially about $Z\Delta\varphi$ and $\varphi\Delta Z$ deformations.

4. Overlap Residuals at Nominal Geometry

Before the impact of misalignments on overlap residuals can be studied, the behaviour and characteristics of overlap residuals at nominal geometry are examined. A reference sample is defined for later comparisons. This also provides a first approximation of the sensitivity of overlap residuals.

4.1. Technical Details

The ATLAS software framework *ATHENA* [64], a full detector simulation, serves as basis for the following studies. It is used in combination with ROOT [65], a C++ based Object-Oriented Data-Analysis Framework, to identify and analyse simulated alignment calibration data with respect to overlap residuals. However, the overlap studies are only the last step in a long chain of algorithms. As data taking has not yet started, events are simulated. They are reconstructed and analysed with the alignment algorithms. The output data will finally be reviewed for overlap residuals.

4.1.1. The ATLAS Software Framework

ATHENA, the ATLAS framework, is a derivative of the Gaudi Common Framework Project. It is composed of several projects connecting both the detector hardware itself and simulated Monte Carlo events with various conditions data bases in order to provide the environment for the various user analyses.

The data flow is shown in Figure 4.1. During normal detector running, real data are recorded. The information is stored in Raw Data Objects (*RDOs*) and the events will be reconstructed progressively with respect to important detector parameters such as the status of its components, environmental parameters (magnetic field, temperature) and accelerator information (luminosity, clock). The results will be provided in two different formats:
ESDs contain the results of reconstruction and the most important parts of the RDOs, so that with a minimum of data the possibility to rerun parts of the reconstruction (e.g. jet calibration or track refitting) is given.
AODs are reduced ESDs and therefore limited to physics quantities from the reconstruction that should suffice for most kinds of analyses. Different physics communities will have separate AODs with different data according to their special needs.

The procedure for event simulation is more sophisticated:
In a first step (*Generation*) the four momenta of particles are generated. This can be done with Monte Carlo Particle Generators such as Pythia or Herwig, which simulate physics processes, or

with a simple Event Generator (*EvGen*) simulating only single isolated particles. The particles are then propagated through the detector (*Simulation*). The magnetic field bends the tracks of charged particles, energy deposition/loss in different materials is taken into account as well as multiple scattering. After this step, the detector response is expected to look as if a real particle just passed. Finally, the read-out is emulated (*Digitisation*), e.g. the deposited electron-hole-pairs in the silicon sensors are collected on the read-out chips or the photons - released by a shower passing the scintillating tiles of the calorimeter. The results are stored in RDOs, too - identical to real data with the difference, that for verification and testing purposes the original Monte Carlo information is added. Afterwards all steps equal the treatment of real data.

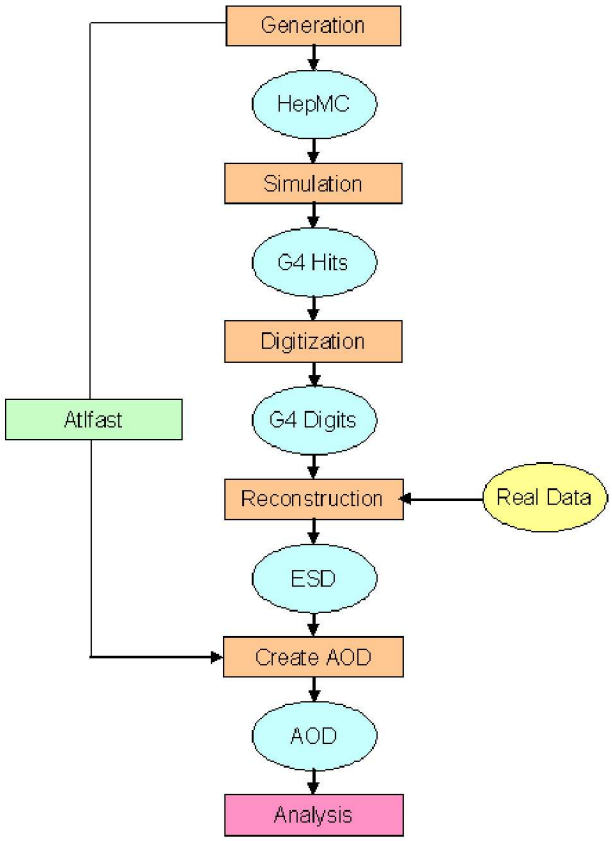

Figure 4.1.: Data flow of ATHENA. Real data are reconstructed and provided in several output formats to the users. For Monte Carlo data, particles have to be generated at first, which then are propagated through the detector. Its response is simulated afterwards. From this point, MC data can be treated like real data. *Atlfast* is a reduced *fast* detector simulation.

For the analysis, basically the following ATHENA-packages [66] are important:

1. Digitisation [67, 68]: InDetDetDescr (InDetReadoutGeometry-01-33-02) and InDetDigitization (PixelDigitization-00-05-17, SCT_Digitization-00-09-15, SiDigitization-03-04-01)
2. Reconstruction: InDetRecExample [69] (InDetRecExample-01-03-42-05)
3. Alignment: LocalChi2AlignAlg [70] (InDetLocalChi2AlignAlgs-00-00-17)

4.1.2. The Simulated Data Sets

The data sets for the alignment calibration studies presented in this thesis consist of simulated muons as they offer different advantages: high p_{T} muons have a very clean signature (easy to identify) and they are numerous both in cosmic data and beam halo. In addition, e.g. $Z \rightarrow \mu\mu$ is of special use, as both muons have a large transverse momentum and originate from the same vertex (vertex and mass constraint).

In order to limit computing power and costs, a reduced data sample of 200,000 events of multi-muons generated with EvGen is used, as these muons have no bremsstrahlung and are easy do identify:

- particle multiplicity: 10μ per event, each with $5\mu^-$ and $5\mu^+$
- particle momentum: $p_{\mathrm{T}} \in [2; 50]$ GeV and $p_{\mathrm{T}} \in [2; 100]$ GeV
- geometrical distribution: flat in $\varphi \in [0; 2\pi]$ and $|\eta| < 2.7$
- vertex origin of all ten muons Gaussian distributed:
  - $\mu_x = 0$ μm, $\sigma_x = 15$ μm
  - $\mu_y = 0$ μm, $\sigma_y = 15$ μm
  - $\mu_z = 0$ μm, $\sigma_z = 56$ mm

4.2. Overlap Residuals at Nominal Geometry

In the following section, typical distributions of overlap residuals at nominal geometry are discussed, characteristics are presented and deviations from theoretical expectations elaborated. DOCA residuals are used if not stated otherwise.

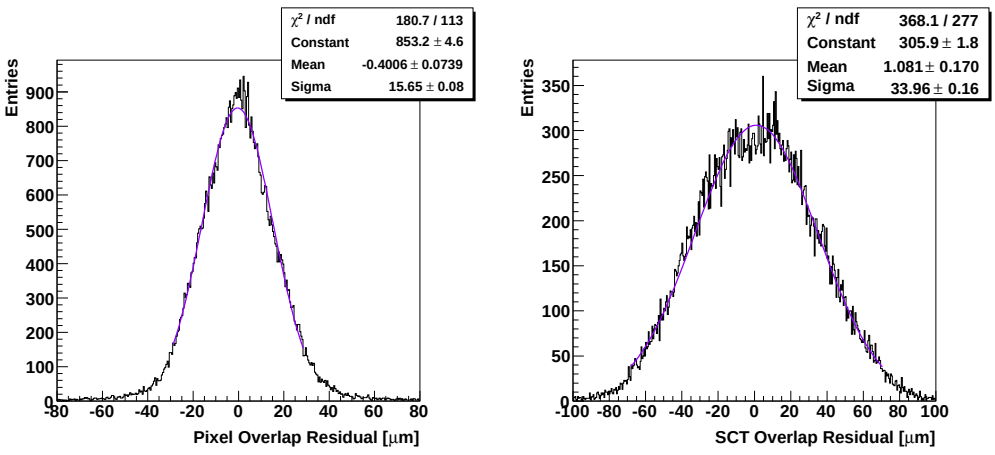

Figure 4.2.: Overlap residuals of the entire Pixel barrel layer 1 **(left)** and SCT barrel layer 1 **(right)**. The overlap residual mean (cf. Figure A.1 for details) differs layer by layer and deviates from zero. The expected Gaussian shape is distorted by asymmetric shoulders and an accumulation of entries in the maximum region.

To gain a first impression, overlap residuals are examined layer by layer (cf. Figure 4.2). There are several points to be made here:

- The Gaussian shape of the distributions is distorted by asymmetric shoulders and an excess of entries near the maximum.
- The mean of the distributions deviates from zero. This shift varies between Pixel, SCT and different layers in a range of (-0.4006 ± 0.0739) μm (Pixel layer 1) and (1.326 ± 0.181) μm (SCT layer 2).

Thus, the distribution of the single residuals, which participate in an overlap, is of special interest, as at least one of these must be shifted also. Both, the residuals of the inner and outer module, contribute to the overlap shifts comparably (cf. Figure 4.3).

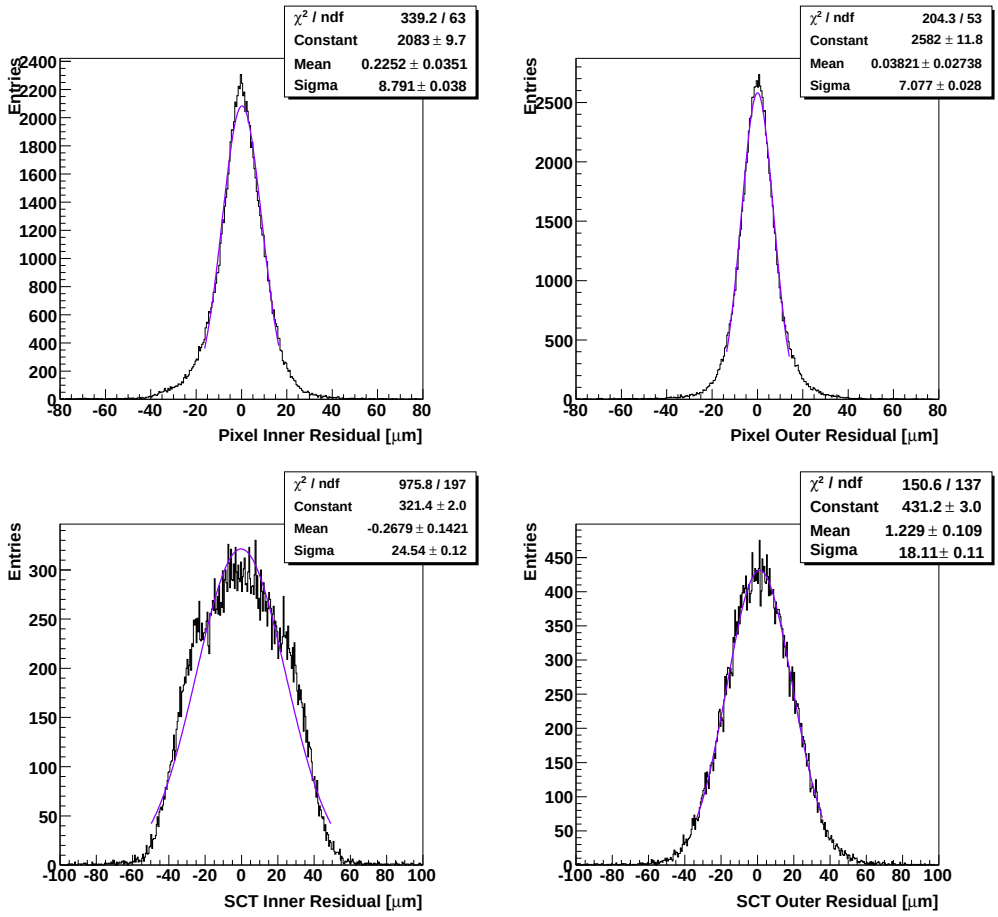

Figure 4.3.: Single residuals which participate in an overlap are shown exemplarily for Pixel layer 0 **(top)** and SCT layer 0 **(bottom)**. - Qualitatively the shape of the single residuals agrees with the overlap residuals, though the shifts of the overlap residuals are divided between the two modules.

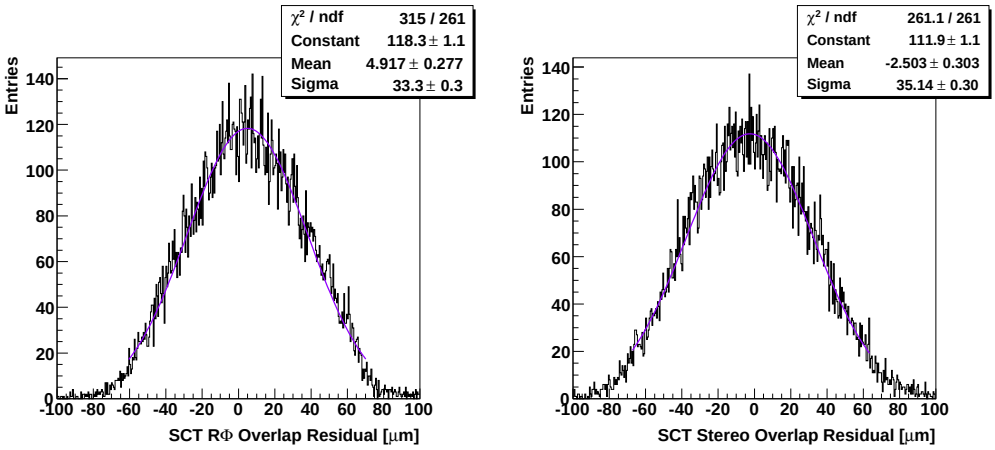

Figure 4.4.: Overlap residuals of the SCT separated by pure axial **(left)** and pure stereo **(right)** side of the module. Mixed are not taken into account due to their rotated coordinate frames. No obvious differences in the overlap residual distributions are found, exemplary SCT layer 0 is shown.

Due to the stereo angle of the SCT modules, it is advisable to distinguish between R-φ (axial) and stereo residuals. As the coordinate frame of the stereo modules is rotated layer by layer alternately around ±40 mrad, the resulting residuals do not represent a clean type 1 overlap. Therefore, only overlaps of the same module side (i.e. R-φ with R-φ, stereo with stereo) are taken into account. Yet, with the stereo angle being very small, the differences between pure axial and pure stereo overlaps can be neglected until further notice (cf. Figure 4.4).

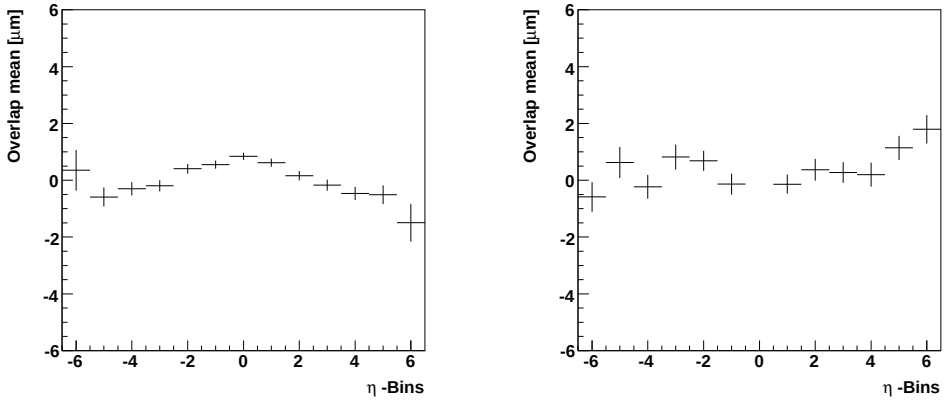

Figure 4.5.: Distribution of overlap residuals versus module-η (*rings*): While the distributions of the SCT are flat and shifted (**right**, layer 1), the Pixel overlap residuals (**left**, layer 0) show a clear η-dependency which decreases going outwards (cf. Figure A.2).

For further analyses, it is very useful to differentiate the overlaps by their geometrical occurrence. With enough statistics every module can be studied separately. But as only about 10-15% of the hits participate in an overlap at all, the overlap residuals of a barrel layer are grouped into *rings* and *staves* in the following, rings being all modules with identical η-coordinate and

staves being all modules with identical ϕ-values. As overlap residuals of type 1 expand over ϕ and $(\phi + 1)$, the overlaps are identified according to the module parameters of the inner module. The same procedure is applied for η with overlaps of type 2.

Overlap residuals as a function of module-φ are nearly flat but shifted according to the distributions of the entire barrel (cf. Figure 4.6). Overlap residuals as function of module-η (cf. Figure 4.5) show a clear η-dependence in the Pixel detector. The amplitude of this structure depends on the layer and decreases going outwards. In Pixel layer 0, the structure has a size of about 3 μm. However, the distributions of the SCT overlaps are flat again.

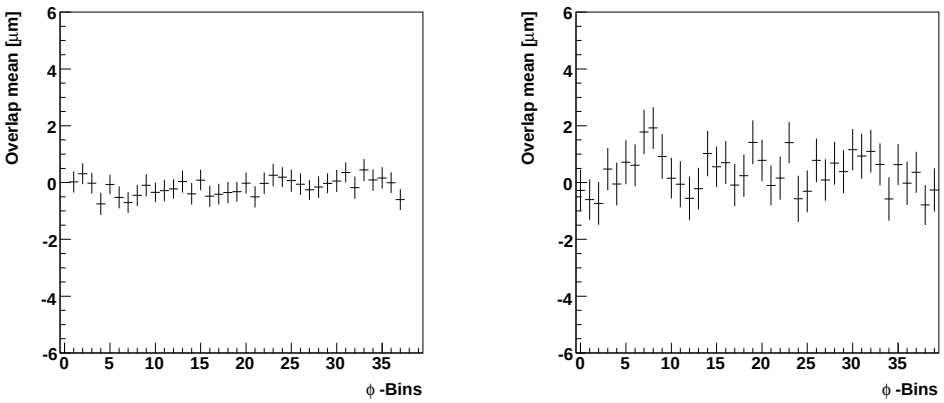

Figure 4.6.: Distribution of overlap residuals versus module-φ (*staves*): The overlap residual distributions of Pixel (**left**, layer 1) and SCTs (**right**, layer 1) are flat, but reflect the shifts already seen in the distributions of the entire barrel. Compare Figure A.3.

According to the premises of the Local-χ-algorithm, the assumption of the two residuals forming an overlap being uncorrelated is limited by the *error ratio* (cf. Equation 3.6).
A correlation between different modules can be introduced by tracks hitting both modules. If the hit uncertainty is not dominated by the track uncertainty ($\sigma_{track} \not\ll \sigma_{hit}$), the single hits will be correlated. The error ratio is shown in Figure 4.7 and the correlation between the residuals in Figure 4.8. Concordantly, both figures show a highly visible anti-correlation, which is confirmed by the associated correlation coefficients, e.g. Pixel layer 0 has a correlation coefficient of about -0.57 and SCT layer 3 of about about -0.48. The strength of the correlation is largest both in the innermost Pixel and outermost SCT layer, while in the middle layers, the correlation is weaker (cf. Figure A.5, Table 4.1). The correlation coefficient of SCT layer 0 is only about -0.24 and thus the absolute value significantly smaller.
Besides, various Pixel overlap residuals exist with one single residual distribution being noticeably narrower than the other (cross-like pattern).

detector	Pixel			SCT			
layer	0	1	2	0	1	2	3
correlation coefficient ρ	-0.5735	-0.2909	-0.3568	-0.2391	-0.2384	-0.3331	-0.4815
mean of the error ratio	1.0970	0.7354	0.9507	0.3255	0.3192	0.4111	0.6107

Table 4.1.: Correlation coefficients of the different layers both for the Pixel and the SCT detector. The innermost and outermost layers have the largest correlation coefficients and accordingly a large mean of the error ratio.

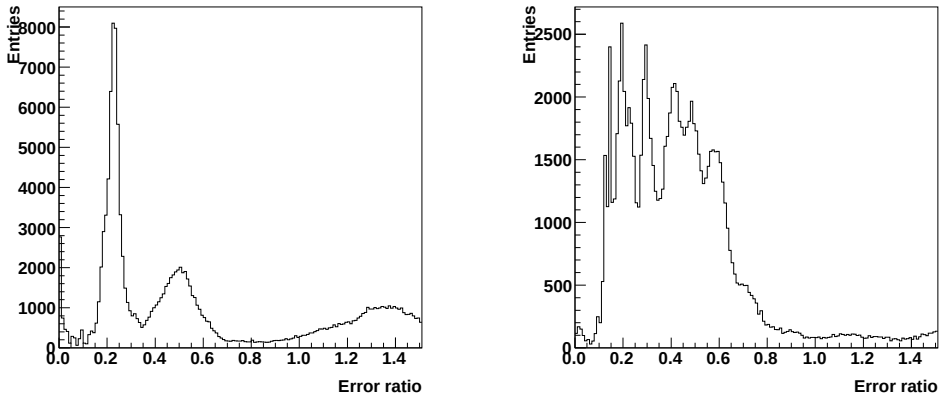

Figure 4.7.: Error ratio $\sigma_{track}/\sigma_{hit}$ of Pixel layer 0 **(left)** and SCT layer 3 **(right)**: The residual uncertainty is dominated by the track uncertainty mainly (cf. Figure A.4). Thus, the single hits must be correlated (cf. Equation 3.6).

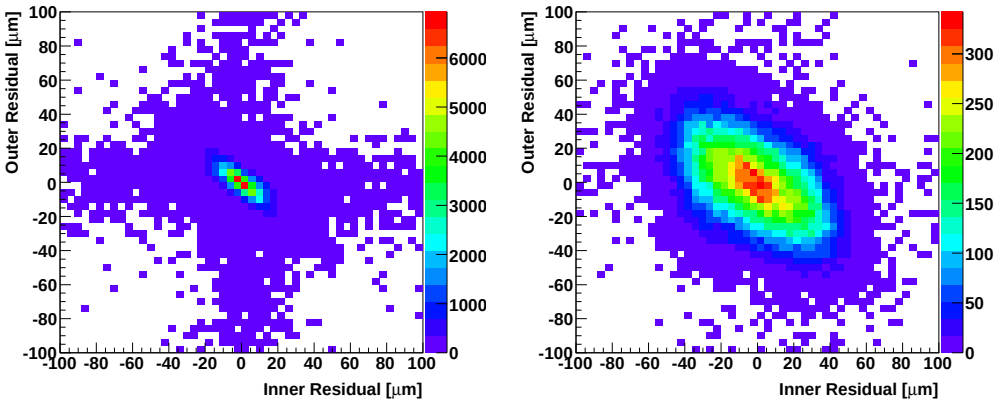

Figure 4.8.: The anti-correlation between the partners is reflected especially in the innermost Pixel layer **(left)** and outermost SCT layer **(right)**. In-between the correlation is weaker (cf. Figure A.5). Various Pixel overlap residuals exist with one single residual distribution being significantly narrower than the other.

Finally, a comparison between *Inplane*- and *DOCA*-residuals is made (cf. Figure 4.9). Except for a known permutation of the residual definition in the Pixel detector, which leads to a flip in the sign of the residuals, the results agree very well.

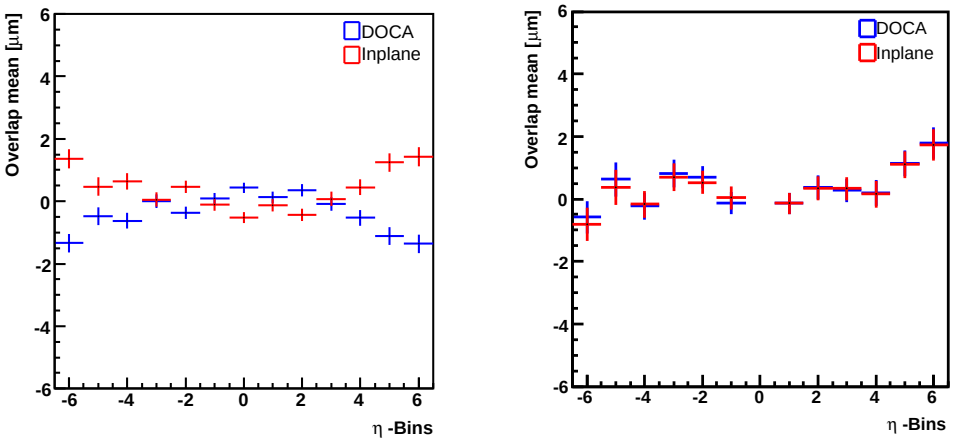

Figure 4.9.: Comparison between Inplane (red) and DOCA (blue) overlap residuals versus module-η, shown for Pixel layer 1 **(left)** and SCT layer 1 **(right)**. - Besides a known permutation in the Pixel residual definition, no discrepancy between the overlap residual distributions is found.

Altogether, there are multiple discrepancies between overlap residuals and theoretical expectations (cf. Section 3.4):

1. The mean of the overlap residual distributions of a complete barrel deviates from zero by a few μm - depending on layer and detector type. The shifts range between (-0.4006 ± 0.0739) μm (Pixel layer 1) and (1.326 ± 0.181) μm (SCT layer 2).

2. The single hits forming an overlap are correlated. This agrees with a too large error ratio ($O(0.5)$ to high). The effects depend on the detector type and the layer.

3. The mean of the overlap residuals shows an unexpected η-dependence for the Pixel detector. The amplitude of this effect depends on the layer, e.g. it is 3 μm on layer 0.

The maximum impact of these discrepancies can be estimated to about $(3 - 4)$ μm. Thus, also the achievable precision of overlap residuals is limited to a few μm. These effects need to be understood before any serious alignment efforts.

4.3. Studies Motivated by Physics

The detector design is asymmetric, both types of silicon trackers have a tilt angle ($+20°$ for Pixel and $-10°$ for SCT). Thus, a bias can be introduced through these different measuring planes, in which the residuals are defined, or the definition of overlap residuals itself.

Slightly different behaviour therefore can be expected in several further variables: both, differently charged tracks and tracks with different transverse momenta lead to different typical incident angles (hit angle between track and module). Moreover, the incident angle varies on different layers just as the angle between two neighbouring modules is radius-dependent.

4.3.1. Detector Geometry

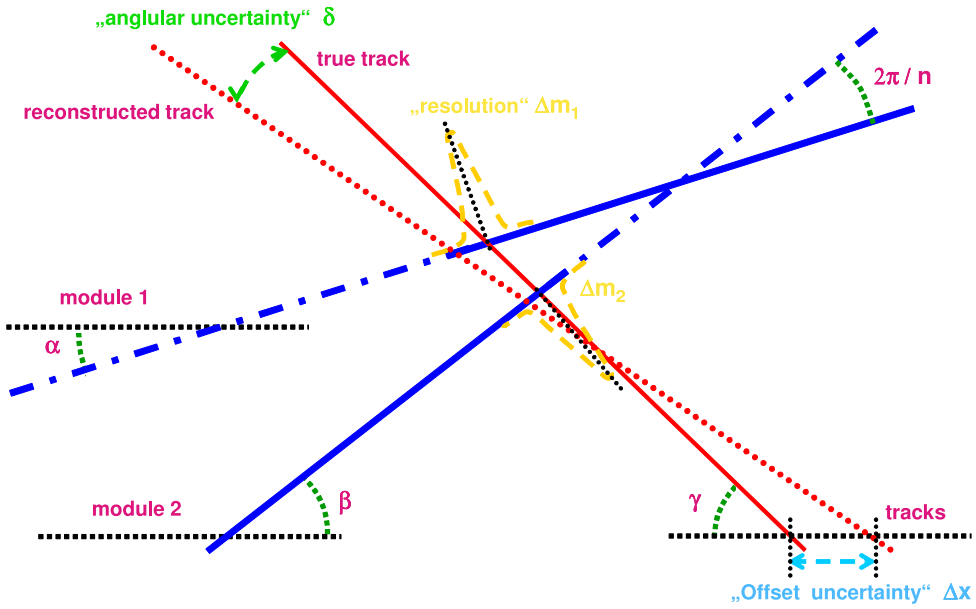

Figure 4.10.: Assuming straight tracks (infinite transverse momentum), there are only three sources of uncertainties: the module resolution (case 1), the track offset (i.e. the vertex, case 2) and the angle of the track (case 3).

A simple two-dimensional model of overlap residuals (e.g. barrel cross section in the R-φ-plane at $\eta = 0$), represented by two modules with an infinite momentum track traversing both of them, is used to estimate this geometrical effect. Two modules do not allow for a reasonable track reconstruction, thus a Gaussian smearing of the track parameters and hit resolution is assumed.
Only three sources of uncertainties (cf. Figure 4.10) which can cause deviations between hit and track exist then:

1. The intrinsic module resolution, Δm, caused by the module segmentation. This is defined in the module plane (cf. Figure 4.11, left).

2. Deviations of the one-dimensional track vertex (track offset), Δx, due to vertex resolution (cf. Figure 4.11, right).

3. Deviations of the angle of the reconstructed track, $\Delta\delta$, due to track parameter resolution (cf. Figure 4.13).

Let α be the inclination angle of module 1, β of module 2. γ represents the track gradient in an arbitrary coordinate system. The angle between modules is given by the number of modules in a barrel ring, n:

$$(\beta - \alpha) = \frac{2\pi}{n}.$$

The incident angles ϑ_1, ϑ_2 between the modules and the track are given by:

$$\begin{aligned} \vartheta_1 &= (\alpha + \gamma)\,, \\ \vartheta_2 &= (\beta + \gamma)\,. \end{aligned}$$

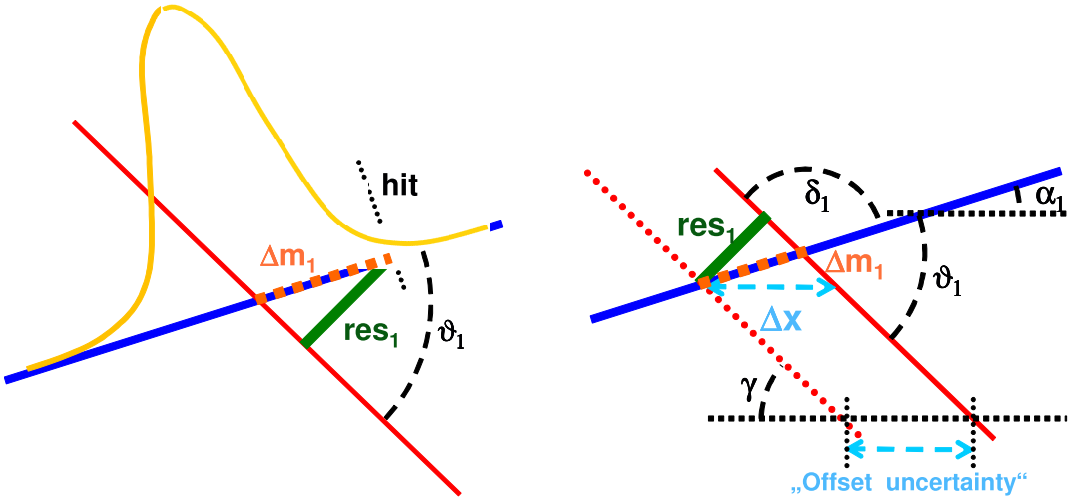

Figure 4.11.: Detailed sketch of the simple overlap model - **Left:** Case of module resolution. **Right:** Case of uncertainty of track offset.

Case 1: Module Resolution

$$\begin{aligned} res_{overlap,\ case\ 1}\,(\alpha, \gamma, n) &= res_1 && - res_2 \\ &= \Delta m_1 \cdot \sin(\vartheta_1) && - \Delta m_2 \cdot \sin(\vartheta_2) \\ &= \Delta m_1 \cdot \sin(\gamma + \alpha) && - \Delta m_2 \cdot \sin(\gamma + \alpha + {}^{2\pi}/_{n}) \end{aligned} \tag{4.1}$$

Let x be fixed and pulled from a Gaussian distribution with $\mu = \Delta m$, then the residual is shifted as a function of the track angle (cf. Figure 4.12, left). This shift is of the same order of magnitude as the module resolution itself.

Let x_1 and x_2 be two randomly chosen, Gaussian distributed hits with $\mu_1 = \Delta m_1$ and $\mu_2 = \Delta m_2$, then the resulting overlap as function of track angle is asymmetric, too (cf. Figure 4.12, right).
In reality there is an ensemble of various tracks at various angles. The assumption of an identical and symmetric resolution for both modules in combination with symmetric distribution of track angles leads to a perfectly centered overlap residual distribution on average.

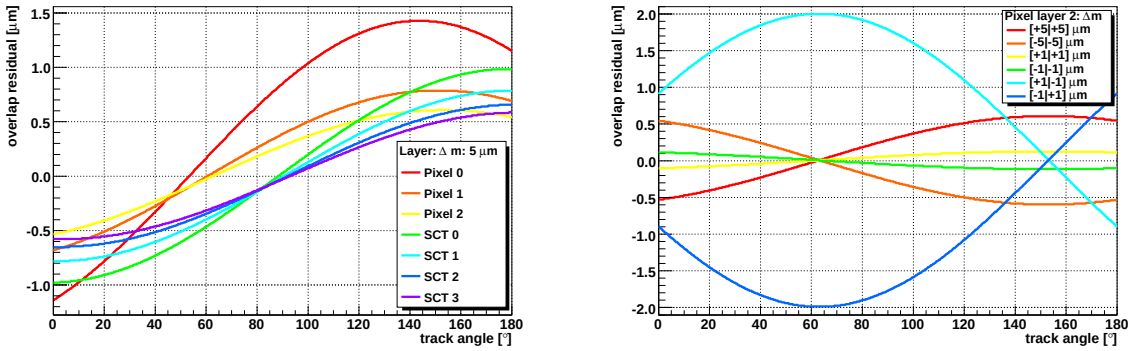

Figure 4.12.: Left: The assumption of a module resolution of a few micron leads to a small asymmetry of each individual residual as function of the track angle. The amplitude of this shift depends on the layer with slightly different behaviour for Pixel and SCT. A track angle of 90° corresponds to a radial track. **Right:** When assuming identical and symmetric module resolution distributions, the overlap asymmetry vanishes on average.

Case 2: Track Vertex With the Law of sines, the missing angle δ can be expressed as

$$\sin(\delta_1) = \sin(\pi - \alpha - \gamma) = \sin(\alpha + \gamma) \tag{4.2}$$

$$\begin{aligned} res_{overlap,\ case\ 2}\,(\alpha, \gamma, n) &= res_1 && - res_2 \\ &= \Delta m_1 \cdot \sin(\vartheta_1) && - \Delta m_2 \cdot \sin(\vartheta_2) \\ &\overset{4.2}{=} \left(\frac{\sin(\gamma)}{\sin(\delta_1)} \Delta x\right) \cdot \sin(\gamma + \alpha) && - \left(\frac{\sin(\gamma)}{\sin(\delta_2)} \Delta x\right) \cdot \sin(\gamma + \beta) \\ &= \Delta x \cdot \sin(\gamma) && - \Delta x \cdot \sin(\gamma) \\ &= 0 \end{aligned} \tag{4.3}$$

The track offset uncertainty does not influence the overlap residuals at all.

Case 3: Track Angle With the theorem of intersecting lines, a correlation between the residuals is defined by:

$$\frac{res_1}{a + \delta a} = \frac{res_2}{a} = \tan(\Delta\delta), \qquad \frac{res_1}{b + \delta b} = \frac{res_2}{b} = \sin(\Delta\delta) \tag{4.4}$$

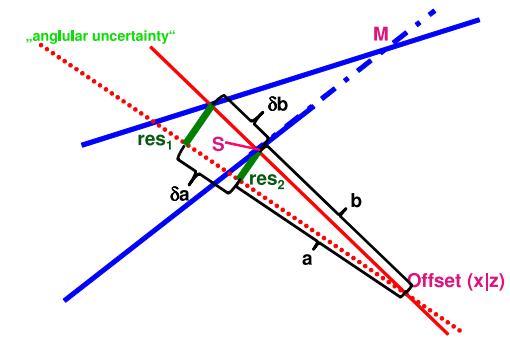

Figure 4.13.: Errors during track reconstruction cause an angular uncertainty $\Delta\delta$.

$$\begin{aligned} \Rightarrow res_{overlap,\ case\ 3}\,(\alpha,\gamma,n) &= res_1 && -res_2 \\ &= (b+\delta b)\cdot\sin(\Delta\delta) && -b\cdot\sin(\Delta\delta) \\ &= \delta b\cdot\sin(\Delta\delta) && \end{aligned} \tag{4.5}$$

From the law of sines, δb can be reduced to the distance $\overline{MS}$:

$$\delta b = \frac{\sin(\alpha-\beta)}{\sin(\alpha+\gamma+\Delta\delta)}\cdot\overline{MS}$$

Pure geometrical considerations finally lead to

$$res_{overlap,\ case\ 3}\,(\alpha,\ \gamma,\ n,\ x,\ z) = \sin(\Delta\delta)\cdot\frac{\sin\left(2\pi/n\right)}{\sin\left(\alpha+\gamma+\Delta\delta\right)}\cdot A, \tag{4.6}$$

$$A := \left[\sin(\Delta\delta+\gamma)\left(r\sin\left(2\pi/n\right)+x\right)+\cos(\Delta\delta+\gamma)\left(r\cos\left(2\pi/n\right)-z\right)+B\right],$$

$$B := \frac{-r\cos(\alpha)+r\sin(\alpha)\sin\left(2\pi/n\right)+r\cos(\alpha)\cos\left(2\pi/n\right)}{\cos\left(\alpha+2\pi/n\right)\sin(\alpha)+\sin\left(\alpha+2\pi/n\right)\cos(\alpha)}.$$

This mode depends on the swivel of the rotation. Let φ be a fixed value of a Gaussian distributed angular uncertainty ($\mu = \Delta\delta$) with a certain distance to the swivel, Δz, then the resulting overlap becomes asymmetric and the amount of shift depends on the track angle (cf. Figure 4.14). Yet, the total distance Δz does not influence the asymmetry. Averaging over various tracks at various angles eliminates this asymmetry as long as the angular uncertainty distribution is symmetric.

Cross-check with Toy Monte Carlo

As the analytical calculations describe only the mean of the residual distributions an additional cross check with a toy Monte Carlo is done. This is implemented analogously to what is described above.

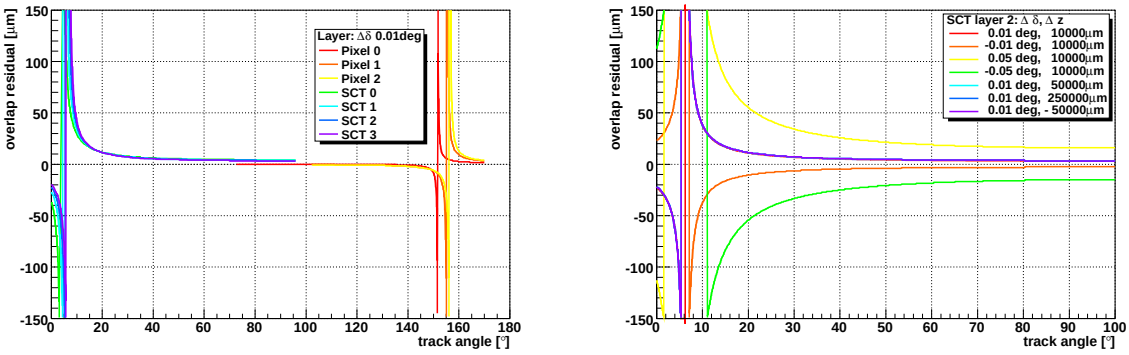

Figure 4.14.: Left: The assumption of an angular track error causes an asymmetry, too. Singularities appear in case track and module are parallel. The amplitude of the asymmetry depends on the track angle. **Right:** With symmetrical angular error distribution this asymmetry vanishes on average.

The track angle varies between 0° and 180° in steps of 1°. For each step, 500,000 tracks are simulated. The module resolution is assumed to be Gaussian with a spread of 5 μm. The angular uncertainty has a Gaussian shape with a spread of 0.05°. The rotation swivel is $\Delta z = 10,000$ μm away from the module.

No deviations between the toy MC and analytical calculations are found (cf. Figure 4.15). Although small asymmetries are produced, the assumption of symmetric distributions for module resolution, track angle and track uncertainties, make them cancel independently of the layer on average. Thus, the asymmetric detector geometry itself does not cause the observed shifts in the overlap residual distributions at nominal geometry.

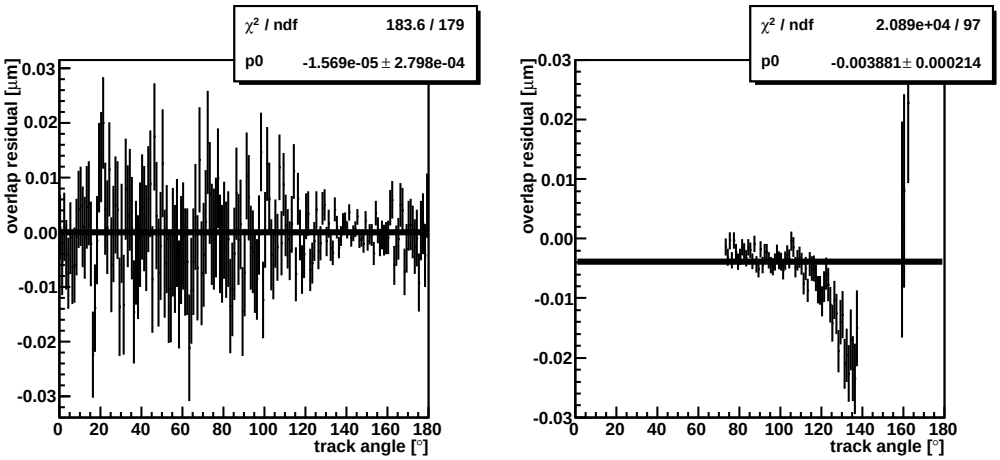

Figure 4.15.: Cross-check of the analytical calculations with a Toy-MC. Pixel layer 0 is chosen as example. In both cases, the Toy-MC perfectly confirms the analytical calculations. Within given uncertainties, the possible asymmetry is orders of magnitude to small.

4.3.2. Transverse Momentum

Due to the solenoidal magnetic field in the Inner Detector, the tracks of charged particles are bent. The curvature of the track depends on the particle momentum. Low p_T tracks ($p_T < (5-10)$ GeV) have a helical shape, while high p_T tracks ($p_T > 40$ GeV) are nearly straight. This defines the typical incident angle between track and module. For high p_T tracks in ATHENA correspond to tracks of about 90° in the toy MC, low p_T tracks to angles between $(0-45)°$ or $(135-180)°$.
No systematic differences between the overlap residuals of the different p_T regions are found in ATHENA (cf. Figure 4.16). The overlap shifts obviously do not depend on the transverse momentum.

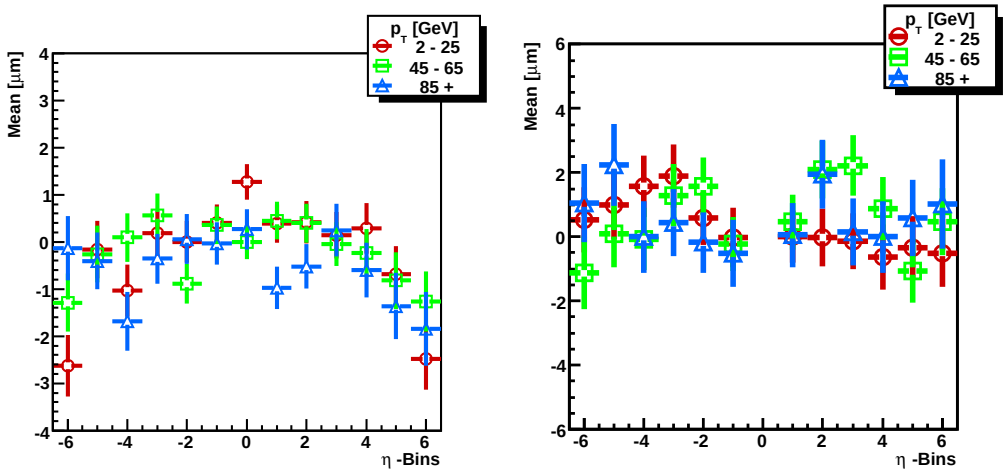

Figure 4.16.: Different p_T cuts are applied. No systematic deviations between the overlap residuals of the different p_T ranges are found, neither for Pixel (**left**, layer 1) nor SCT (**right**, layer 3).

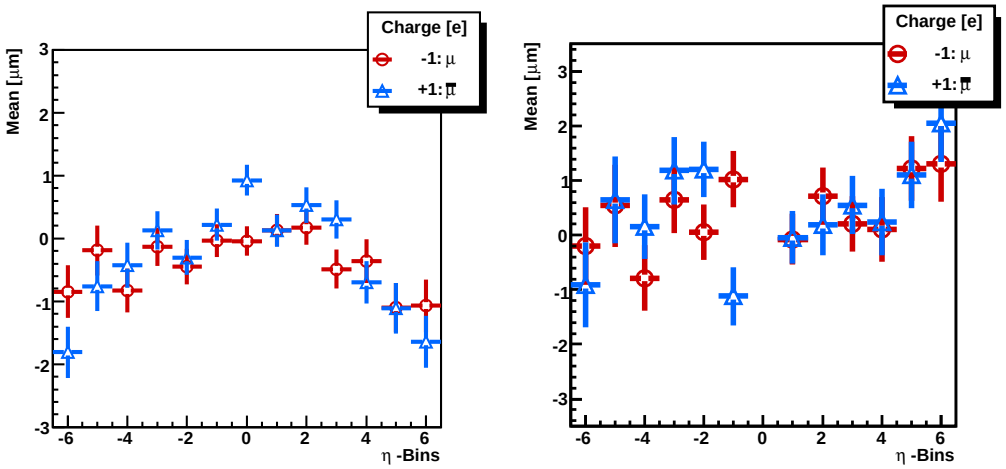

Figure 4.17.: A cut on the charge sign of the original particle is applied, as this corresponds to a special region of inclination angles. Overlap residuals versus module-η are shown for pixel layer 1 **(left)** and SCT layer 1 **(right)**. Again no systematic deviations are found.

4.3.3. Charge Asymmetry

With a cut on the charge of a particle only left- or right bent tracks can be selected. The bending direction determines the typical incident angle, which could indirectly cause asymmetries due to the detector geometry.

No systematic deviations between the different charges are found for the Pixel and the SCT (cf. Figure 4.17). The overlap shifts do neither depend on the charge of the particle nor its transverse momentum nor a combination of both. These results completely agree with the toy MC. The detector does not cause overlap shifts indirectly by different incident angles.

4.4. Technical Issues

In this section, the focus is on technical issues such as software or database versions. As ATHENA is still under construction, there are changes of different severance between the various tags. But also within one version, e.g. different tracking options can influence the results.

Athena Version 12.0.1, 12.0.3 and 12.0.5 are compared (they represent the software development during the last year). No significant changes in the overlap residual distributions are found.

Geometry Tags The ATLAS detector geometry database stores the entire information which is necessary for the detector description applications to build various versions of the detector. Different detector layouts such as an initial, ideal or typical layout are taken into account just as the magnetic field and the material properties.

All tags start with 'ATLAS', followed by a tag-name and some typical blocks of identifiers *ATLAS-name-xx-yy-zz*. The name typically describes the main characteristics of the tag: 'Comm' for *Commissioning*, 'NF' for *No magnetic field* or 'CSC' for *Computing System Commissioning*. xx is the major version number, while yy describes small changes as different magnetic field or alignment. zz is reserved for bug fixes and patches.

Of main interest are:

- ATLAS-DC3-02, which is an updated version of the early DC3-geometry. This version is the production layout of ATHENA 11.0.X.
- ATLAS-CSC-00-00-00, which is an updated version of DC3-02 with various severe changes concerning cavern, material and sub-detectors (among others silicon tracker positions). This geometry is adequate for ATHENA 12.0.X.

From DC3-02 to CSC-00-00-00 the simulation of every part of the detector became more realistic. This includes both some small bug fixes and a total Inner Detector update (Inner Detector-DC3-04). Although the biased Pixel residual distribution of overlap residuals as a

function of module-η slide closer to zero (about 1 μm for Pixel layer 0), no significant change in the residual shape is found (cf. Figure 4.18). For the SCT, no deviations are seen at all. Indeed, the new geometry tag does influence overlap residuals, but does not change the shape of the distributions. In this thesis, CSC-00-00-00 is chosen if not stated otherwise.

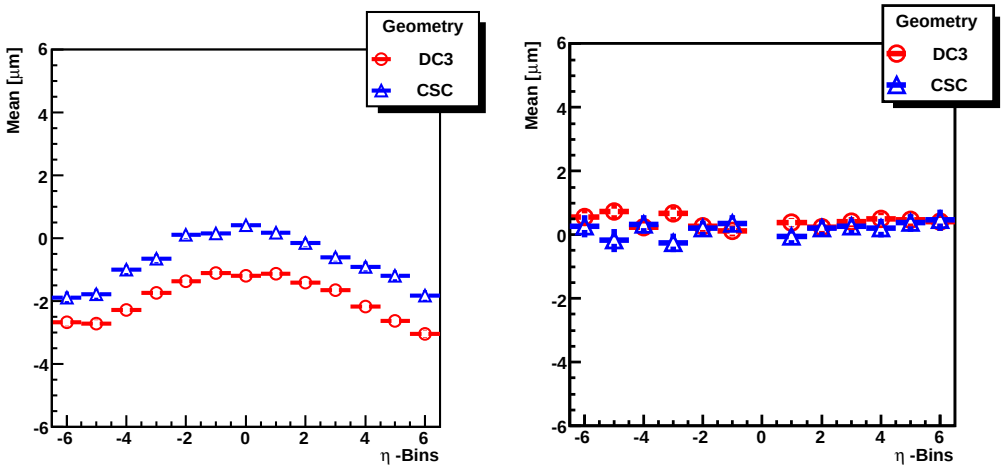

Figure 4.18.: Overlap residuals with different geometry tags: DC3-02 and CSC-00-00-00. The SCT **(right)** does not show any significant deviations while the Pixel overlaps **(left)** are closer by zero on average, but their shape is conserved.

Different Tracking Options ATHENA offers three different tracking algorithms, which are the result of historical developments mostly: *iPatRec*, *xKalman* and *NewTracking*. The Local-χ^2-Algorithm, used to determine the residuals, favours the last one, so all studies are done with the NewTracking.

Track reconstruction proceeds in several steps. First, the *pattern recognition* tries to sort all the hits in the whole detector with different algorithms and creates collections of hits which are assigned to a possible track. The hits of a collection are sorted geometrically afterwards. A *Kalman*-Fitter processes the hits outwards and inwards successively, and for every hit the fit parameters are adapted as the track is iteratively fitted via a χ^2-minimisation of the residuals (similar to the alignment procedure, but this time hit positions are retained and the track can vary). This fit can be done with different options: a *biased* fit includes every hit for every iteration of the fitting procedure. This is the easiest way and the statistics is maximised. However, a hit which does not belong to the track under study or is an artefact of the detector, might influence the fit severely and pull the fit into a wrong direction. Alternatively, the hit of the module, which is actually processed, is excluded from the fit (*unbiased* fit). This decreases the influence of outliers, but the statistics is smaller as for every fit one hit is neglected. A special case of an unbiased fit can be found for the SCT. Although every side of a SCT module reports a hit independently, both hits are severely correlated by geometry. One can decide if both hits of a SCT module are excluded successively (*semi-unbiased*) or at the same time (*true-unbiased*).

Although the unbiased fit increases the shifts of the Pixel overlap residuals about e.g. 1 μm (Pixel layer 1), the tracking options are not the reason for this shift. In the SCT no differences can be found, neither between biased and semi-unbiased nor between semi- and true-unbiased resid-

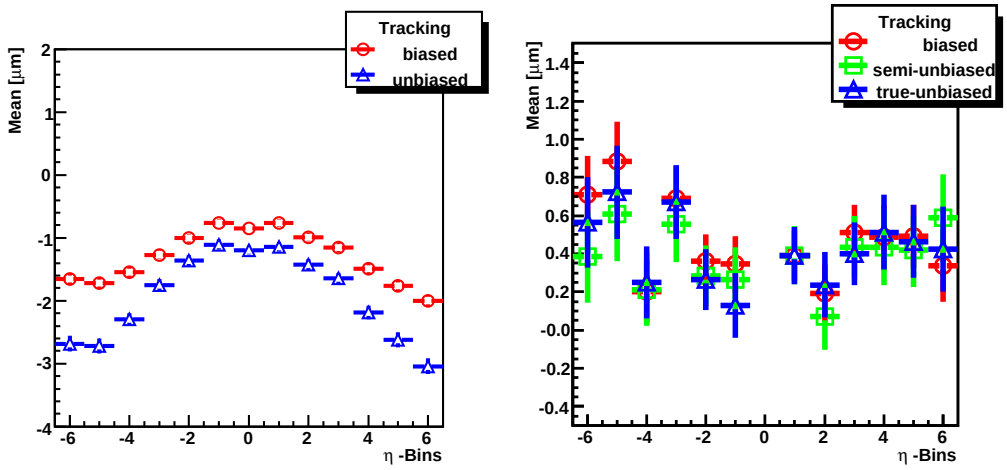

Figure 4.19.: Different tracking options can increase the amplitude of the Pixel overlap residual shifts (**left**, layer 1), but do not influence their shape. Neither of the three tracking options (((true-)un-)biased) does create systematic deviations in the SCT (**right**, layer 1).

uals. So, these different tracking options do have a small influence on overlap residuals, but do not cause the observed deviations. Since true-unbiased residuals show the clearest η-dependency, they are in use.

4.5. Silicon Hit in Detail

Applying an external electric field to a silicon sensor, used in reverse-biasing mode, ideally increases the depletion zone over the whole sensor [67]. A charged particle traversing the depletion zone usually creates pairs of electrons and holes along its track (cf. Figure 4.20). Due to the electric field, the produced charges drift towards the electrodes. An additional magnetic field causes a lateral deflection because of the Lorentz force. The angle between the primary drift direction and the resulting drift direction of the charges is therefore called *Lorentz angle*, ϑ_{lor}. It depends on the magnetic field, B, and the Hall mobility, μ_{hall}, of the drifting charges.

$$\tan \vartheta_{lor} = \mu_{hall} \cdot B = \frac{\Delta x}{\Delta Z} \tag{4.7}$$

The charge cloud widens in the direction perpendicular to their drift direction due to diffusion. The drifting electrons are collected on electrodes at the upper sensor surface. Finally the information is delivered to the read-out chips for further processing.

A maximum Lorentz angle of about 17° is found in Pixel layer 0. This leads to a typically lateral drift of a particle, traversing the whole depth of the sensor, of about 75 μm. A typical diffusion radius of electrons in the Pixel detector is given by (6-8) μm.

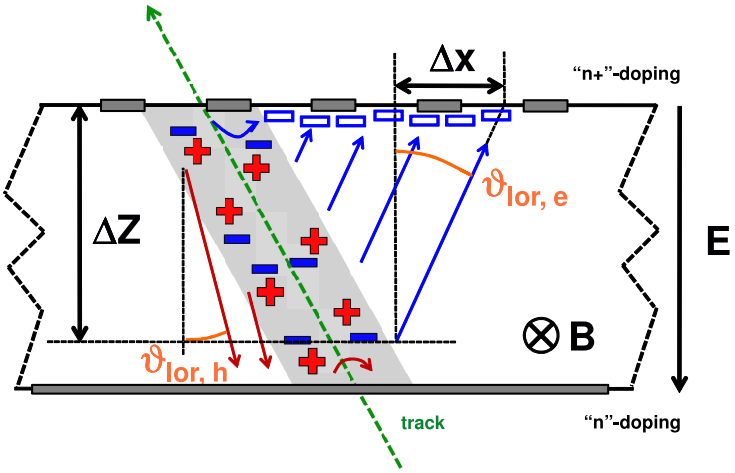

Figure 4.20.: A particle passing the depleted zone of a silicon sensor produces pairs of electrons and holes along its track, which drift towards the read-out surface due to electric and magnetic fields. The original hit position is reconstructed from the collected surface charges.

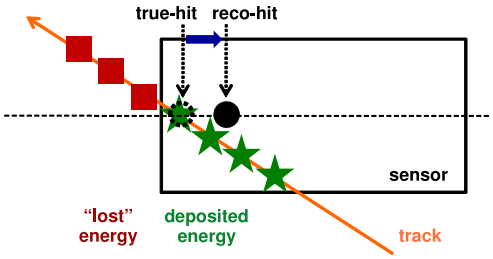

Figure 4.21.: If a particle passes the outer edge of the sensor, a fraction of the hit is lost outside. The produced electron-hole pairs inside cause a hit, shifted in its reconstructed position to the sensor middle.

4.6. Edge Channels

The edge-channels of a silicon sensor are special: a particle hitting the sensor in this region does not traverse it over the entire depth, depending on its incident angle. Thus, electron-hole pairs are produced only along the fraction of the track inside the sensor (cf. Figure 4.21). As the farthest part of the track is not detectable, the hit will always be reconstructed nearer the sensor middle. From geometrical considerations the number of affected channels can be estimated to one [60]: the first and the last channel of a module are biased with respect to the reconstructed hit position in opposite directions. For single residuals, this bias averages out on module level. Overlap residuals inherit this bias twice since they are located in the opposite edge regions of the two different modules.

The pixel detector shows the expected behaviour (cf. Figure 4.22): the mean of the residuals of the first and last channel (no. 0 and 327) is shifted. Apart from that, there is a repeating pattern of channels with a varying number of hits: channels around a maximum have a clear minimum with some average channels in-between before repetition.

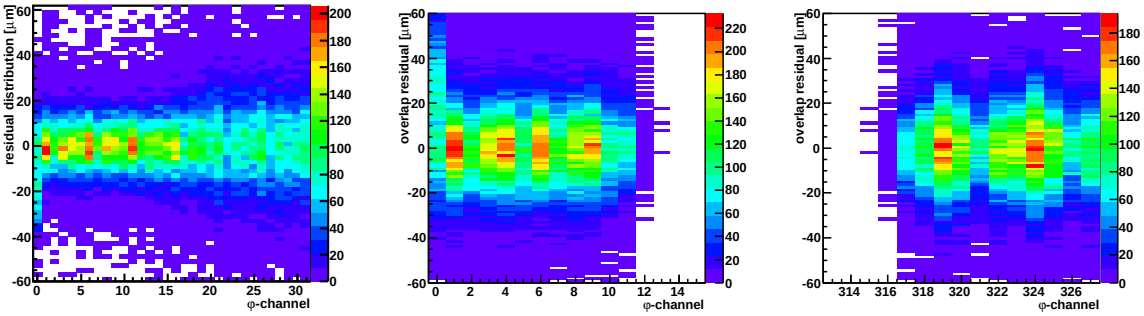

Figure 4.22.: Left: Single residuals of Pixel layer 0 as a function of the φ-channel. **Middle:** Overlap residuals of layer 0 as function of the φ-channel of the inner module. **Right:** Overlap residuals versus the φ-channel of the outer module. - As expected the direct edge channels show a clear bias both for single and overlap residuals.

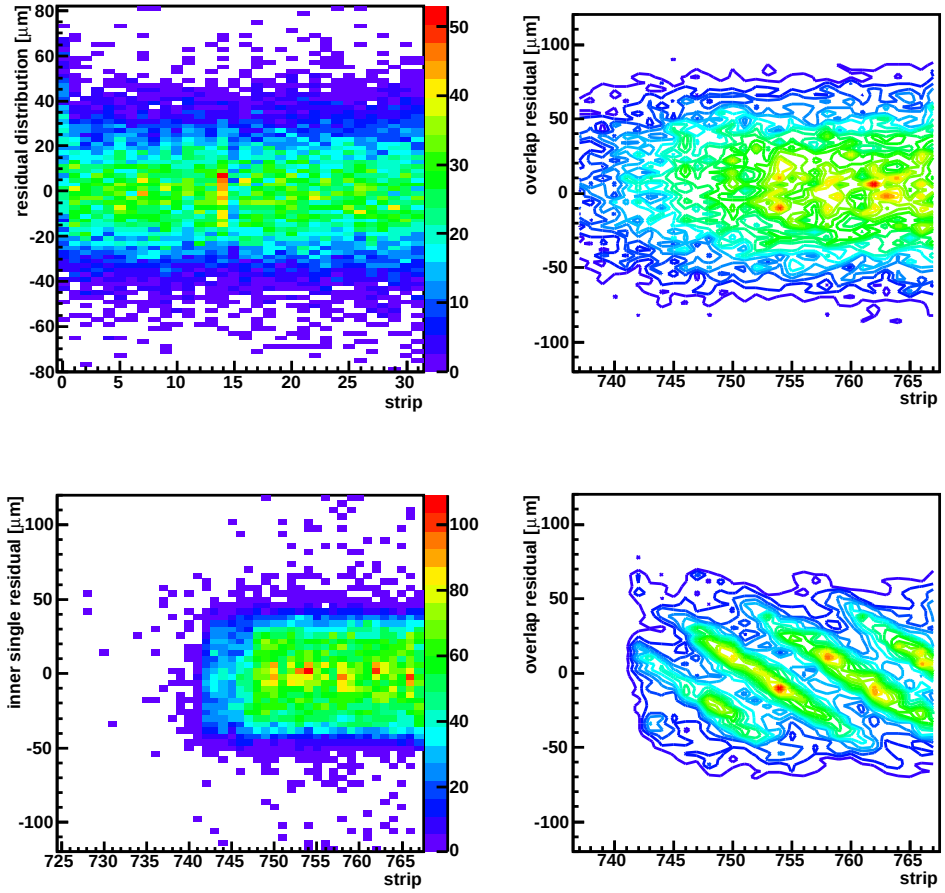

Figure 4.23.: Top left: Single residuals of SCT layer 1 as function of strip no. **Top right:** Overlap residuals of the stereo side as function of strip. **Bottom left:** Only single residuals, which participate in an axial overlap. **Bottom right:** Axial overlaps as function of inner strip number. The overlap mean seems to depend on the strip number with multiple maxima per strip.

The SCT single residuals agree with the expectations as well as the overlap residuals from the stereo side of the modules (cf. Figure 4.23). The overlap residuals from the axial module side also show a bias in the edge channels. However, the overlap mean depends on the strip number with multiple maxima per strip. This behaviour is found in all SCT axial layers and will be discussed further in Section 4.8.

Concluding, the residuals measured by the edge channels of the silicon modules are intrinsically biased. This bias could be removed by excluding the first and the last channel of a module, but this would severely decrease statistics, as from geometrical definition many overlap residuals are situated in this region. Yet, even with this edge cut the overlap residual distribution as a function of layer still deviates from zero (cf. Figure 4.24).

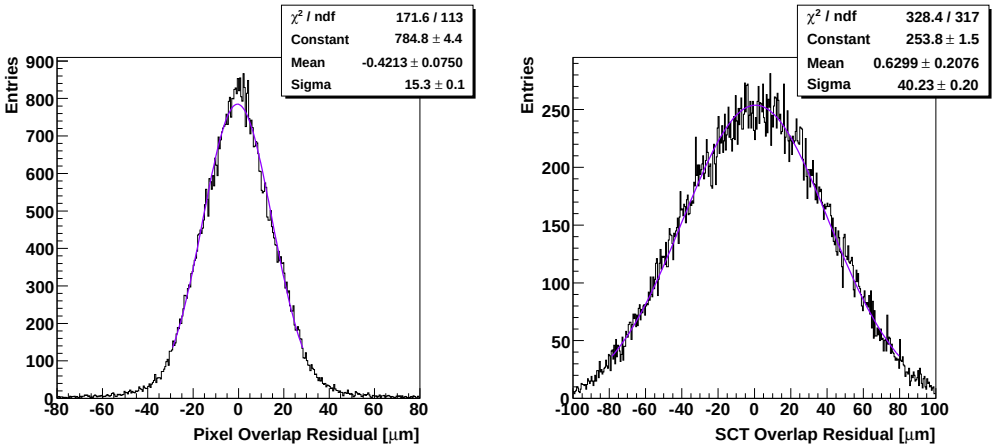

Figure 4.24.: The impact of a simple edge cut on the overlap residual distribution of Pixel layer 1 **(left)** and SCT layer 3 **(right)**. Although the mean of the residuals is influenced severely, it still deviates from zero.

4.7. Studies of the η-Dependency of Pixel Overlap Residuals

In the Pixel detector, there are mainly two effects of special interest: the shifted mean of the overlap residuals and their η-dependency (compare figures 4.2 and 4.5).
The process of *Digitization* is studied in detail (cf. Section 4.5): A particle traversing a silicon sensor typically creates pairs of electrons and holes, which are collected at its surface and from which the hit position must be reconstructed. With the silicon tracker being located in a 2 T magnetic field, the tracking algorithms must compensate the impact of this field - any imprecision concerning silicon properties or magnetic field could cause systematic discrepancies.

4.7.1. Lorentz Drift and -Corrections

The lateral deviation of the drifting charges inside the silicon sensors, caused by the external magnetic field, needs to be corrected for during the reconstruction in order to determine the

exact hit position. For Monte Carlo data, the primary Lorentz drift of the charges is introduced during the digitisation first.

In order to examine overlap residuals with respect to Lorentz drift and correction, the effects of the magnetic field on the silicon sensors (both in the digitisation and in the reconstruction procedure) can be switched off while the rest of the detector is unaffected (tracks are still bent etc.). The notation is defined as follows: *std* for usual field, *nf* for no field, lower cases for digitisation, upper cases for reconstruction.

In the *nfNF* data sample, the magnetic field in the silicon sensors is completely switched off. Several differences between the *stdSTD* sample (compare section 4.2) and the *nfNF* data are found (figure 4.25):

- The overlap residual distributions are still shifted, but the amount of shift changes without identifiable pattern. E.g. the shift of the overlap residuals of the entire Pixel layer 1 increases from (-0.4006 ± 0.0739) μm to (-0.5143 ± 0.0873) μm, while the shift of SCT layer 3 decreases from (1.046 ± 0.201) μm to (0.8105 ± 0.1777) μm.
- The correlation between inner and outer residual nearly vanishes in the Pixel detector. For example, the correlation coefficient of overlap residuals decreases from -0.2909 to -0.1385 (layer 1).
- The η-dependency of Pixel overlap residuals vanishes for all three pixel layers.
- The error-ratio $\sigma_{hit}/\sigma_{track}$ changes its shape and decreases clearly in the Pixel detector. E.g. the mean of the error ratio decreases from 0.7354 to 0.3893 (layer 1) in agreement with the decreasing correlation coefficient.

In order to classify the phenomena and distinguish between digitisation- and reconstruction effects, also samples with inconsistent magnetic field are taken into account: "stdNF" and "nfSTD". This inconsistency is expected to create a systematic bias in the overlap residuals, which is directed in opposite directions (cf. Figure 4.26). Although the distributions have a slightly different shape, no additional shift is found but the η-dependency is more pronounced.

Furthermore, it should be stated, that without Lorentz drift and correction the characteristic dependence of overlap residuals versus strip-number in the SCT detector decreases noticeably (cf. Figure 4.27).

Obviously, the Lorentz correction does influence especially overlap residuals in the Pixel detector severely (cf. Figure 4.25). Both the η-dependency of Pixel overlaps and the correlation between the hits forming an overlap depends directly on the Lorentz corrections - without magnetic field in the silicon sensors, it vanishes.

4.7.2. Diffusion

Besides the drift of the electrons due to electric and magnetic fields, a diffusion takes place perpendicular to the drift direction [67].

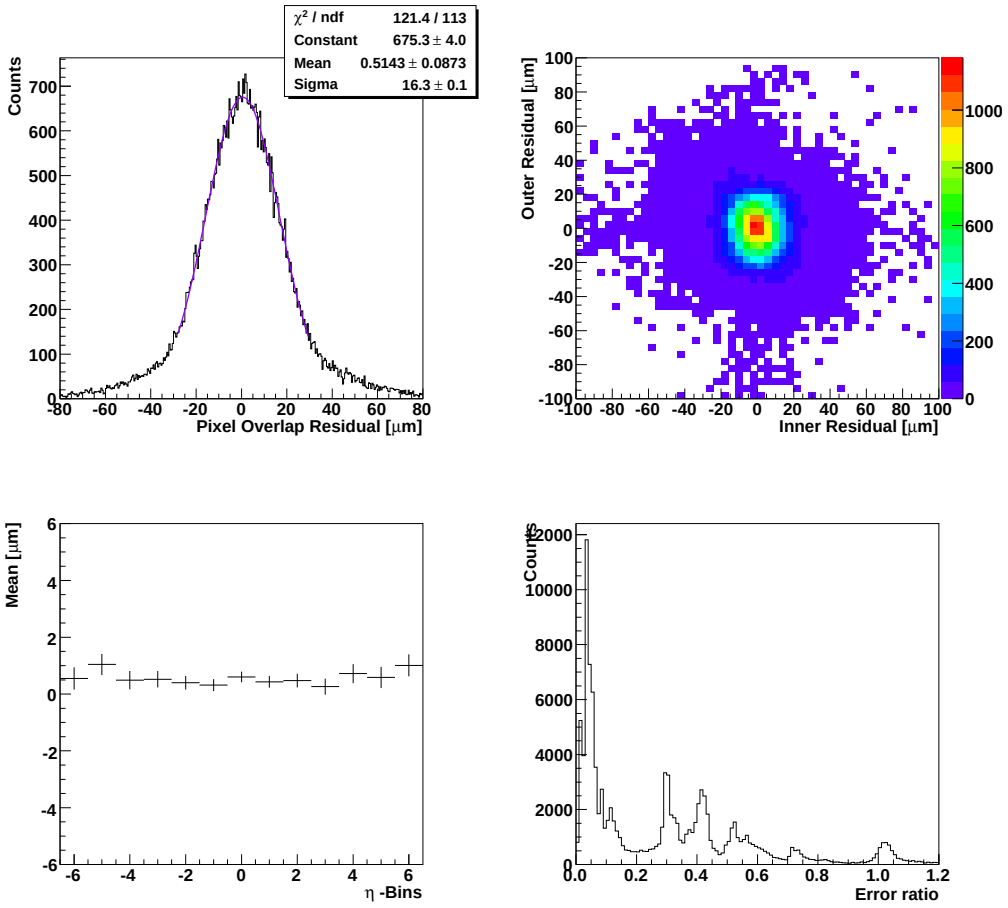

Figure 4.25.: The absence of a magnetic field in the silicon sensors during digitisation and reconstruction changes the behaviour of overlap residuals significantly - exemplary for Pixel layer 1. **Top left:** Distribution of complete layer is still shifted. **Top right:** Inner and outer residual seem uncorrelated now and the correlation coefficient decreases to -0.3893. **Bottom left:** Overlap residuals as function of module-η coordinate are shifted, but flat. **Bottom right:** The shape of the error ratio changes significantly and its mean decreases to 0.3593.

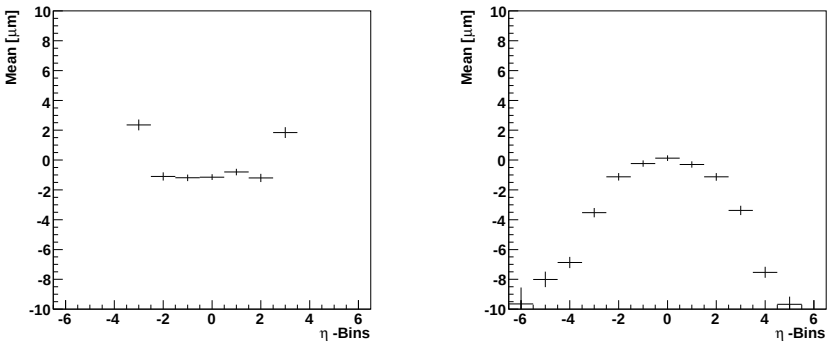

Figure 4.26.: Mixed magnetic field settings for digitisation and reconstruction - exemplary on Pixel layer 0. **Left:** *nfSTD* **Right:** *stdNF*. There are small deviations in the shape of the distributions, but the shifts are directed oppositely as expected.

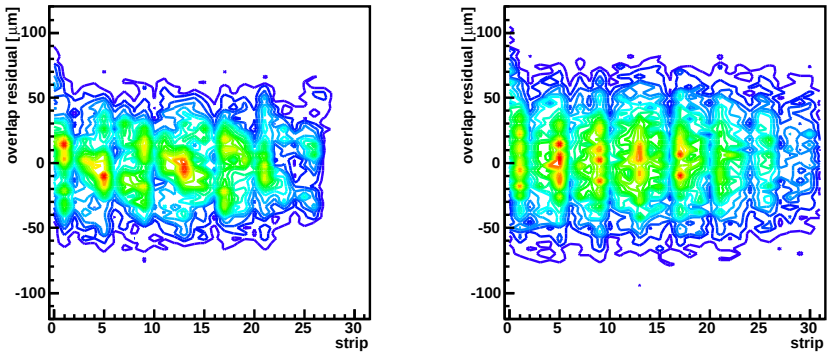

Figure 4.27.: Overlap residuals as a function of the strip number on SCT layer 1 exemplarily, for axial **(left)** and for stereo **(right)** overlap residuals. The characteristic dependence of the overlap residual mean on the strip number decrease noticeably without the impact of the magnetic field.

Fick's laws are the starting point, ρ being the charge density and D the diffusion constant.

$$\dot{\rho} = D \cdot \nabla^2 \rho \tag{4.8}$$

Let the initial charge distribution be oriented parallel to the wafer surface with a Gaussian shape,

$$\rho = \frac{N}{2\pi \cdot \Sigma^2} \cdot \exp\left(-\frac{r^2}{2\Sigma^2}\right) \tag{4.9}$$

N being the number of drifting charges and Σ being the time-dependent Gaussian width (*diffusion radius*), $\Sigma\,(t=0) = \Sigma_0$.

$$\begin{aligned}
\dot{\rho} \overset{(4.9)}{=} & \quad \tfrac{N}{2\pi}\left(-\tfrac{2\dot{\Sigma}}{2\Sigma^3}\right)\exp\left(-\tfrac{r^2}{2\Sigma^2}\right) \quad + \frac{N}{2\pi\Sigma^2}\left(\frac{-r^2}{2}\frac{-2\dot{\Sigma}}{\Sigma^3}\right)\exp\left(-\frac{r^2}{2\Sigma^2}\right) \\
= & \qquad \rho \cdot \left[-\tfrac{\dot{\Sigma}}{\Sigma^3}\right] \qquad\qquad + \rho \cdot \left[\frac{r^2\dot{\Sigma}}{\Sigma^3}\right] \\
= & \qquad -\rho \cdot \tfrac{\dot{\Sigma}}{\Sigma}\left(1 - \tfrac{r^2}{\Sigma^2}\right)
\end{aligned} \tag{4.10}$$

The Laplace-operator in spherical coordinates

$$\nabla^2 f = \frac{1}{r^2}\frac{\partial}{\partial r} r^2 \frac{\partial f}{\partial r} + \cdots \frac{\partial f}{\partial \vartheta} + \cdots \frac{\partial f}{\partial \varphi^2}$$

leads to

$$\begin{aligned}
\frac{\partial \rho}{\partial r} &= \frac{N}{2\pi\Sigma^2}\exp\left(-\frac{r^2}{2\Sigma^2}\right)\cdot\left(-\frac{2r}{2\Sigma^2}\right) = -\rho\cdot\left(\frac{r}{\Sigma^2}\right) \\
\Rightarrow \quad \frac{1}{r^2}\frac{\partial}{\partial r}\left(r^2\frac{\partial \rho}{\partial r}\right) &= -\frac{1}{r^2\Sigma^2}\cdot\left[r^2\rho + r^3\rho\left(-\frac{r}{\Sigma^2}\right)\right] \\
&= -\frac{\rho}{\Sigma^2}\left[1 - \left(\frac{r}{\Sigma}\right)^2\right]
\end{aligned} \tag{4.11}$$

and finally

$$\begin{aligned} -\rho \cdot \frac{\dot{\Sigma}}{\Sigma} \quad \left(1 - \tfrac{r^2}{\Sigma^2}\right) \quad &\overset{(4.8,\,4.10,\,4.11)}{=} D \cdot \left[-\frac{\rho}{\Sigma^2}\left(1 - \left(\frac{r}{\Sigma}\right)^2\right)\right] \\ \Rightarrow \quad \dot{\Sigma} = \quad & {}^{D}/_{\Sigma} \\ \Rightarrow \quad \Sigma\,(t) = \quad & \sqrt{2Dt + \Sigma_0^2} \end{aligned} \tag{4.12}$$

From geometrical considerations (cf. Figure 4.20), a relation between the original drifting distance ΔZ and the new one d_{lor} is given by the Lorentz angle ϑ_{lor}.

$$\begin{aligned} d_{lor}^2 = \quad & (\Delta x)^2 & + (\Delta Z)^2 \\ = \quad & (\Delta Z \cdot \tan(\vartheta_{lor}))^2 & + (\Delta Z)^2 \\ \Rightarrow d_{lor} = \quad & \Delta Z \cdot \sqrt{1 + \tan^2(\vartheta_{lor})} & \end{aligned} \tag{4.13}$$

Assuming a typical electron drifting time of about 5 ns to traverse a silicon sensor completely and an initial delta function-like charge distribution at $t = 0$, a typical diffusion radius is given by

$$\Sigma(t \approx 5\text{ ns}) \overset{(4.12)}{=} \sqrt{2\mathrm{Dt} + 0} \approx 6\ \mu\mathrm{m}.$$

With respect to the longer drifting time due to the inclined drifting distance, a slightly modified diffusion radius is found.

$$\Sigma_{lor}(t) \overset{(4.12)}{\approx} \sqrt{2D \cdot t_{lor}} \overset{(4.13)}{=} \sqrt{2D \cdot t \cdot \sqrt{1 + \tan^2(\vartheta_{lor})}} \tag{4.14}$$

Equation 4.14 is mostly consistent with the implementation in ATHENA [67], both in the dependence on variables and in the dimension.

$$\Sigma_{ATHENA}(\Delta Z = v_{electrons} \cdot t) = 6\ \mu\mathrm{m} \cdot \sqrt{\frac{\Delta \mathrm{Z}}{0.3}} \cdot \sqrt{1 + \tan^2(\vartheta_{\mathrm{lor}})} \tag{4.15}$$

In order to examine the influence of the diffusion and especially the Lorentz-dependent diffusion on overlap residuals, the diffusion radius inside the Pixel Digitization is scaled with different factors. The Lorentz-dependent fraction of diffusion is scaled with 0.01 and 5., showing no deviations from nominal geometry (cf. Figure 4.28). Obviously, this part of diffusion does not cause the η-dependence of Pixel overlap residuals.

Finally, two different cases are simulated: 1. the whole diffusion switched off and 2. the diffusion is scaled by a factor of 5.0. The width of the overlap distribution of the complete barrel layers (cf. Figure 4.29) decreases slightly without diffusion (e.g. from 14.53 μm to 14.34 μm on Pixel layer 0) and increases noticeably under fivefold diffusion (e.g. to 23.7 μm on Pixel layer 0). While the η-dependency of the overlap residuals is more pronounced with fivefold diffusion (by a factor of 5 approximately), overlap residuals versus module-η flatten completely without diffusion (cf. Figure 4.30).

Concluding, although the Lorentz-dependent part of the diffusion is very small and does not influence the overlap residuals, it is the diffusion itself, which contributes to the unexpected behaviour of overlap residuals at nominal geometry.

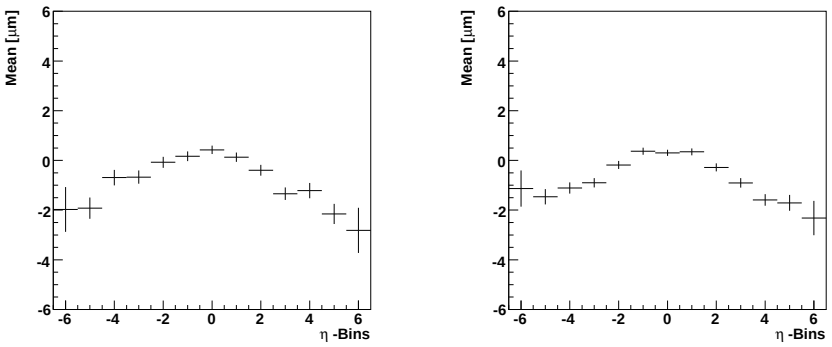

Figure 4.28.: Influence of Lorentz dependent diffusion on the η-dependence of overlap residuals- exemplary on Pixel layer 0. **Left:** Scaled with factor 0.01. **Right:** Scaled with factor 5.0 . Obviously, Lorentz dependent diffusion does not cause this η-dependence.

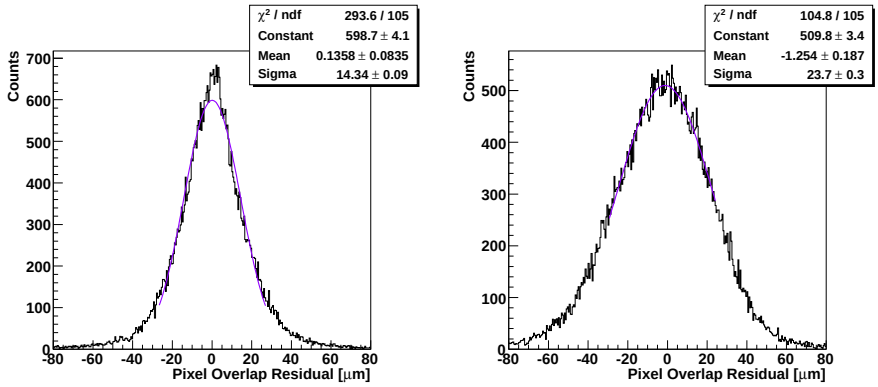

Figure 4.29.: Influence of diffusion on overlap residuals - exemplarily for Pixel layer 0. **Left:** The Gaussian width of the overlap residuals of the entire barrel decreases slightly. **Right:** Scaling the diffusion with a factor of 5.0 increases the Gaussian width of the overlap residuals.

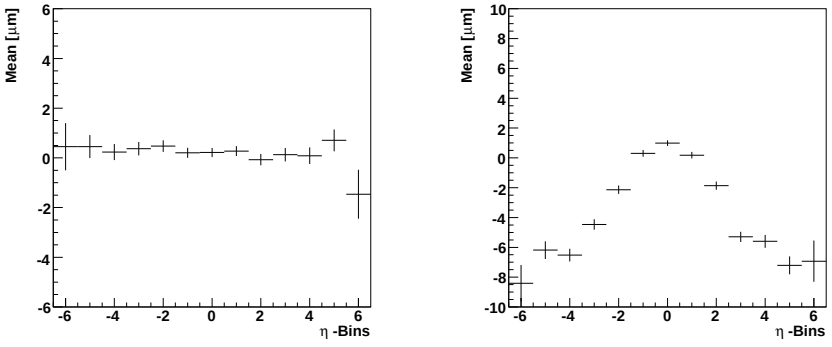

Figure 4.30.: Influence of diffusion on the η-dependence of overlap residuals - exemplary on Pixel layer 0. **Left:** Without diffusion, overlaps as function of module-η are flat. **Right:** Scaling the diffusion with factor 5.0 increases the amplitude of the η-dependence in nearly the same order of magnitude.

4.7.3. Incident Angles

One big difference between modules in the central barrel region (module-$\eta = 0$) and the modules at the edges of the barrel (*module*-$|\eta| = 6$) is the longitudinal incident angle of the tracks. While in the central region the sensors are hit perpendicularly, the longitudinal incident angle at the edge sensors is about $(70 - 80)°$. A simple way to study the influence of this angle on overlap residuals is to move the event vertex.

For this study, the z-component of the vertex is moved to -370.0 mm. On all three layers, the η-dependency of the overlaps is shifted similarly to the vertex, which shows an additional dependence of overlap residuals on the longitudinal incident angle. In the inner layer, the modules on the opposite barrel edge cannot be hit by tracks for geometrical reasons (module inclination, compare section 2.2.3).

Concluding, also the longitudinal incident angle between track and module does influence the overlap distributions and especially their η-dependency.

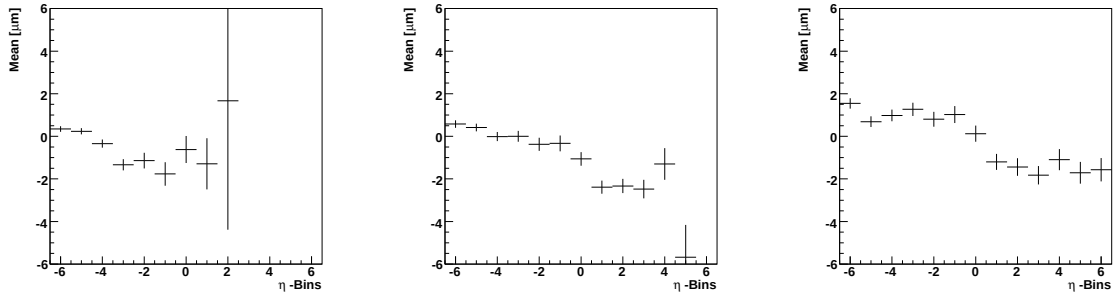

Figure 4.31.: With the event vertex moved along the beam-pipe to the edge of the silicon tracker, the η-dependence of the overlap residuals converts into a sloping straight line on all three layers: **(left)** layer 0, **(middle)** layer 1 and **(right)** layer 2.

4.7.4. The Solenoidal Magnetic Field

In ATHENA the magnetic field is stored inside a dedicated database (*magnetic field map*). Early magnetic field maps contain a theoretically calculated field of an ideal superconducting coil. For later maps, material distortions, hardware dislocations and the influence of magnetic materials inside the detector are taken into account. Finally, thousands of measuring points inside the coil operating distance form the basis to approach the real field. Since 2006 the standard map is *bmagatlas04_test1.data* - including a realistic current for the solenoid (semi-analytical ATLM [71]) inducing a maximum field of 1.96 T at the detector centre and a wire-by-wire description of the toroids.

The solenoidal magnetic field is aligned parallel to the beam pipe and points into the positive z-direction. In the non-central barrel regions, the field diverges radially from the beam pipe (cf. Figure 4.32). The field strength is approximately constant, while the direction of the field changes slightly.

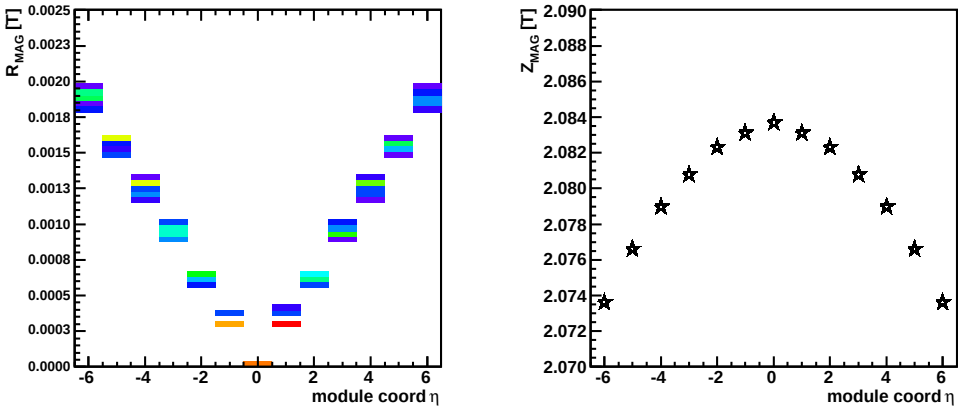

Figure 4.32.: Left: Radial component of the ID magnetic field vector as function of module-η for Pixel layer 0. **Right:** z-component of the magnetic field vector as function of module-η. At the outer barrel edges, the field diverges from the beam pipe.

The Silicon Software needs access to the magnetic field at various times during reconstruction. In order to minimise database access, a constant magnetic field on the scale of a module is assumed: only the value of the magnetic field at the module's centre of gravity is stored as module-based property. This approximation induces two errors which especially concern overlap residuals (see figure 4.33):

"Error Type I"

In the R-φ plane, the edges hit by a particle creating an overlap are situated close together at nearly identical φ-values. Yet, the magnetic field applied to the two edges is different as the modules' centres of gravity are distant. Therefore, overlaps are calculated with different values of the magnetic field, although the same should be used.

"Error Type II"

In the R-Z plane, especially at high η values, the hit positions of the two modules are separated by a large z-distance (the inner module is hit at the front and the outer module at the back). Thus, overlaps are calculated with an identical magnetic field, though different values should be used.

These errors can be approximated by semi-analytical calculations. Let $\vec{t}$ be a straight track creating an overlap between neighbouring modules on Pixel layer 0 at module-$\eta = 6$ and $\varphi \in \{0, 1\}$.

$$\vec{t} = \begin{pmatrix} 0 \\ 0 \\ 0 \end{pmatrix} + \lambda \cdot \vec{r} = \begin{pmatrix} 0 \\ 0 \\ 0 \end{pmatrix} + \lambda \cdot \begin{pmatrix} 0.12744 \\ 0.03540 \\ 0.99121 \end{pmatrix} \tag{4.16}$$

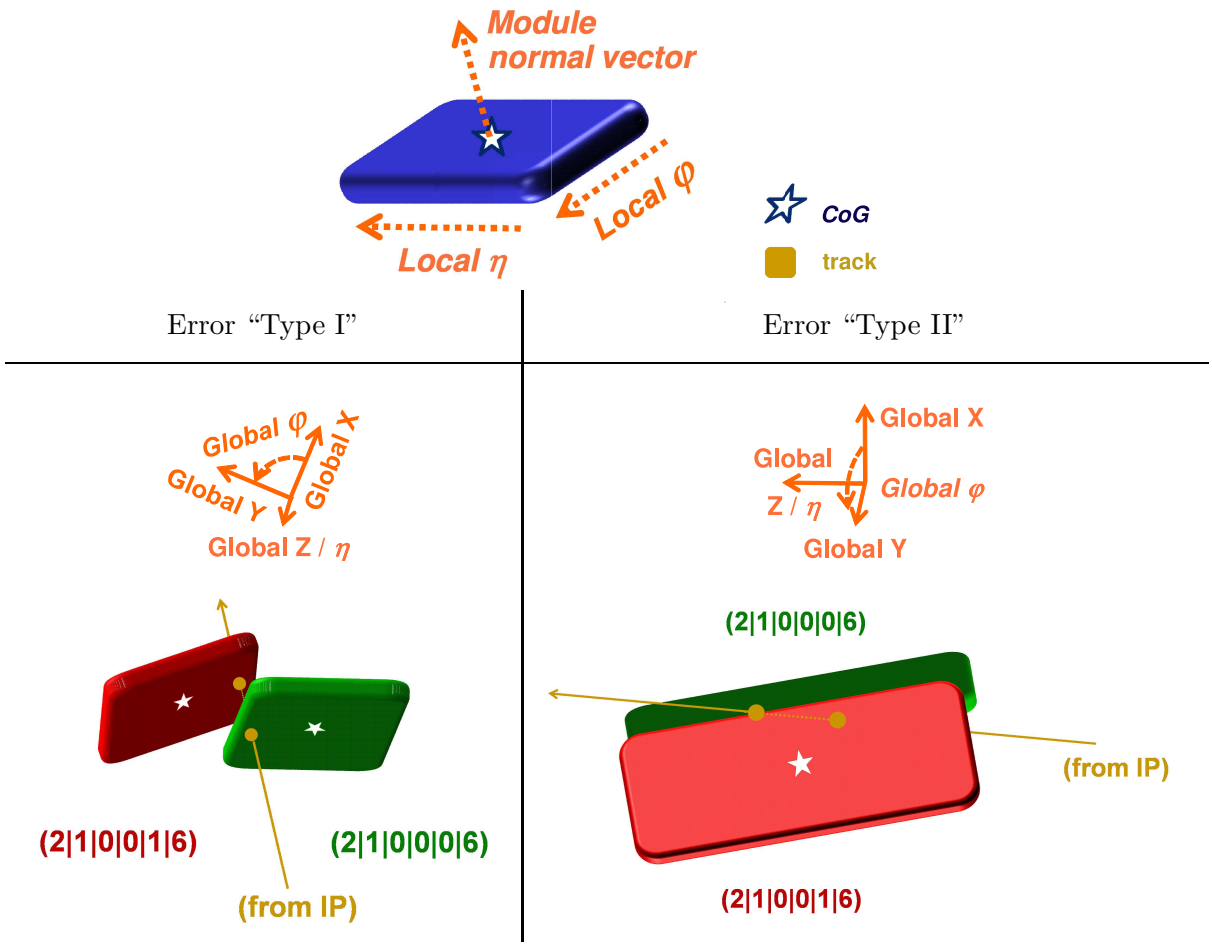

Figure 4.33.: Due to the assumption of a constant magnetic field on module scale, two additional errors, especially concerning overlap residuals, are introduced. Type I determines the overlap hits with different field values, since the centres of gravity (CoG) of the modules are distant. But in reality, they are exposed to an identical field. Type II calculates the overlap hits with an identical field, although especially in the η-range two different values should be used due to the high z-distance between the hits.

Mathematically, the modules are represented as bounded planes P_x, $x \in \{0, 1\}$,

$$\vec{P}_x = \vec{g}_x + \mu_x \cdot \vec{\varphi}_x + \nu_x \cdot \vec{\eta}_x, \quad |\mu| < 3.02 \text{ cm} \wedge |\nu| < 0.82 \text{ cm} \tag{4.17}$$

by their centres of gravity $\vec{g}$ and three local vectors $\vec{n}$, $\vec{\varphi}$ and $\vec{\eta}$ determing their three-dimensional orientation (cf. Figure 4.33). Numerical values are extracted from ATHENA (cf. Section A.2). Finally, the magnetic field vectors at the module centres are extracted.

Let the electron mobility μ_{hall} be -1395.93 $\mathrm{cm}^2/\mathrm{V{\cdot}s}$. The tangent of the Lorentz angles is

separated by its φ- and η-component and calculates to:

$$\begin{aligned}
&\tan_v(\vartheta_x) = \mu_{hall,\,electrons} \cdot [(\vec{\varphi} \times \vec{\eta})_x \times \vec{m}_x] \cdot \vec{v}, \quad \vec{v} \in \{\vec{\varphi}_x, \vec{\eta}_x\} \\
&\tan_\varphi(\vartheta_0) \approx -0.28940775 \\
&\tan_\varphi(\vartheta_1) \approx -0.28940752 \\
&\tan_\eta(\vartheta_0) \approx \quad 0.00011443 \\
&\tan_\eta(\vartheta_1) \approx \quad 0.00010442
\end{aligned} \tag{4.18}$$

As the η-component of the Lorentz angle is significantly smaller than the φ-component, it is completely neglected.

In comparison, the intersections between track and modules are calculated exemplary and the realistic field at these points is chosen in order to approximate the uncertainties of the Lorentz angle calculation. The planes $P_x, x \in \{0, 1\}$ are transfered into parametric form, giving the intersections between the planes and the track as

$$\vec{P}_x : (\vec{\varphi}_x \times \vec{\eta}_x) \cdot \begin{pmatrix} x \\ y \\ z \end{pmatrix} = d_x \quad \rightsquigarrow \quad d_x = \vec{n}_x \cdot \vec{g}_x$$

$$\Rightarrow \quad (\vec{\varphi} \times \vec{\eta})_x \cdot \vec{t} = (\vec{\varphi} \times \vec{\eta})_x \cdot \lambda_x \vec{r} = d_x \rightsquigarrow \lambda_x = \frac{d_x}{(\vec{\varphi} \times \vec{\eta})_x \cdot \vec{r}} \tag{4.19}$$

The z-component of the intersections differs by about 3.2 cm (cf. Equation A.3). With the true values of the magnetic field, the tangent of the Lorentz angle is recalculated:

- Precise field values in x,y:

$$\tan_\varphi(\vartheta_0) \approx -0.28940759, \quad \tan_\varphi(\vartheta_1) \approx -0.28940760 \tag{4.20}$$

- Precise field values in z:

$$\tan_\varphi(\vartheta_0) \approx -0.28919546, \quad \tan_\varphi(\vartheta_1) \approx -0.28946379 \tag{4.21}$$

- Precise field values in all coordinates:

$$\tan_\varphi(\vartheta_0) \approx -0.28919529, \quad \tan_\varphi(\vartheta_1) \approx -0.28946387 \tag{4.22}$$

The deviation

$$\Delta = 100 \cdot (1 - {}^{\tan\vartheta_{calc.}}/_{\tan\vartheta_{ATHENA}})$$

between Equation 4.20 and Equation 4.18 is a measure for the maximum magnetic field error type I of the tangent of the Lorentz angle and is about $6 \cdot 10^{-5}$ %. The error type II is represented by Equation 4.21 and Equation 4.18. It is estimated to about 0.07 %. Finally, the total error of the Lorentz angle calculation (4.22 and 4.18) due to the algorithms used adds up to 0.07 %.

Concluding, the special treatment of the magnetic field in the Inner Detector software causes a bias due to approximations. Nevertheless, these uncertainties do not suffice to explain the observed overlap effects. For simulated events, the software only takes error type I into account, which is sufficiently small.
But especially for real data error type II, which is bigger by a factor of 1,000, is expected to arise. Therefore, the impact of this approximation needs to be estimated in detail.

4.7.5. Combining Lorentz Angle, Diffusion and Incident Angle - Noise Cuts

The fact that Lorentz effects and diffusion as well as the longitudinal incidence angle influence the η-dependency of overlap residuals severely, motivates a more detailed study of the Digitization. The drifting charges, produced by a traversing particle, are collected pixel-wise on the sensor surface and a noise cut is applied.
Typically, a hit in the detector centre consists of about $30,000$ drifting charges, and at the outermost parts of the barrel of $75,000 \cdot e^-$, which disperse on several neighbouring pixels. Due to Lorentz effects and diffusion, the charge cloud is widened and a radial track finally leads to a normal cluster width of 2-4 pixels in φ. The η-size depends strongly on the longitudinal incident angle and can reach up to 6-7 pixels. The threshold of the noise cut is assumed to be $4,000 \cdot e^-$.

Assuming a very flat track and a uniform distribution of surface charges, cluster sizes of 4×5 pixels and more are possible, leading to a ratio of 3,750 charges per single pixel - near or below the noise threshold.
Systematically hits with huge cluster sizes could be rejected as well as especially small asymmetric tails of the surface charge distributions, created by diffusion or magnetic field. This could introduce a bias. Yet the noise cuts are inevitable for a reliable performance of the trackers.

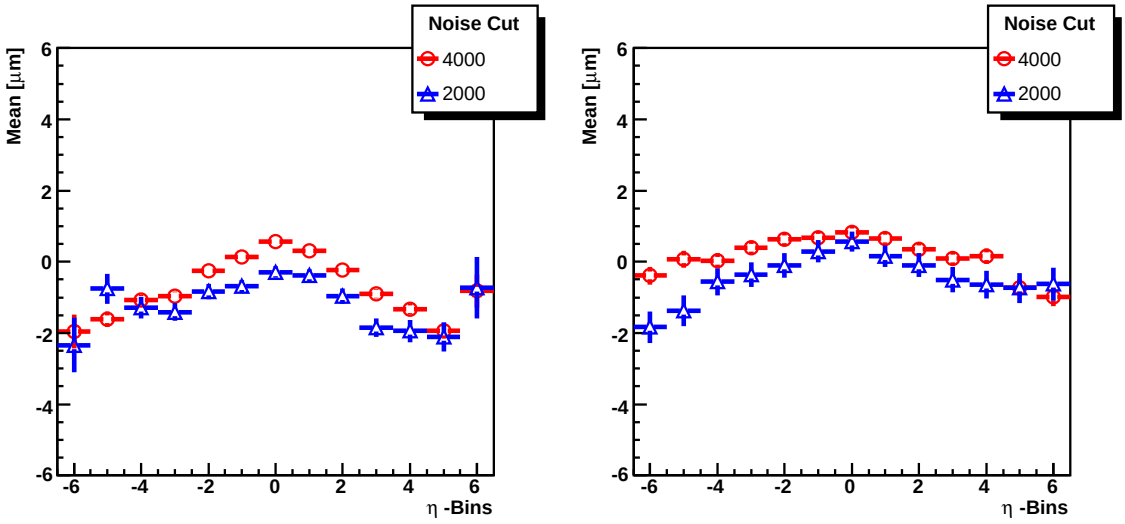

Figure 4.34.: The overlap residual mean as a function of module-η is shown for Pixel layer 0 **(left)** and Pixel layer 2 **(right)**. A smaller noise threshold ($2,000 \cdot e^-$) seems to increase the systematic η-dependency of overlap residuals slightly by about 0.5 μm.

In order to examine the influence of the noise cut, the noise threshold of the Pixel detector is lowered from $4,000 \cdot e^-$ to $2000 \cdot e^-$ in ATHENA, which is expected to decrease its influence and minimise the observed effects.
No decrease of shifts is found (cf. Figure 4.34), but rather it seems to increase slightly (about $O(1\ \mu\text{m})$ for Pixel layer 0). Obviously, the noise cut does influence overlap residuals in the pixel detector. But for further studies this process is separated from the full ATHENA simulation.

4.7.6. Toy Monte Carlo Simulating Pixel Digitization

For a more detailed study of the digitisation an independent Monte Carlo simulation of the digitisation procedure is implemented. In order to simulate overlaps in all η-ranges, the simulated geometry consists of Pixel modules of two neighbouring half-staves in layer 0, ATLAS-Identifiers $(2|1|0|0|\{0;1\}|\{0;...;6\})$ according to ATHENA 12.0.5 with CSC-00-00-00 geometry. For reasons of computational costs and symmetry, the results of positive η-values are mirrored to negative ones. Straight tracks from a common vertex are assumed with a flat distribution in η and φ. The parameters of the Pixel modules comply with ATHENA. The charges collected on the sensor surface are electrons and the Lorentz angle ϑ_{Lor} is approximated with 20°. The sensor thickness of 250 μm is assumed to be fully depleted and the noise threshold for surface charges is $4000 \cdot e^-$.

First, the particle is propagated through the detector, and the external hit parameters, such as hit position and incident angles are calculated and transfered to a local module-frame. With this information, electrons are created along the track inside the silicon sensor. Every single electron is projected on the read-out-surface taking into account Lorentz angle and diffusion. The surface charges are binned according to the Pixel size and the noise cut is applied. In addition, also the true hit data (quasi-infinite binning of the sensor) and data without the noise cut are stored. The centre and width of the charge cluster is calculated and propagated back into the measuring plane. Afterwards the residuals are determined (i.e. the difference between the original hit and the calculated charge centre).
The following features are implemented:

- The deposition of energy along the track is split into 2000 steps.
- The number of produced electrons scales with the traversing length of the particle ($30000 \cdot e^-$ for module-$\eta = 0$ and $75000 \cdot e^-$ for module-$|\eta| = 6$).
- All calculations are done in a plane at the middle of the sensor.
- Particles can leave the sensor edgewise, drifting charges cannot.
- Let z_d be the actual depth of the particle, then the Lorentz drift in x-direction is given by:
$$x_{Lor} = z_d \cdot \tan(\vartheta_{Lor})$$
- The Lorentz-drift in y-direction is neglected because of $B_{xy} \approx 0$ T.
- The diffusion radius r_{diff} is given by Equation 4.15.
- Let $(x_{el}|y_{el}|z_d)$ be the origin of an drifting electron. Its surface position then is given by:
$$x_{surf}\text{Gaussian distributed, } \mu = (x_{el} + x_{Lor}),\ \sigma = r_{diff},$$
$$y_{surf}\text{Gaussian distributed, } \mu = y_{el},\ \sigma = r_{diff}.$$
- True (*analogue*) and *digitised* cluster centres μ_{cl} (with/without noise cut) are calculated as weighted mean and propagated back from the surface to the measuring plane.
- Let $(x|y)$ be the true hit position in the measuring plane. Then the φ-residual is calculated as
$$res = \left(\mu_{cl} - \frac{1}{2}x_{Lor}\right) - x. \tag{4.23}$$

In a typical surface charge distribution (cf. Figure 4.35, left), the majority of the electrons are concentrated in a small region in the cluster middle while at the cluster edges only few electrons (≤ 500 per pixel) are found. Larger incident angles (i.e. high η-values) stretch the distribution over several pixels (cf. Figure 4.35, right).

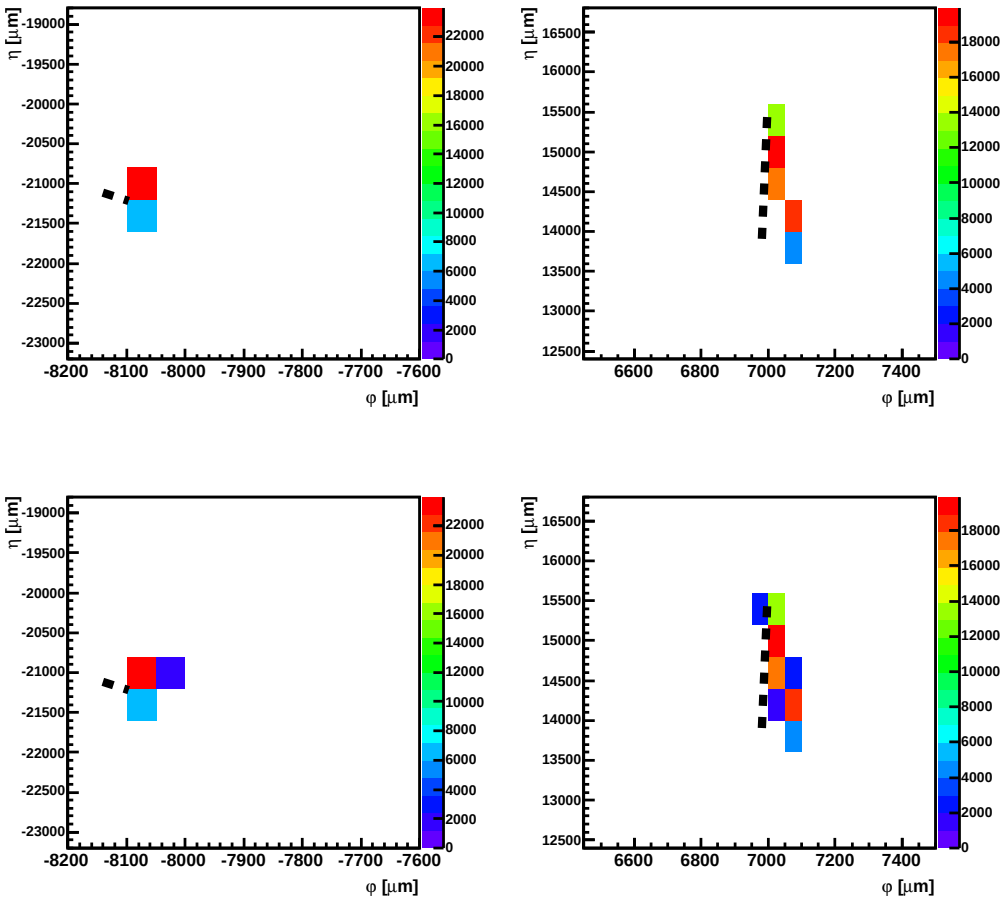

Figure 4.35.: The dashed line is the true track position. **Top left:** The tracks hit the sensors nearly perpendicular in the central barrel region. The cluster width in η typically adds up to 1-2 pixels. **Top right:** At high η values, the tracks hit the sensors very flat and typical incident angles are about $(70 - 80)°$. The clusters can extend over more than 4 pixels in η-direction. **Bottom:** The same without the noise cut.

The toy Monte Carlo is tested in several scenarios with respect to magnetic field, diffusion, detector geometry and edge channels. First the *normal* case of ATLAS is analysed. Both residuals and overlap residuals show an almost Gaussian shape and their width is of the expected order of magnitude ($(10 - 20)$ μm, cf. Figure 4.36). While all residuals show no φ-dependency, the same dependency on η, both in size and shape, as observed in ATHENA is seen (cf. Figure 4.37) Between inner and outer residual, no obvious correlation is found. But various overlap residuals exist with the residual distribution of one single residual being significantly narrower than the other (cf. Figure 4.38), which is caused by modules with high η.

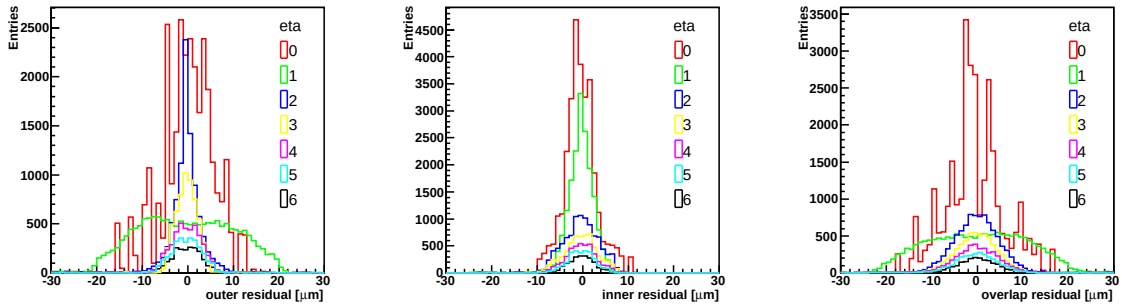

Figure 4.36.: Left: Residuals of the inner module. **Middle:** Residuals of the outer module. **Right:** Resulting overlap residuals - the distributions are of Gaussian shape almost and correspond well to the full detector simulation.

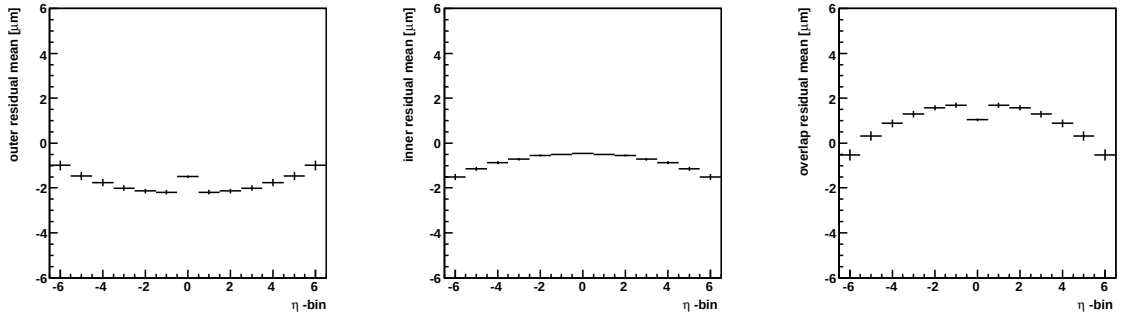

Figure 4.37.: Left: Residuals of the inner module as function of module-η. **Middle:** Residuals of the outer module as function of module-η. **Right:** Overlap residuals as function of module-η. Single residuals are slightly shifted while overlap residuals reflect an η-dependence of at least 2 μm size.

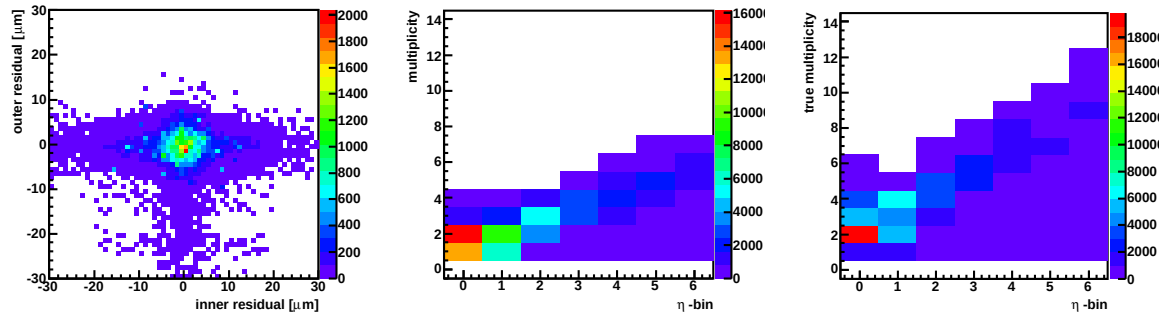

Figure 4.38.: Left: No obvious correlation is found between inner and outer residual. But various overlap residuals exist with the residual distribution width of one single residual being narrower than the other. **Middle:** Multiplicity of outer module as function of module-η. **Right:** True multiplicity of outer module (without noise cut) as function of module-η. At higher η-values, the typical hit multiplicities increase as expected.

The noise threshold cutting away pixels with too small collected charge is expected to change the pixel multiplicity (number of pixels per hit) substantially (cf. Figures 4.35 and 4.38). Indeed, the multiplicity decreases by $2-5$ pixels. Yet, the number of hits with a very small multiplicity, especially in high η-ranges, is larger than expected and will be discussed later.

Next, the influence of the diffusion is estimated by de-/increasing the diffusion radius. Without diffusion, the barrel-wide distributions do not change significantly, and also the η-dependence does not vanish (in contrast to ATHENA). But the multiplicity decreases by 1-2 pixels, since the diffusion widens the surface charge distribution (cf. Figure 4.39).
With applying a five-fold diffusion, the barrel-wide residual and overlap residual distributions are distorted and especially the true hit multiplicity increases clearly (cf. Figure 4.40) as well as the characteristics of the η-dependency - in agreement with ATHENA (cf. Figure 4.30).

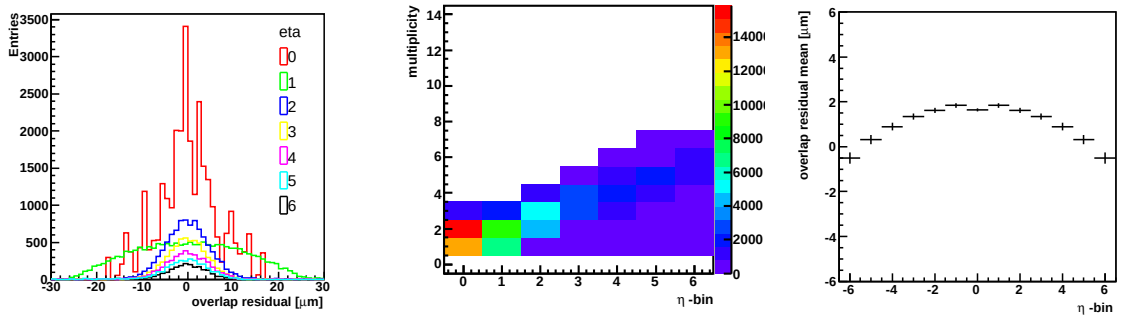

Figure 4.39.: Left: Without diffusion, overlap residuals are still Gaussian-shaped. **Middle:** The hit multiplicity decreases, as diffusion normally smooths and widens the surface charges. **Right:** The η-dependence of overlap residuals does not vanish (contrary to ATHENA).

The impact of different Lorentz angles is tested. Lorentz angles between $\{-20,\ldots,20\}^\circ$ are chosen.
As module inclination and normal Lorentz angle are adjusted to each other in order to minimise the φ cluster size of radial tracks, the overlap residual distributions of a whole barrel (cf. Figure 4.41) are clearly affected by not-fitting Lorentz values. E.g. the typical φ cluster size changes from 2 pixels at normal parameters up to 8 pixels for opposite magnetic field. However, without Lorentz drift and correction, the η-dependency vanishes, while the amplitude decreases with half Lorentz corrections by a factor of 2 and - except for small shape changes - the η-dependency for opposite magnetic field is reversed (cf. Figure 4.42).

The influence of the geometry is tested with respect to the different surface charge distributions. The Pixel modules do not only overlap in φ but also in η-direction with a longitudinal inclination angle of a few degrees. Changing this η-angle to 0° increases the η-dependency of overlap residuals slightly ($O(< 0.5\ \mu\text{m})$), which is explicable by the higher longitudinal incident angles between the track and the modules at $\eta \neq 0$.
For the module inclination angle α, values between -30° and $+20^\circ$ (normal detector design) are chosen. Obviously, the η-dependency of the overlap residuals does depend on the module inclination α additionally (cf. Figure 4.43). Its amplitude decreases with smaller module inclination and finds a minimum at -20°. At lower angles it increases again. It should be noted, that these effects do not change with opposite Lorentz angle.

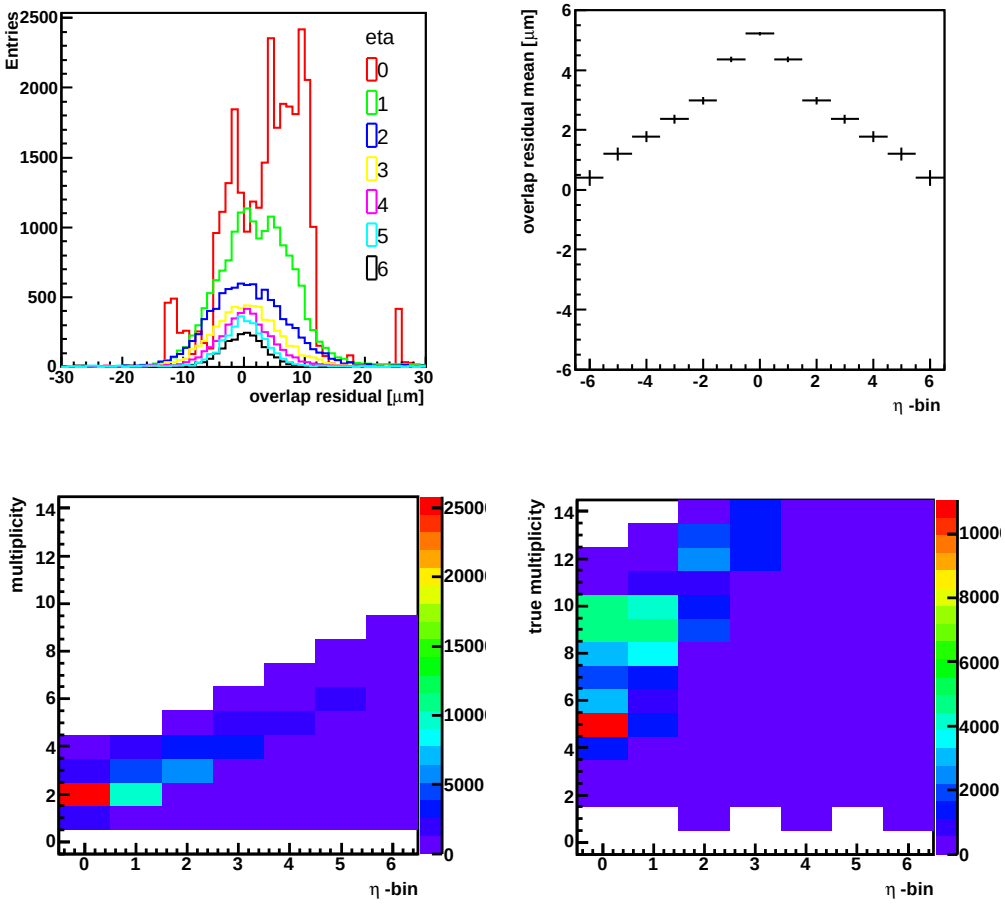

Figure 4.40.: Top left: With fivefold diffusion, the shape of the overlap residuals is distorted as the surface charge distribution is extremely widened. **Top right:** The η-dependency of overlap residuals increases by a factor of 5. **Bottom left:** Although the effective hit multiplicity is very similar to the normal case, the true hit multiplicity (**bottom right**) confirms the widening of the surface charges clearly.

As the geometry itself is already excluded as the origin of the η-dependency of Pixel overlap residuals (cf. Section 4.3.1), the reason for the observed changes of the toy MC must be found in different charge distributions inside the silicon sensors.

As has been shown already, the noise cut itself does not create the η-dependence of overlap residuals - it can increase existing deviation at most. As further cross-check, the lowering of the noise threshold from $4000e^-$ to $2000e^-$ is simulated. In accordance with ATHENA, the barrel-wide overlaps do not change significantly, while the η-dependency is even increased by a factor of 1.5 (cf. Figure 4.44).

Concluding, the reduced toy Monte Carlo of the Pixel Digitization reproduces many of the characteristics seen in the ATHENA overlap residuals at nominal geometry (especially the η-dependency of overlap residuals, cf. Section A.3). Thus, these effects are apparently not the result of any severe errors inside the complex software environment ATHENA. Despite of a

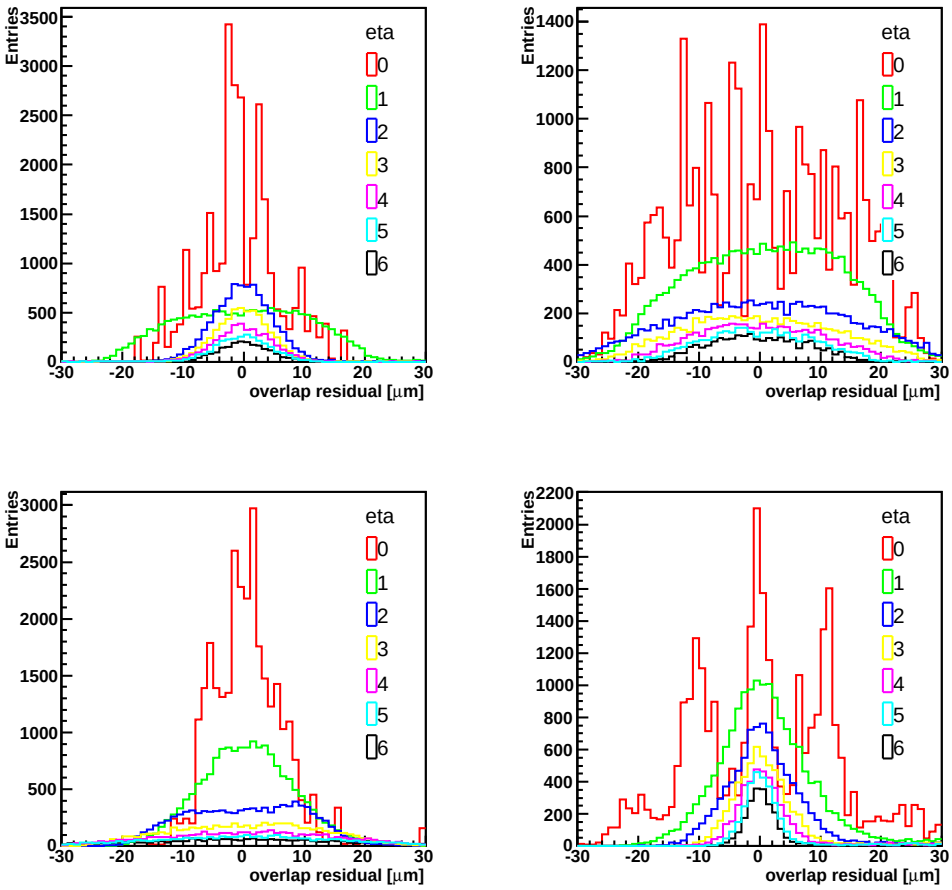

Figure 4.41.: Overlap residuals of the entire barrel for different Lorentz angles: **Top left:** $\vartheta_{Lor} = -20°$, normal field. **Top right:** $\vartheta_{Lor} = -10°$, only half magnetic field. **Bottom left:** $\vartheta_{Lor} = 0°$, without magnetic field. **Bottom right** $\vartheta_{Lor} = +20°$, opposite magnetic field. The structure of the overlap residuals at the opposite magnetic field is a result of a combination of the high hit multiplicity and the applied noise cut.

few small disagreements (i.e. the case without diffusion) the toy MC is sufficient to be used for further studies, especially of the η-dependency of overlap residuals.

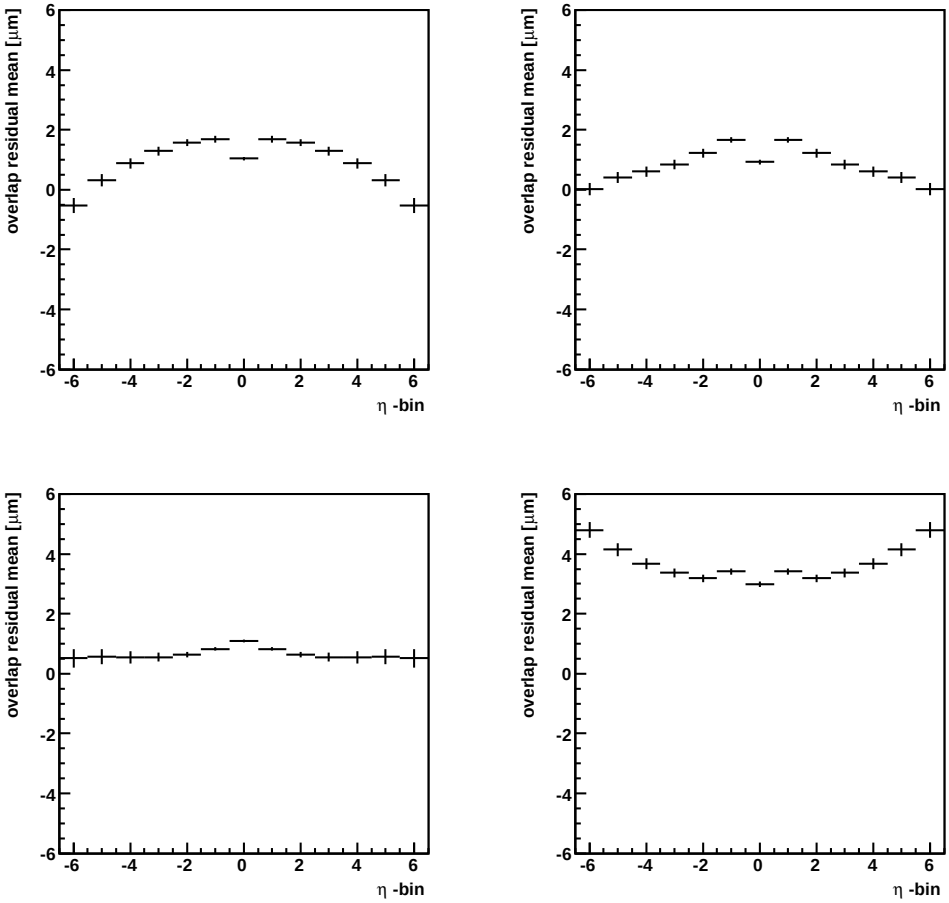

Figure 4.42.: Distribution of the overlap residuals versus module-η for different Lorentz angles: **Top left:** $\vartheta_{Lor} = -20°$, normal field. **Top right:** $\vartheta_{Lor} = -10°$, only half magnetic field. **Bottom left:** $\vartheta_{Lor} = 0°$, without magnetic field. **Bottom right** $\vartheta_{Lor} = +20°$, opposite magnetic field. - The amplitude of the pattern depends on the Lorentz angle severely and the direction of the structure can even be inversed for an opposite Lorentz angle.

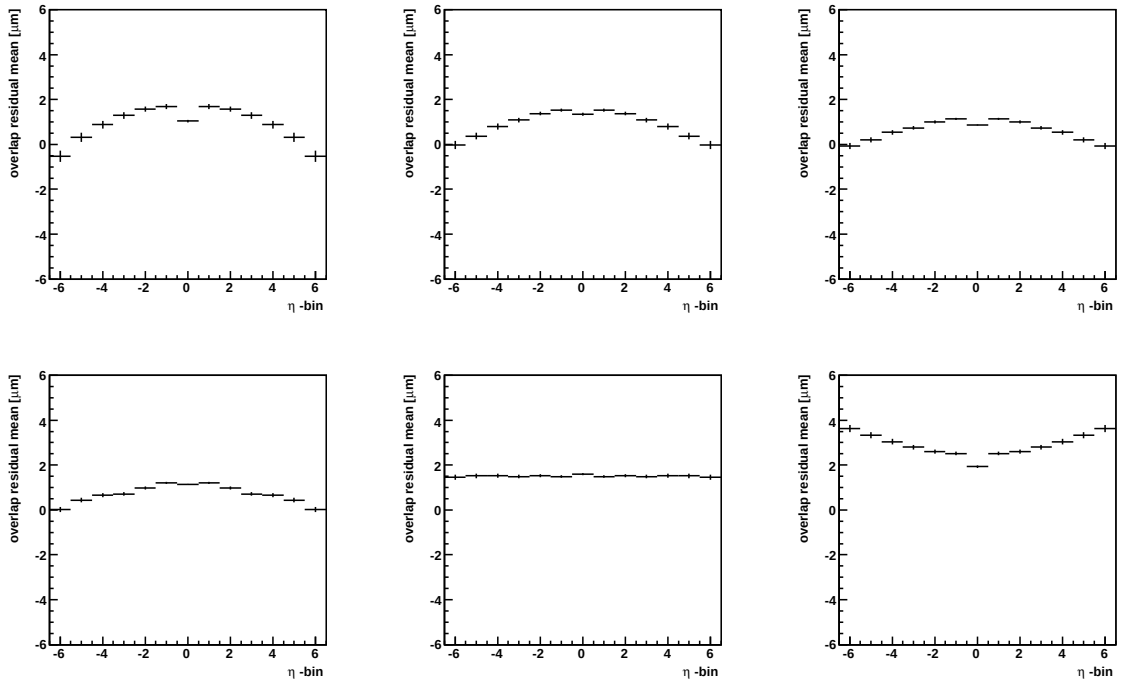

Figure 4.43.: Overlap residual versus module-η as a function of different module inclinations α: **Top left:** $\alpha = +20°$, normal geometry. **Top right:** $\alpha = +10°$, only half inclination. **Top right:** $\alpha = 0°$, no inclination, modules are arranged tangentially. **Top right:** $\alpha = -10°$, half opposite inclination. **Bottom left:** $\alpha = -20°$, opposite inclination. **bottom right** $\alpha = -30°$, bigger opposite inclination. Obviously, the η-dependency of the overlap residuals does depend on the module inclination additionally.

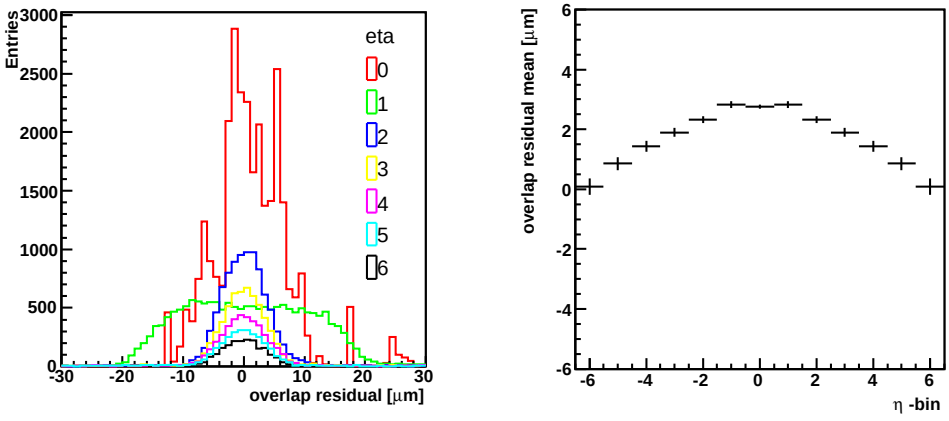

Figure 4.44.: Left: Even with half noise threshold, the barrel-wide overlaps do not change significantly. **Right:** The amplitude of the pattern is increased by a factor of about 1.5 with application of only the half noise threshold. This agrees with the ATHENA studies very well.

4.7.7. Comparison: ATHENA and Toy Monte Carlo

The hit multiplicity as a function of module-η (cf. Figure 4.38) gives an indication of a further unexpected behaviour of overlap residuals. Especially in high η-range various hits with a very small multiplicity are recorded which do not agree with the expectation of an increasing multiplicity at high η values. Furthermore, the mean of the (overlap) residuals as a function of their multiplicity depends on η and a huge shift, especially for hits consisting of only few pixels (cf. Figure 4.45), is found.

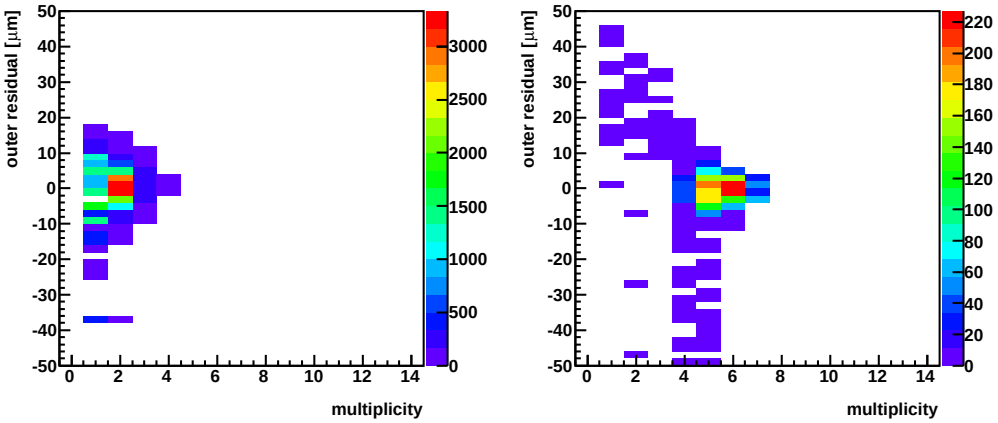

Figure 4.45.: Residuals as a function of the pixel multiplicity (toy MC). **Left:** For $\eta = 0$, no correlation between multiplicity and residual is found, as expected. **Right:** For $\eta = 6$ and low multiplicities, the size of a residual depends on the pixel multiplicity significantly.

Obviously, residuals of hits with a low pixel multiplicity in high η-ranges are biased. The associated hits can be produced, if only a small fraction of the hit is situated inside the sensor (cf. Section 4.6). Both edges in φ and in η need to be considered. Due to the module inclination α, a track typically leaves a diagonal pattern of surface charges. If the particle does not traverse the full depth of the sensor, the remaining fraction will be significantly biased (cf. Figure 4.46).

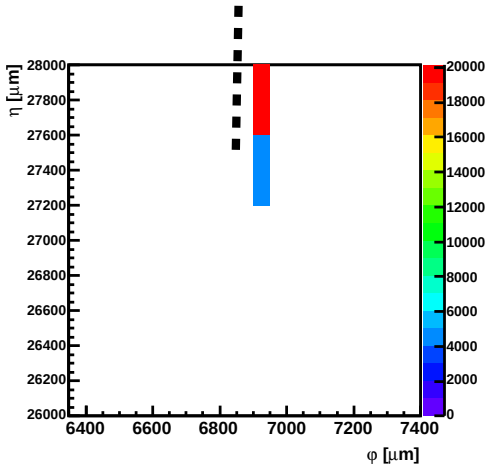

Figure 4.46.: The reconstructed position of this hit is clearly biased, as the *dashed* particle does not traverse the whole depth of the module.

In the following all hits close to an edge are removed. If the reconstructed centre of a surface charge distribution belongs to the outermost three pixels in φ-direction (channels 0-3 and 324-327), the hit is neglected. The cut, applied in η direction, depends on η itself in order to minimise the number of discarded hits: the hits of $1-3$ pixels at the sensor edges are neglected (for central modules only one pixel, for modules at module-$|\eta| = 6$ three pixels are excluded from the analyses, in-between two).

The distribution of overlap residuals over the entire barrel does not change significantly although the statistics reduces by about 20-30 %. The η-dependency of overlap and single residuals vanishes completely - independent from other parameters such as digitisation or magnetic field (cf. Figure 4.47). Also the accumulation of hits with the width of one residual being significantly narrower distributed than the other vanishes completely just as the hits with a low pixel multiplicity at high η values.

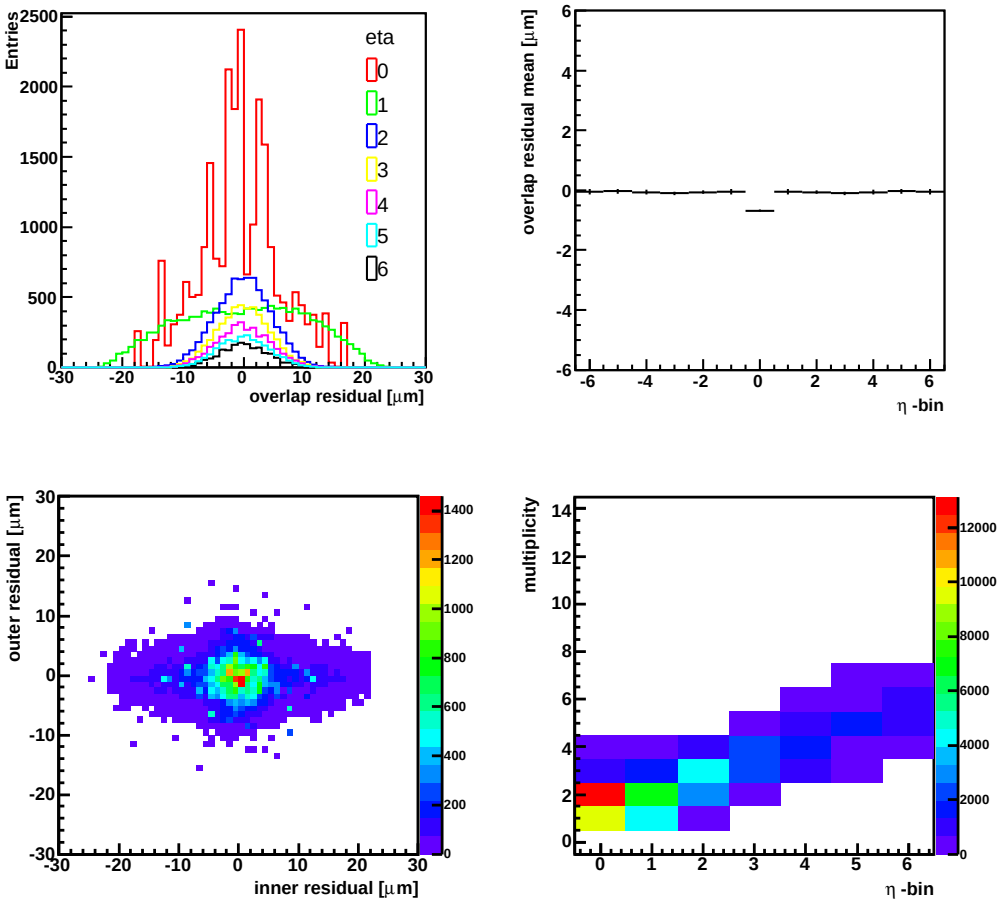

Figure 4.47.: Top left: Barrel-wide overlaps do not change noticeably, yet statistics decreases by 25%. **Top right:** Independent from all other parameters such as magnetic field, diffusion and module inclination, the η-dependency of residuals and overlap residuals vanishes completely. **Bottom left:** The cross-like pattern in the correlation plot between inner and outer residual vanishes. **Bottom right:** The hit-multiplicity depends on module-η clearly, the various hits with a low pixel multiplicity at high η values vanish.

Applying the edge cut, the characteristics of Pixel overlap residuals in the toy Monte Carlo become concordant to theoretical expectations. Thus, the behaviour of edge channels in ATHENA is studied (cf. Figure A.10). Both the overlap residuals as a function of the module coordinates and the channel numbers show a qualitatively very similar behaviour (cf. Section A.3).
Therefore, the extended edge cuts are transferred to ATHENA in a next step. According to Figure A.10, the cuts for the overlap region are chosen as follows:

- Two edge channels in φ direction are excluded from analyses.
- An η-dependent cut is chosen for edge channels in η direction (the higher the module-η, the more channels are neglected. A maximum of three pixels in η is excluded at the barrel edges.)
- Additionally, hits of the inner five pixels of the overlap region are excluded as these show the largest bias (up to 10 μm).

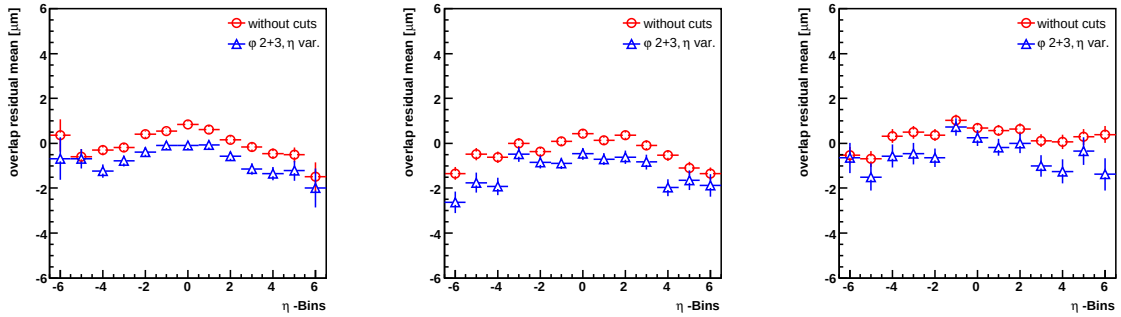

Figure 4.48.: Overlaps versus module-η with edge cuts of $\varphi : 2 + 3\ pixels,\ \eta : 1 - 3\ pixels$ **Left:** Pixel layer 0 **Middle:** Pixel layer 1 **Right:** Pixel layer 2. Although the η-dependence does not vanish completely, its amplitude decreases by 1 μm.

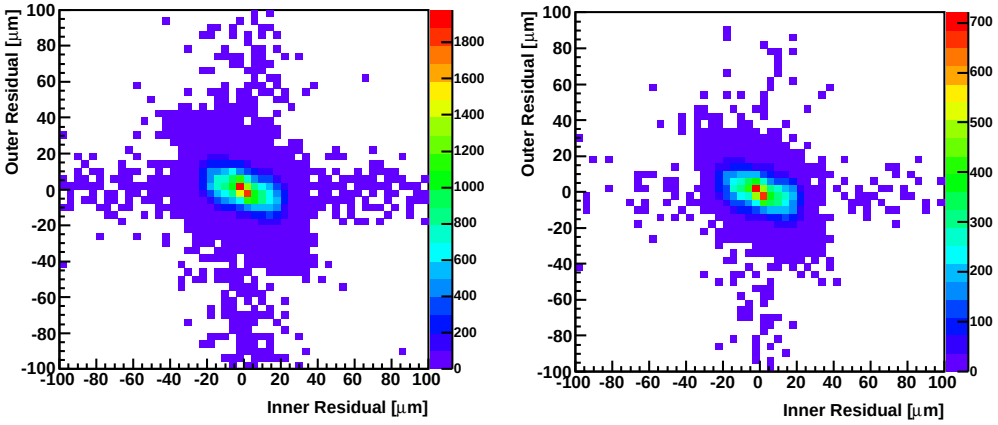

Figure 4.49.: Correlation between the residuals forming an overlap is shown for Pixel layer 2. **Left:** without edge cuts. **Right:** with the adjusted edge cuts. The cross-like pattern decreases visibly, although it does not vanish completely. The correlation factor of -0.3460 does not change significantly compared to the standard sample without edge cuts.

Also in the full detector simulation, the unexpected behaviour of overlap residuals at nominal geometry is mainly dominated by the edge channels of the overlap region. Applying an adjusted edge-cut decreases the η-dependency of overlap residuals visibly by ≈ 1 μm (cf. Figure 4.48) and also the various overlap residuals with the distribution of one residual being narrower than the other (cf. Figure 4.49). But the according correlation coefficient does not change significantly (e.g. from -0.3568 to -0.3560 for pixel layer 2).

Concluding, the application of edge-cuts in φ- and η-direction does change the characteristic behaviour of overlap residuals significantly - both for the toy Monte Carlo and ATHENA. Yet, the applied cuts are not sufficient to suppress e.g. the η-dependence of pixel overlap residuals. Obviously, the transfer of the cuts from the clean environment of the toy Monte Carlo into the complex ATHENA software needs further adjustments.

4.8. Influence of the SCT Read-Out

In the axial part of the SCT detector the mean of the overlap residuals depends on the strip number of the involved modules with multiple maxima per strip (cf. Section 4.6 and Figure 4.23). This effect is reflected in all layers with different intensity: inner layers are affected more heavily than outers.

For more detailed studies, the overlap residuals are analysed as a function of the strip number of the outer module, keeping the strip number of the inner module fixed, and similarly vice versa. In both cases a clear dependence of the overlap residuals on the strip number appears (cf. Figure 4.50). However, for the outermost layers the clear shape vanishes.

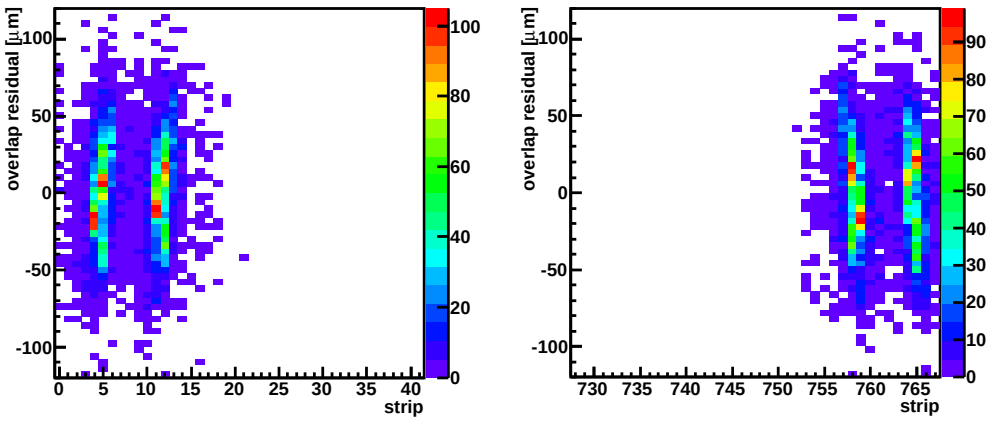

Figure 4.50.: SCT overlap residuals as a function of the channel, exemplarily layer 0: **Left** With strip 758 fixed on the inner module, a clear dependence of overlap residuals on the outer strip number appears. **Right** Channel 12 of the outer module is fixed. Then a very similar structure appears on the inner module.

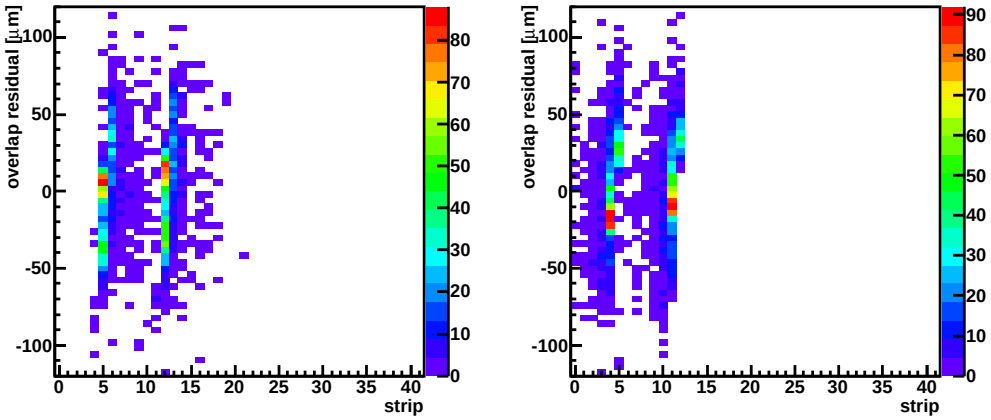

Figure 4.51.: SCT layer 0 at fixed inner strip (758): **Left** Overlap residuals of negatively charged particles as function of the strip number. **Right** Similarly overlap residuals of positively charged particles. The different charge of the particles increases the dependency of overlap residuals on the strip number but does not cause it.

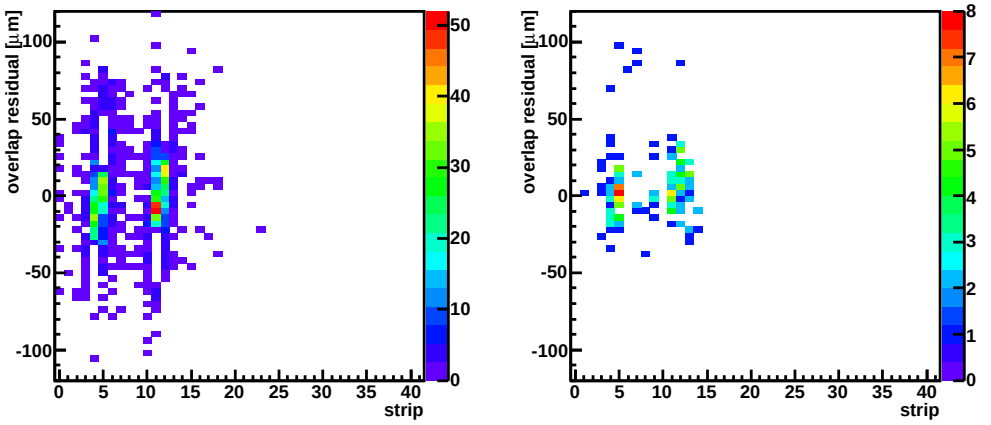

Figure 4.52.: SCT layer 0 at fixed inner channel (758): **Left** Overlap residuals from φ single-strip hits show the dependence clearly. **Right** Besides very low statistics, overlap residuals from double-strip hits indicate the dependence also.

Charge dependence A reason for the dependence of the overlap residuals on the strip number can be the particle charge as the magnetic field bends even high p_{T} tracks in slightly different directions. This assumption is studied with a cut on the reconstructed particle charge. As can be seen in Figure 4.51, the particle charge contributes cumulatively to the dependency of overlap residuals on the strip number but does not cause it.

Cluster Size Another reason for the dependence of the overlap residual on the channel number can be the φ cluster size of the hits. The intrinsic resolution of multi-strip-clusters is better than the resolution of single-strip hits due to effects of charge sharing etc. This assumption is studied with a cut on the φ cluster size of the hits. Only overlap residuals with identical cluster size on both sensors are considered for simplicity. Besides very low statistics, the structure is seen both in the distributions of single-strip hits and double-strip hits in outlines (cf. Figure 4.52). Thus, the cluster size is not the origin of the dependence of overlap residuals on the strip number.

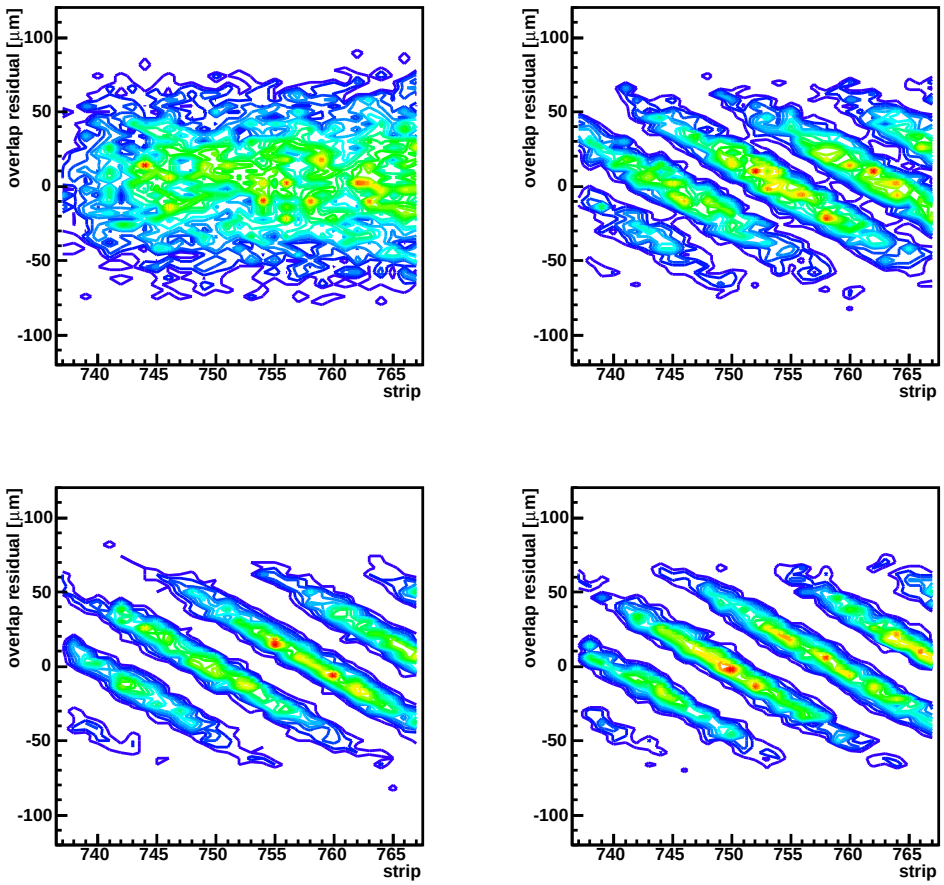

Figure 4.53.: SCT layer 2. The dependency of overlap residuals on the strip number mostly becomes clearer with increasing transverse momentum. From **top left** to **bottom right**: $(2-15)$ GeV, $(35-45)$ GeV, $(65-75)$ GeV and $(95-105)$ GeV.

4.8.1. Dependence on Transverse Momentum

The incident angle between track and module depends directly on particle charge and its transverse momentum. As the charge (i.e. the bending direction of the track) influences the behaviour of overlap residuals (cf. Section 4.8), also the angle itself could influence the dependency of the overlap residual mean on the SCT strip number. The higher p_{T} the straighter and more radial the tracks.

For the outer layers the structure becomes clearer with increasing p_T (cf. Figure 4.53), while in the inner layers the structure appears around 40 GeV and vanishes again at higher p_T-values. The occurrence of this structure especially for high transverse momentum (i.e. straight tracks) and the differences between the layers imply a *projection* effect which must be related to a SCT-specific parameter as none of the Pixel layers shows a similar behaviour.

4.8.2. Binary Read-Out and Projection between Modules

One of the main differences between the Pixel and the SCT detector is not only the different inclination of both detectors but also the read-out procedure. The read-out of the SCT is done completely binary (cf. Section 2.2.3).
For every strip there are only two states: *hit ("1")* or *not hit ("0")*. While a particle deposits its energy continuously along its path through the module, the hit locations are discrete. Single-strip hits are always assigned to the strip centre, while the location of multi-strip hits is a geometrical average.

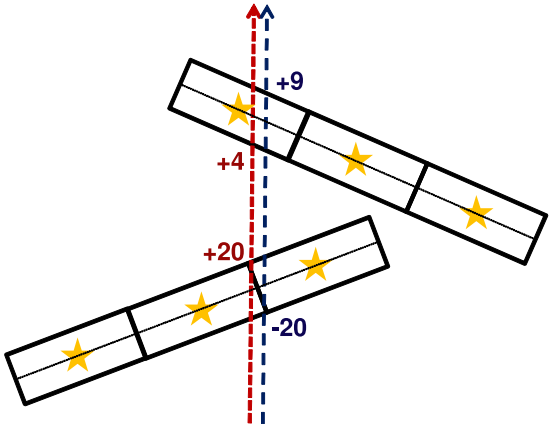

Figure 4.54.: Because of the binary read-out of the SCT, which assigns hits to the geometrical middle of a strip, two nearly identical tracks with a small difference in φ can cause totally different residuals (resulting also in different overlap residuals) when hitting the intersection between neighboured strips on one of the modules.

Two almost identical tracks with only a small difference in φ can create totally different residuals when hitting the intersection between the two strips. Without loss of generality (*w.l.o.g.*) the first track hits the left strip at its right edge, while the second track hits the right strip at its left edge. The coordinate axis for residuals points to the right, resulting in values for the first residual of 20 μm and for the second residual of -20 μm (cf. Figure 4.54).

Due to the track reconstruction allowing continuous hit positions, single residuals still have a Gaussian shape on average over a whole sensor.
Let the hits on the second module be located near the geometrical middle of a strip, so w.l.o.g. the value for the residual of the first track is $+4$ μm and for the second track it is $+9$ μm. The resulting overlap residuals finally add up to -16 μm (first track) and $+29$ μm (second track) - although both tracks are nearly identical. Thus, with an ensemble of tracks flat in φ passing, both residuals jump independently from each other at every intersection between neighbouring

channels. As the detector geometry determines the angle between the modules, the number of intersections is calculable which can be passed by tracks when the strip number of the second module is kept fix.
The impact of the magnetic field on the dependency of overlap residuals on the strip number (cf. Figure 4.27) is caused by the typical cluster width in φ. The smaller the cluster size, the clearer this dependency. For the standard sample (*stdSTD*) only about 24% of the hits in the barrel region hit two neighbouring strips. Without Lorentz-drift and correction (*nfNF*) this number increases up to 45% (cf. Figure 4.55), as the module inclination and the Lorentz angle are adjusted in order to minimise the cluster size of radial tracks.

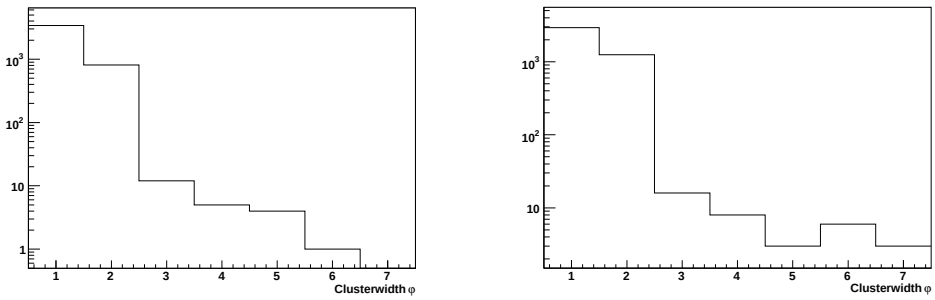

Figure 4.55.: Left: In the normal case, only about 25% of all hits have a φ-clustersize of more than 2. **Right:** Without the impact of a magnetic field inside the silicon sensors this number increases to 45%.

4.8.3. Verification with Toy Monte Carlo

In order to verify this assumption the Toy-MC (cf. Section 4.3.1) needs small adjustment: a binary read-out is implemented for both Silicon trackers.
The following parameters are chosen: an angular uncertainty of 0.03°, a module resolution of 18 μm, a track offset uncertainty of 20 μm, a radial distance between track swivel and vertex of 450,000 μm and an incident angle 90° (only radial tracks).

Although single and overlap residuals keep a Gaussian shape on module average, the binary read-out enforces the appearance of a "baguette"-like structure very similar to the ATHENA observations in both silicon trackers which vanishes if the charge information is used for the position reconstruction (figure 4.56).

Concluding, the binary read-out of the SCT leads to a dependence of the overlap residual mean on the strip number of the participating modules. This effect is most prominent for high p_{T} tracks as the intersection between neighbouring strips of one module is straight-forwardly projected onto the second module. It is washed out for low-p_{T} tracks.

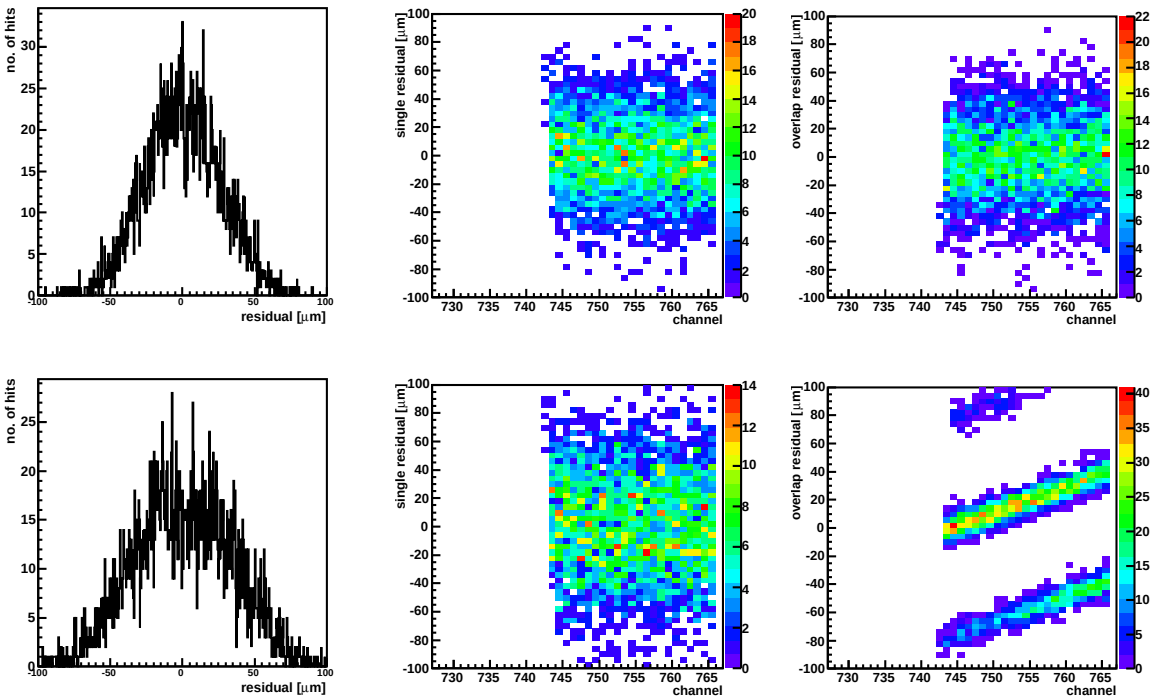

Figure 4.56.: Differences between analogue (upper row) and digital/binary (lower row) read-out of the SCT detector in toy MC. **Left column:** Single residual of the inner module on layer 3. The typical Gaussian shape is shown which is independent from the way of read-out. **Middle row:** Single residual as function of strip number. In both cases, no specific characteristic is found. **Right row:** Overlap residuals as function of inner strip no. The binary read-out creates a "baguette"-like shape, while in complete analogue case, the behaviour of the overlap residuals equals the single residuals.

5. Global Detector Deformations

Overlap residuals are expected to be sensitive to global detector deformations. A simple implementation of the distortions displayed in the misalignment matrix (cf. Table 3.1) is chosen and verified. Afterwards the impact on the overlap residuals is studied.

5.1. Parametrisation of the Deformations

In the alignment procedure, three levels of misalignment are distinguished:

- *Level-1* describes deformations/displacements of the whole detector.
- *Level-2* refers to layer-/ disc-wide displacements.
- *Level-3* is module-based.

It is possible to generate global detector deformations with level-1 or level-2 displacements. However, level-3 displacements allow for a more precise adjustment of each single module forming a global deformation. Therefore, level-3 displacements are chosen in the following and the global deformations are translated to module-level. Due to the geometrical arrangement of the modules with their inclination angle α between a barrel tangent and the module plane (cf. Section 2.2.3), e.g. a radial displacement corresponds on level-3 to a Local$X$-Local$Z$ transformation.

$$\vec{e}_R \rightsquigarrow \vec{e}_X + \vec{e}_Z$$

The toolkit for the misalignment production is the Local-χ^2-algorithm, which allows to generate a modified geometry database according to the misalignment needs. Misalignments can be integrated into the detector simulation in two different ways: If the displacements are very large (i.e. the new module position does not agree with the original position at all), then the complete reconstruction including pattern recognition and tracking must be rerun with the new geometry. But if the displacements are small (i.e. the new module position is very similar to its original one), then the track is assumed to be unchanged and only the track-fitter must be rerun for an update of the residual calculation.

Let S be the maximum displacement applicable to a module. The CSC-00-00-00 geometry is chosen in combination with a different amplitude of the deformations: A maximum displacement S of $S = 500$ μm is applied in the (*S500*) data sample and $S = 100$ μm (*S100*) respectively. Only barrel displacements are considered.

Let r be the radius of the barrel layer, l its length, r_M the maximum radius of the detector (SCT layer 3), l_M its maximum length (SCT layer 3), φ and η be module's coordinates with φ_M

being the number of modules per η-ring. The maximum displacement S needs to be converted into radial, axial and z displacements first. $\Delta X_M,\ X \in \{R, \varphi, Z\}$

$$\begin{aligned} \Delta R_M &= S \\ \Delta\varphi_M &= 2 \cdot \sin\left(\frac{S}{2 \cdot r_M}\right) \\ \Delta Z &= S \end{aligned}$$

The deformations can be parameterised as shown in Table 5.1. For the SCT-detector, $\eta/6.$ must be replaced with $(\eta - 1/2.sign(\eta))/6.$ as a module with $\eta = 0$ does not exist.

	ΔR	$\Delta\varphi$	ΔZ
R	$\frac{r}{r_M} \cdot \Delta R_M$	$\frac{r}{r_M} \cdot \Delta\varphi_M$ $\left(\frac{r}{r_M}\right)^2 \cdot \Delta\varphi_M$	$\frac{r}{r_M} \cdot \Delta Z_M$
φ	$\left\lvert\sin\left(2\pi\frac{\varphi_{module}}{\varphi_M+1}\right)\right\rvert \cdot \Delta R_M$ $\frac{r}{r_M} \cdot \sin\left(2\pi\frac{\varphi_{module}}{\varphi_M}\right) \cdot \Delta R_M$	$\left\lvert\sin\left(2\pi\frac{\varphi_{module}}{\varphi_M+1}\right)\right\rvert \cdot \Delta\varphi_M$ $\frac{r}{r_M} \cdot \sin\left(2\pi\frac{\varphi_{module}}{\varphi_M}\right) \cdot \Delta\varphi_M$	$\sin\left(2\pi\frac{\varphi_{module}}{\varphi_M+1}\right) \cdot \Delta Z_M$ $\sin\left(2\pi\frac{\varphi_{module}}{\varphi_M}\right) \cdot \Delta Z_M$
Z	$\eta/6. \cdot \frac{l}{l_M} \cdot \Delta R_M$	$\eta/6. \cdot \frac{l}{l_M} \cdot \Delta\varphi_M$	$\eta/6. \cdot \frac{l}{l_M} \cdot \Delta Z_M$

Table 5.1.: Exemplary parameterisation of the misalignment matrix. Entries of the upper lines refer to *S500*, lower line describes *S100*, if different.

Finally, $\Delta X_M,\ X \in \{R, \varphi, Z\}$ is transferred into the different local coordinate frames of the Pixel and the SCT detector (incident angle $\alpha \in \{+20°, -10°\}$). β represents a rotation around LocalY. The conversion from the global to the module-local coordinate frame is then given by the Equations 5.1.

$$\begin{aligned} \Delta R \begin{cases} \text{LocalX} &= \sin(\alpha) \cdot \Delta R \\ \text{LocalZ} &= \cos(\alpha) \cdot \Delta R \end{cases} \\ \Delta\varphi \begin{cases} \text{LocalX} &= 2r \cdot \sin\left(\frac{\Delta\varphi}{2.}\right) \cdot \cos\left(\frac{\Delta\varphi}{2} + \alpha\right) \\ \text{LocalZ} &= -2r \cdot \sin\left(\frac{\Delta\varphi}{2.}\right) \cdot \sin\left(\frac{\Delta\varphi}{2} + \alpha\right) \\ \beta &= \Delta\varphi \end{cases} \\ \Delta Z \begin{cases} \text{LocalY} &= \Delta Z \end{cases} \end{aligned} \tag{5.1}$$

5.2. Verification

The validation of the generated misalignment sets is done graphically via a 3D visualisation tool [72]. It is based on ROOT and Open-GL, and converts alignment constants from e.g. the Local-χ^2-algorithm (with the help of *InDetRecExample* and *SiGlobalChi2Algs*) into a three-dimensional model of the silicon barrel tracker. For comparison, the nominal geometry is added in green, while the actual layout is shown in red.

For the *S500* simulation, all nine misalignments are shown in Figure 5.1. All deformations qualitatively show the expected behaviour.

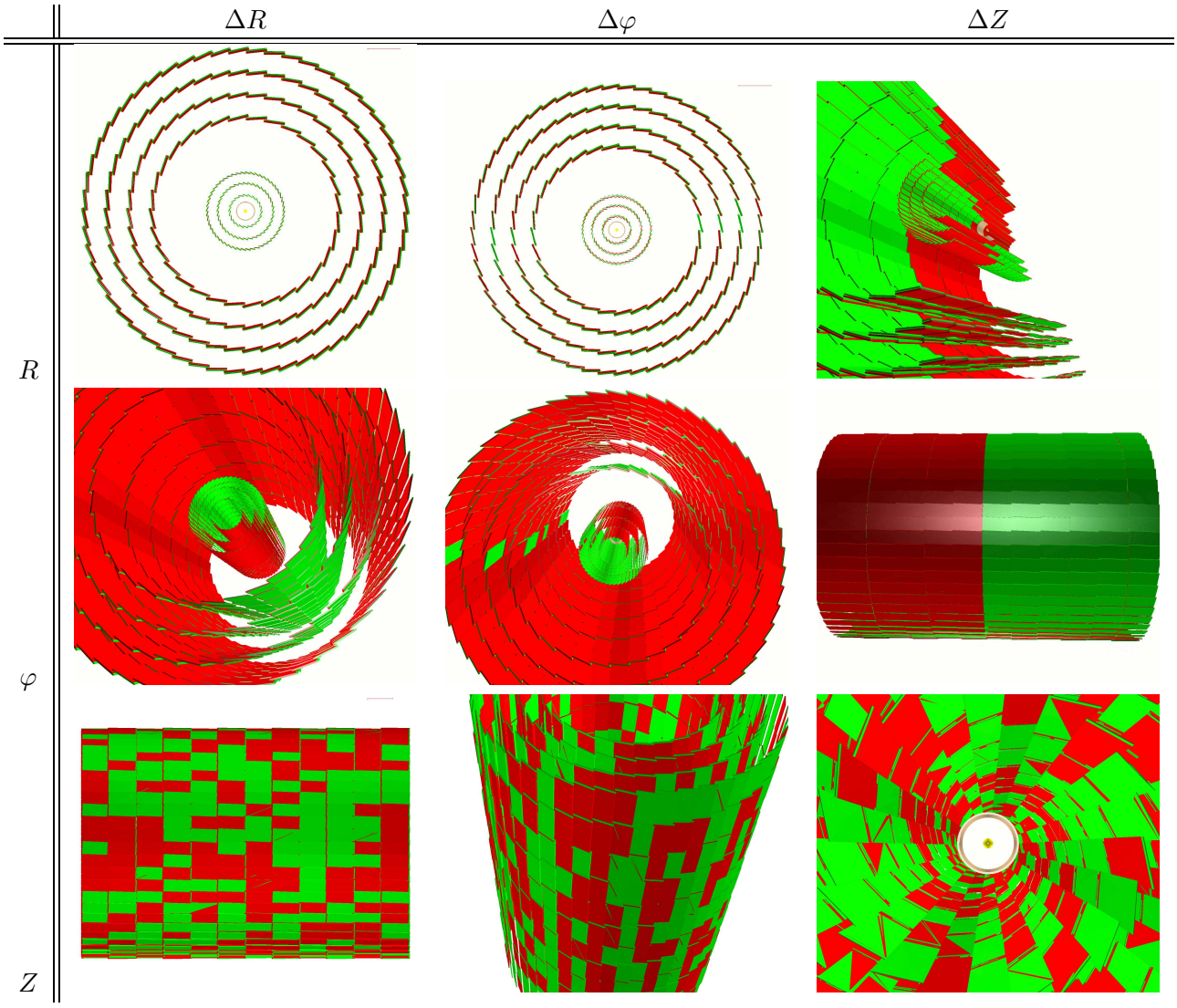

Figure 5.1.: Visualisation of the misalignment matrix with a maximum shift of $S = 500$ μm. All deformations show the expected behaviour.

In the *S500* sample the non-radius-dependent deformations lead to disproportionally large shifts - e.g. in Pixel layer 0, $r \approx 50000$ μm, a module-shift of 500 μm is applied, which corresponds to a severe change of the detector layout. Thus, only the results of S100 are used for further studies.

5.3. Impact on Overlap Residuals

Typical indicators for the impact of the misalignment matrix (maximum shift of 100 μm) on overlap residuals are either the overlap residual distributions of an entire layer or the distributions split up by φ or η (*rings or staves*), or a combination of both.
For example, the elliptical (i.e. sinusoidal) shape of $\varphi\Delta R$ is perfectly reflected by overlap residuals as function of module-φ (cf. Figure 5.2) just as the radial expansion $R\Delta R$ shifts mean of the barrel-wide overlap residual distribution about 16 μm.

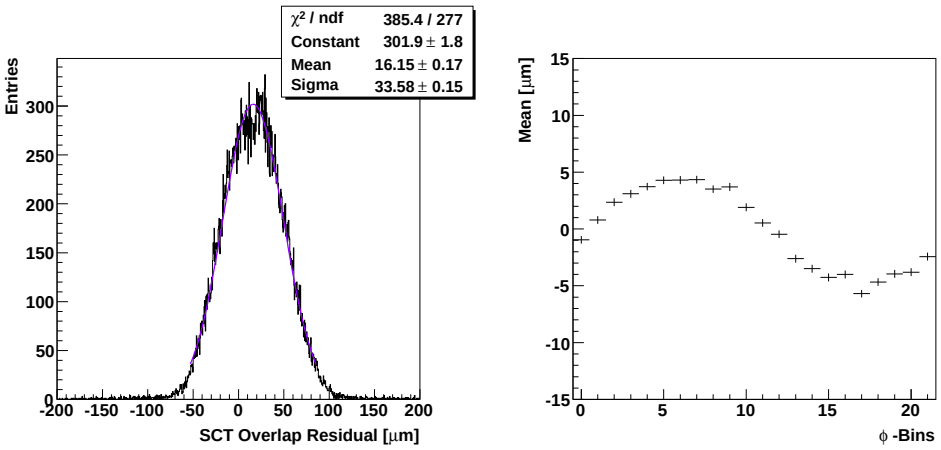

Figure 5.2.: Left: (SCT layer 1) $R\Delta R$ expands the barrel radially about 58 μm and is reflected in a shift of the overlap residual mean of about 16 μm. Shrinking creates an opposite-directed shift. **Right:** (Pixel layer 0) $\varphi\Delta R$ shapes the R-φ-cross-section through the detector elliptical. The sinusoidal shifts of overlaps as function of module-φ corresponds to its mathematical parametrisation.

Exemplarily, the impact of the radius-dependent deformations of SCT layer 0 is shown in Figure 5.3. The impact of angular and z-dependent deformations on SCT layer 0 can be found in the Appendix (cf. Figures A.11 and A.12).

The deformations of the first column are reflected qualitatively by the overlap residual distributions. Table 5.2 summarises the impact of the deformations on R-φ overlap residuals. The amplitudes of the reflected patterns range from one hundred to only a few microns, depending on how strongly the deformation influences especially the module-to-module distance.

The present limitation of this method is given by the systematic effects of overlap residuals at nominal geometry. The maximum radial expansion of the ellipse is simulated about 10 μm for Pixel layer 0 (cf. Figure 5.2), which already corresponds to the amplitude of the η-dependent structure of Pixel overlap residuals.
R-$\Delta\varphi$ and Z-$\Delta\varphi$ result in an indefinable pattern of overlaps versus module-η, though a clear deformation is visible. However, φ-$\Delta\varphi$ shows its sinusoidal shape of overlaps versus module-φ again clearly.
As expected, the deformations of the third column are invisible for R-φ overlap residuals.

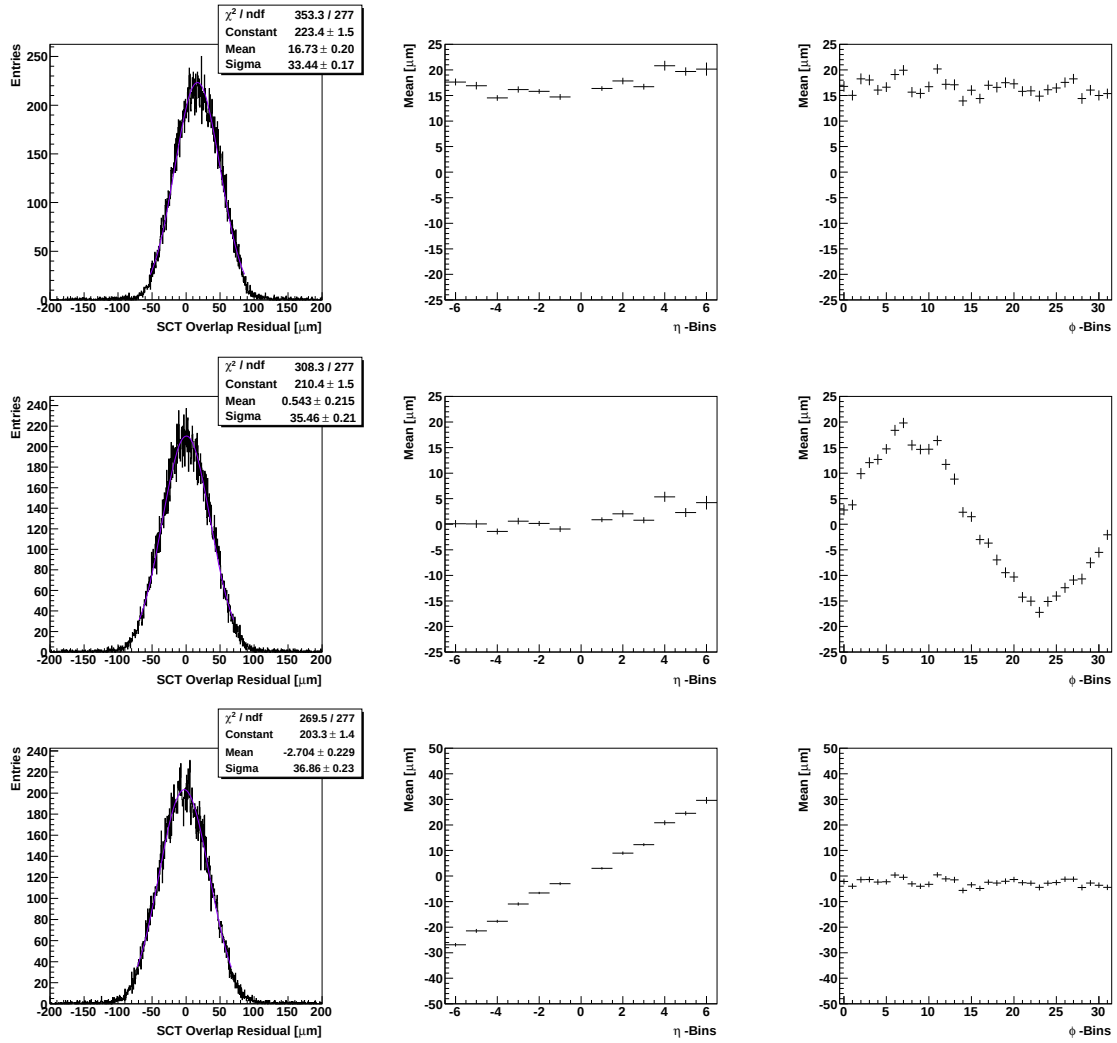

Figure 5.3.: Impact of the radius dependent global deformations on SCT layer 0 exemplarily. **Top:** R-ΔR **Middle:** φ-ΔR. **Bottom:** Z-ΔR. **Left:** Overlap residuals of an entire barrel. **Middle:** Overlap residual versus module-η. **Right:** Overlap residuals versus module-φ. - All deformations are reflected by overlap residuals qualitatively.

The sensitivity of overlap residuals must be compared especially to that of single residuals (cf. Figure 5.4). While for SCT layer 3, the overlap residuals reflect the 100 μm displacement of the modules (radial expansion) with a shift of their mean about 20 μm, the typical distributions of the single residuals stay unaffected. A similar characteristics is found for the elliptical shape. While even the overlap residuals of Pixel layer 0 reflect a maximum displacement of 10 μm with a shift of at least the same order of magnitude, the single residuals do not change noticeably at all.

Concluding, R-φ overlap residuals are sensitive to global deformations which impact the module-to-module geometry as expected. Especially in comparison with the according single residuals, an improved sensitivity is found. At the present, the sensitivity of overlap residuals for alignment purposes is still limited to a few micron due to systematic effects.

Deformation	complete barrel	Rings (ov. versus η)	Staves (ov. versus φ)
$R\Delta R$	mean shifted	flat[1] but shifted	flat but shifted
$\varphi\Delta R$	centered [1]	flat and centered	sinusoidal shaped
$Z\Delta R$	centered	diagonal	flat and centered
$R\Delta\varphi$	centered	partly deformed	flat and centered
$\varphi\Delta\varphi$	centered	flat and centered	sinusoidal shaped
$Z\Delta\varphi$	centered	deformed	flat
$R\Delta Z$	centered	flat and centered	flat and centered
$\varphi\Delta Z$	centered	flat and centered	flat and centered
$Z\Delta Z$	centered	flat and centered	flat and centered

Table 5.2.: Impact of the misalignment matrix on typical overlap residual distributions. Qualitatively, the deformations of the first two columns are reflected by overlap residuals, while the exact quantitative results are layer-dependent (especially the angle between the modules influences the amplitude of shifts).

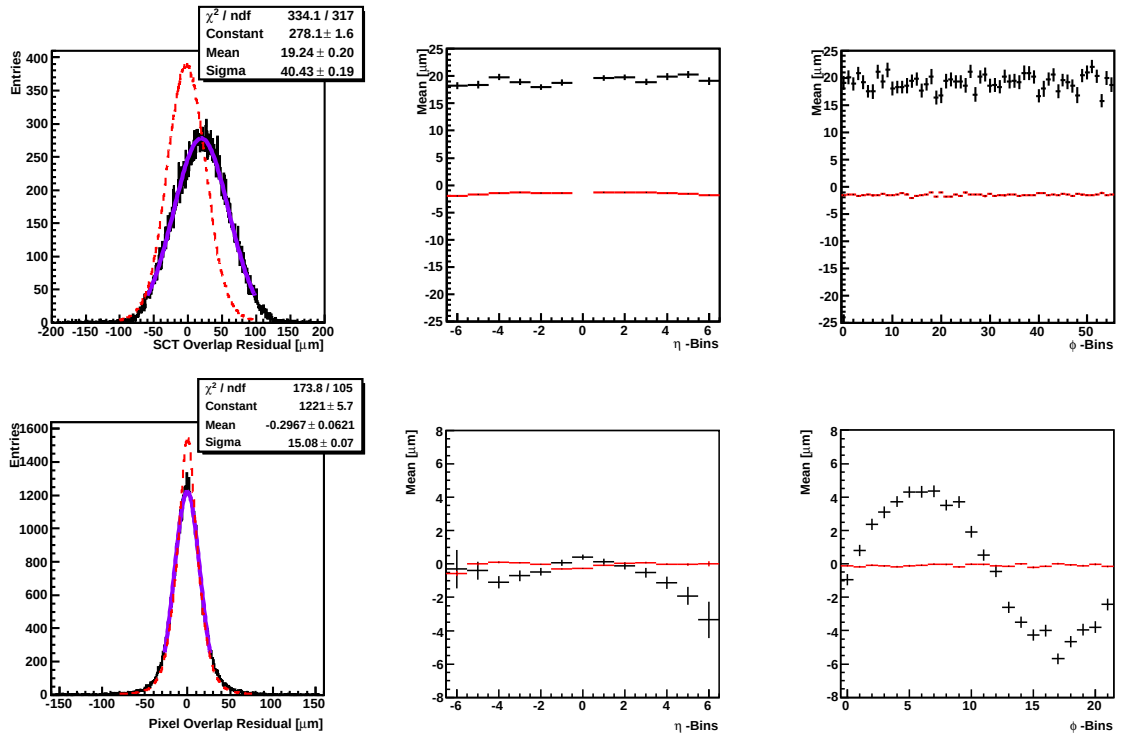

Figure 5.4.: Top: Impact of R-ΔR on SCT layer 3 (maximum shift applied 100 μm). **Bottom:** Impact of φ-ΔR on Pixel layer 0 (maximum shift applied 10 μm). - Comparison between single residuals *(red)* and overlap residuals *(black)*. The barrel-wide single residual distributions are normalised to the number of overlap residuals.

[1] With respect to nominal geometry (biases in overlap means, η-dependency of pixel overlap residuals etc.)

6. Conclusions and Outlook

6.1. Conclusion

As has already been shown in former experiments [51, 62], overlap residuals can be a powerful tool for alignment studies. Thus, a method for the identification of global detector deformations of the ATLAS Silicon Trackers using overlap residuals has been developed. Systematic studies of overlap residuals at nominal geometry were performed at first:

- The mean of the overlap residual distributions of an entire barrel deviates from zero by a few micron - the amplitude of the shifts depends on the detector type and the layer.
- Overlap residuals show a clear η-dependency in the pixel detector ($O(3\ \mu\text{m})$).
- Inner and outer residuals are correlated and hits are found with the distribution of one of the participating single residuals being significantly narrower than the other (cross-like pattern in the correlation plots).
- The mean of the overlap residual distribution depends on the strip number for the R-φ wafer of the SCT modules.

The η-dependency of pixel overlap residuals emerges during the hit reconstruction. The reconstructed hit position is clearly biased in case a particle hits a module close to the edge since the sensor is not crossed through its entire depth. Modules at higher η values are affected in particular, as the particles enter these sensors under shallow incidence and the resulting hits normally stretch over 3-5 pixels in η.
Removing hits from the analysis which are close to the modules edges both in φ and η can improve the overlap residuals although it diminishes statistics significantly: The η-dependency of the Pixel overlap residuals decreases as well as the cross-like pattern in the correlation plots between inner and outer residual. Yet the effects are not suppressed completely.

Furthermore, the mean of the overlap residual distributions depends strongly on the strip number of axial side of the SCT sensor. This effect emerges most clearly at high p_{T} tracks and is washed out for low p_{T} tracks and the stereo side of the modules. It is the result of a direct projection of the strip intersections between the respective sensors and the binary read-out of those.

These systematic effects limit the intrinsic resolution of overlap residuals, as the uncertainties of a few micron in the overlap residual distributions can be translated back into a module-to-module precision of a similar order of magnitude. Yet the approximated precision of overlap residuals is sufficient for first alignment studies.

Several global detector deformations have been analysed, which are difficult to detect with single residuals. The used R-φ overlap residuals reflect the majority of the global deformations qualitatively and show an excellent sensitivity to these deformations which influence the module distance in R-φ direction.

Overlap residuals have been proven to be a powerful tool for the alignment of the ATLAS Silicon trackers. Once they are understood quantitatively in full MC, overlap residuals should be integrated in the ATLAS Silicon tracker alignment thus.

6.2. Outlook

The reasons for the unexpected behaviour of overlap residuals at nominal geometry have been explored from various points of view. In order to use overlap residuals for the calibration of the ATLAS detector, the observed effects and dependencies must be verified with real data and combined to a re-calibration of overlap residuals as a significant improvement of their intrinsic resolution is possible.
Afterwards, the alignment studies need to be continued systematically: the misalignments need to be quantified and a set of more realistic implementations of the deformations should be developed. The next goal would be at least a layer-dependent formula for translating overlap residual shifts back into single module displacements.

Finally, the overlap studies could be expanded to z-overlap residuals analogously and - with enough statistics - even diagonal ones could be taken into account. Possibly, the use of different alignment data sets such as cosmic muons and muons from beam halo could lead to further improvements, as important parameters of the tracks (such as the transverse momentum and the incident angle) change significantly within these different samples.
Moreover, overlap residuals are not limited to barrel distortions. Similar analyses could be done for the end caps as well.

Overlap residuals should be included into the ATLAS alignment by default and extensive comparative studies should be done with respect to potentially weak modes of the different alignment methods and the possibility of overlap residuals to detect them.

A. Additional Plots of Overlap Residuals

A.1. Additional Plots of Nominal Geometry

For reasons of completeness, for nominal geometry all overlap residual distributions are shown in the following.

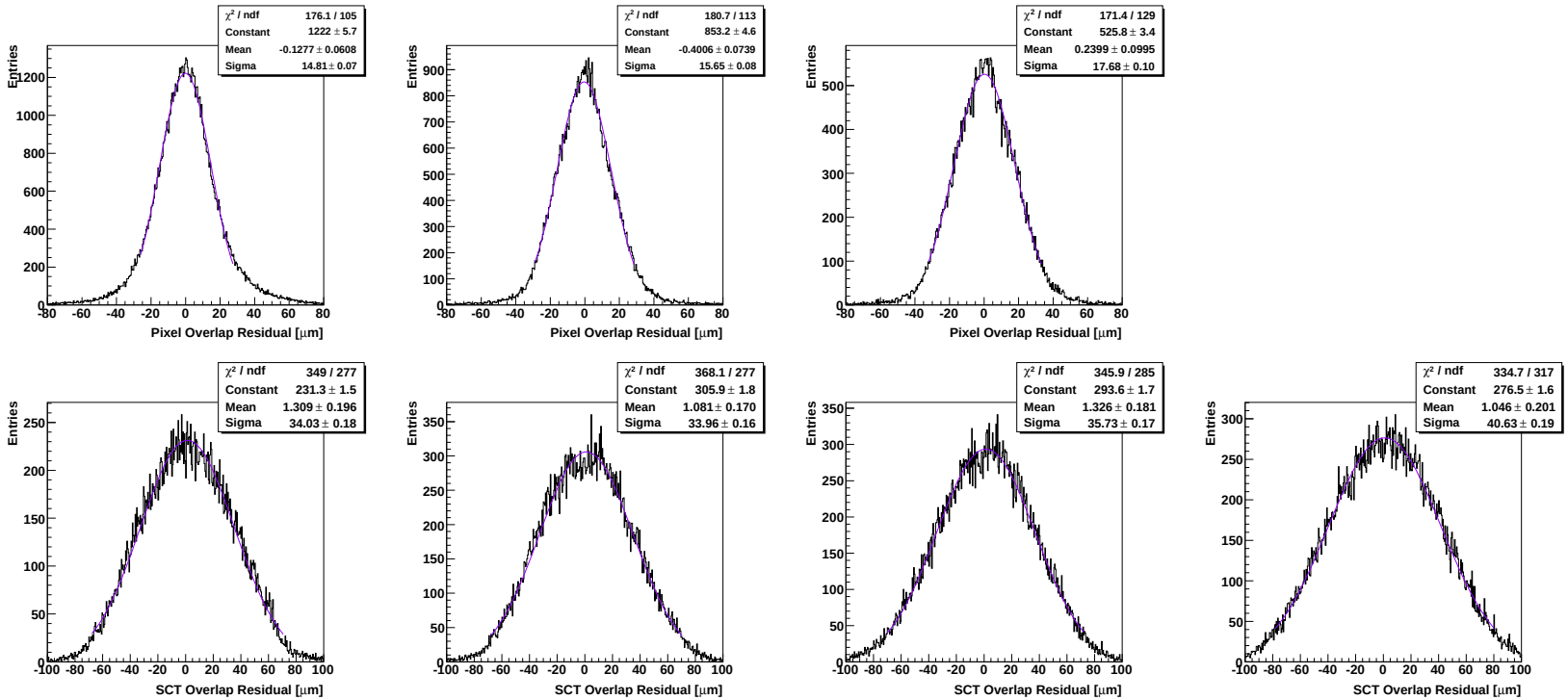

Figure A.1.: Barrel overlap residuals, both for Pixel **(top)** and SCT **(bottom)**. The layer numbers increase from the left to the right. The overlap mean differs layer by layer and deviates from zero. The expected Gaussian shape is distorted by asymmetric shoulders and an accumulation in the maximum region.

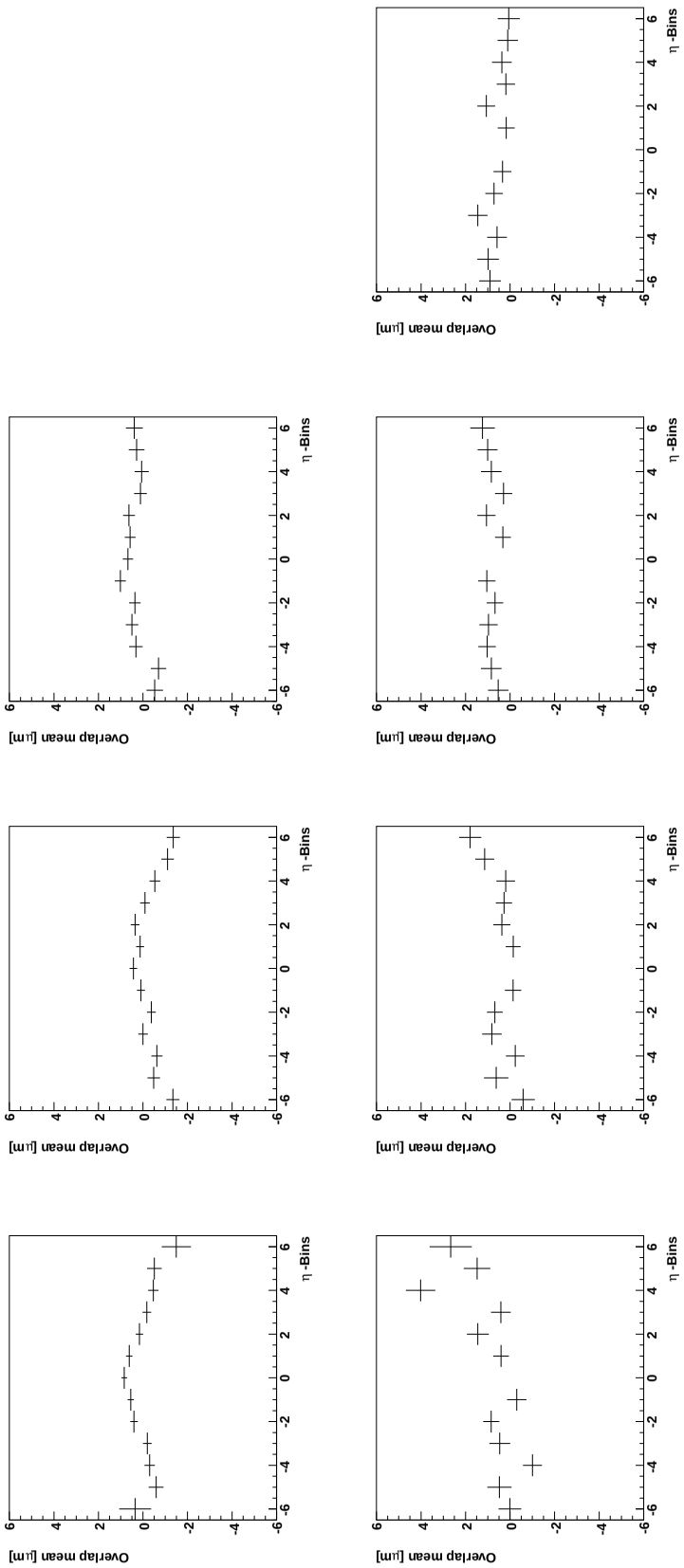

Figure A.2.: Distribution of overlaps residuals versus module-η (*rings*), both for the Pixel **(top)** and the SCT **(bottom)**. The layer numbers increase from the left to the right: While the overlap residual distributions of the SCT are flat and shifted, the Pixel overlap residuals show a η-dependency which decreases going outwards.

Figure A.3.: Distribution of overlap residuals versus module-φ (*staves*), both for the Pixel **(top)** and the SCT **(bottom)**. The layer numbers increase from the left to the right: Pixel and SCT overlap residuals are flat, but they reflect the shifts already seen in the distributions of the entire barrel.

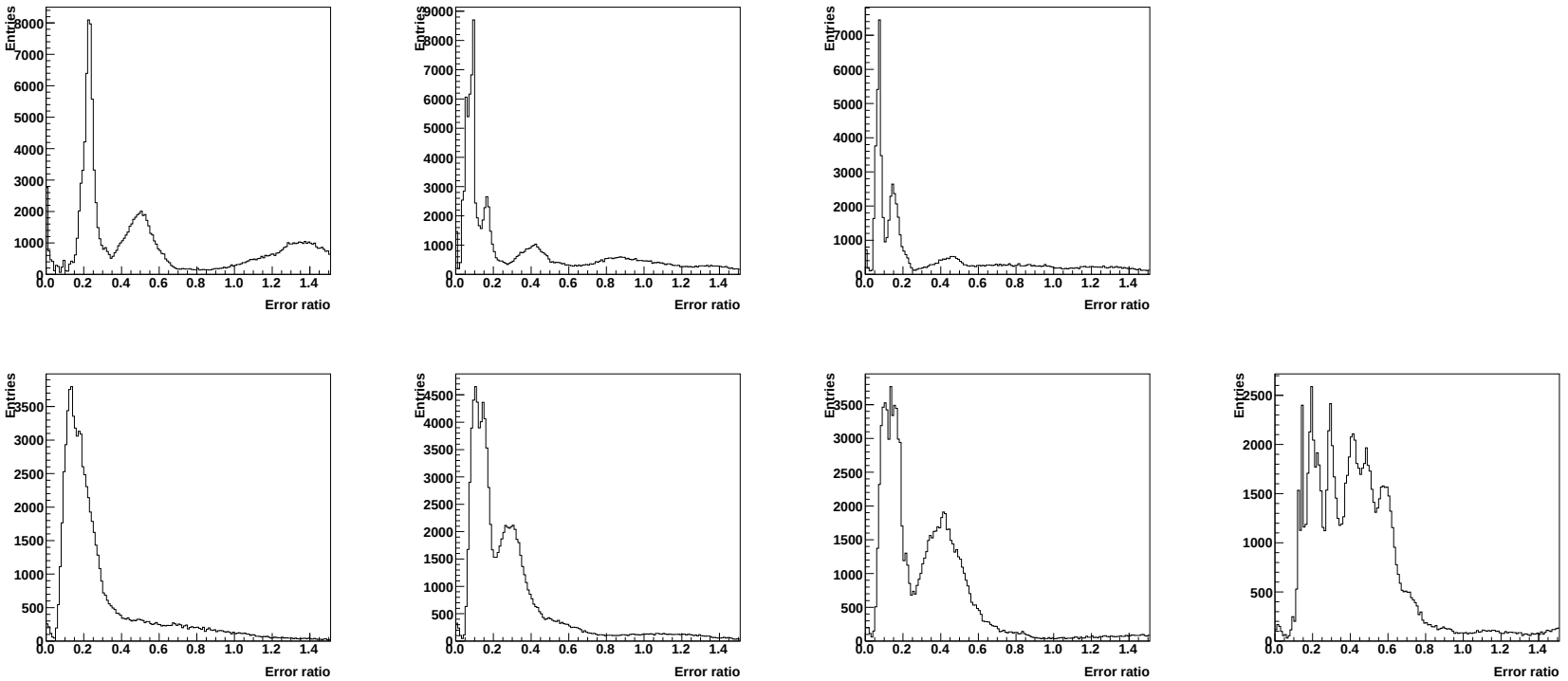

Figure A.4.: Error-ratio $(\sigma_{track}/\sigma_{hit})^2$, both for Pixel **(top)** and SCT **(bottom)**. The layer numbers increase from the left to the right. Only if the error ratio is sufficiently small (i.e. $(\sigma_{track}/\sigma_{hit})^2 \ll 1$), the hits of the different modules are uncorrelated.

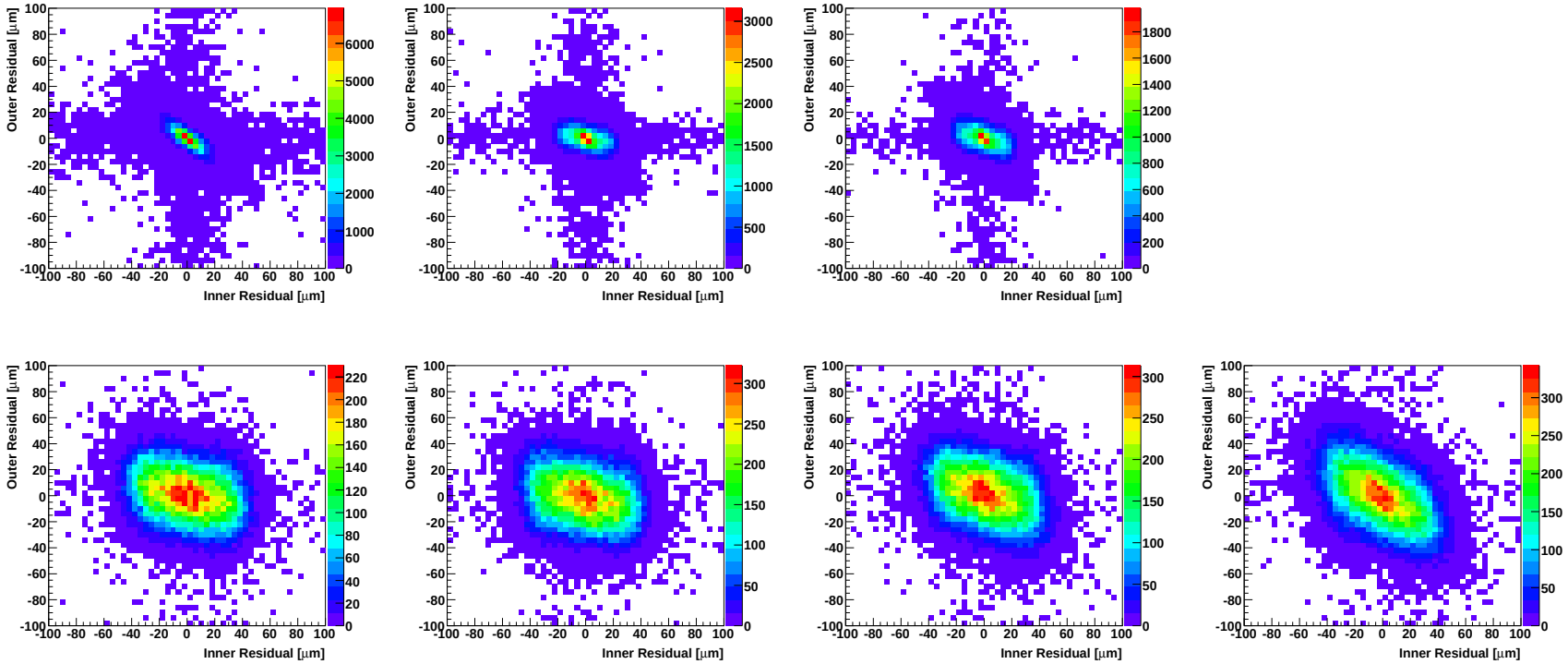

Figure A.5.: Correlation between inner and outer residual, both for Pixel **(top)** and SCT **(bottom)**. The layer numbers increase from the left to the right. Anti-Correlation between the partners is highly visible especially in the innermost Pixel and outermost SCT layer. In-between it is weaker in agreement with the error-ratio.

A.2. Detailed View of the Magnetic Field Errors

The chosen modules are represented by:

$$\vec{g}_0\,[\text{cm}] = \begin{pmatrix} 4.9989 \\ 0.7187 \\ 37.0308 \end{pmatrix} \quad \vec{\varphi}_0 = \begin{pmatrix} 0.2048 \\ 0.9788 \\ 0.0000 \end{pmatrix} \quad \vec{\eta}_0 = \begin{pmatrix} -0.0188 \\ 0.0039 \\ 0.9998 \end{pmatrix} \quad \vec{n}_0 = \vec{\varphi}_0 \times \vec{\eta}_0 \tag{A.1}$$

$$\vec{g}_1\,[\text{cm}] = \begin{pmatrix} 4.5936 \\ 2.0976 \\ 37.0308 \end{pmatrix} \quad \vec{\varphi}_1 = \begin{pmatrix} -0.0792 \\ 0.9969 \\ 0.0000 \end{pmatrix} \quad \vec{\eta}_1 = \begin{pmatrix} -0.0191 \\ -0.0015 \\ 0.9998 \end{pmatrix} \quad \vec{n}_1 = \vec{\varphi}_1 \times \vec{\eta}_1$$

The magnetic field at the module centres is given by:

$$\vec{m}_0\,[\text{T}] = \begin{pmatrix} 0.001703 \\ 0.000886 \\ 2.073643 \end{pmatrix}, \quad \vec{m}_1\,[\text{T}] = \begin{pmatrix} 0.001811 \\ 0.000459 \\ 2.073643 \end{pmatrix} \tag{A.2}$$

The intersections are located at $\lambda_0 = 39.9681379$ cm $\wedge\ \lambda_1 = 36.65093899$ cm, which corresponds in global coordinates to

$$\vec{i}_0\,[\text{cm}] = \begin{pmatrix} 5.093539 \\ 1.414872 \\ 39.616818 \end{pmatrix}, \quad \vec{i}_1\,[\text{cm}] = \begin{pmatrix} 4.670796 \\ 1.297443 \\ 36.328777 \end{pmatrix} \tag{A.3}$$

The magnetic field at the true intersection points is given by:

$$\vec{m}_0\,[\text{T}] = \begin{pmatrix} 0.001924 \\ 0.000695 \\ 2.072122 \end{pmatrix}, \quad \vec{m}_1\,[\text{T}] = \begin{pmatrix} 0.001692 \\ 0.000635 \\ 2.074047 \end{pmatrix}. \tag{A.4}$$

A.3. Detailed Comparison between Toy Digitisation and ATHENA

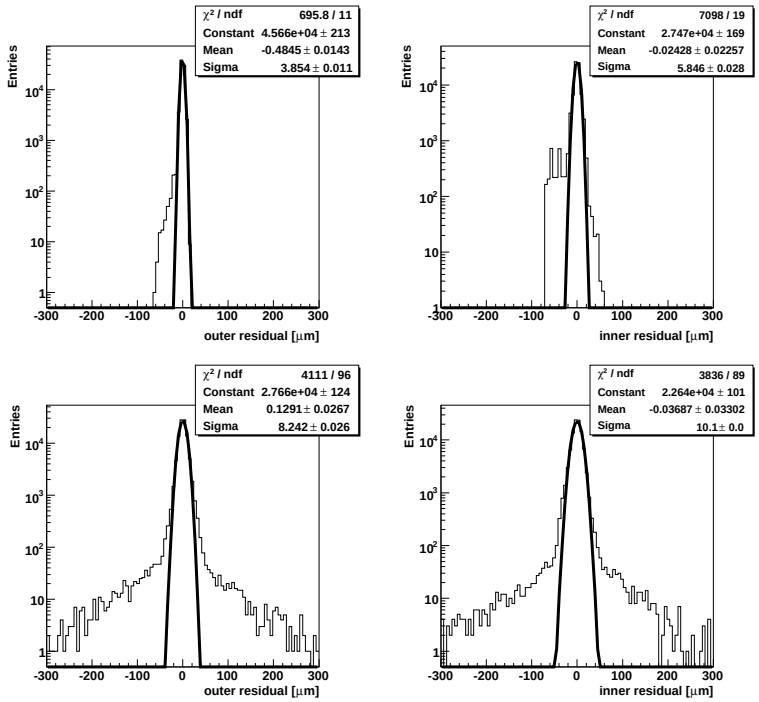

Figure A.6.: Comparison of single residuals for the toy MC of digitisation **(top)** and ATHENA **(bottom)**. All plots agree very well.

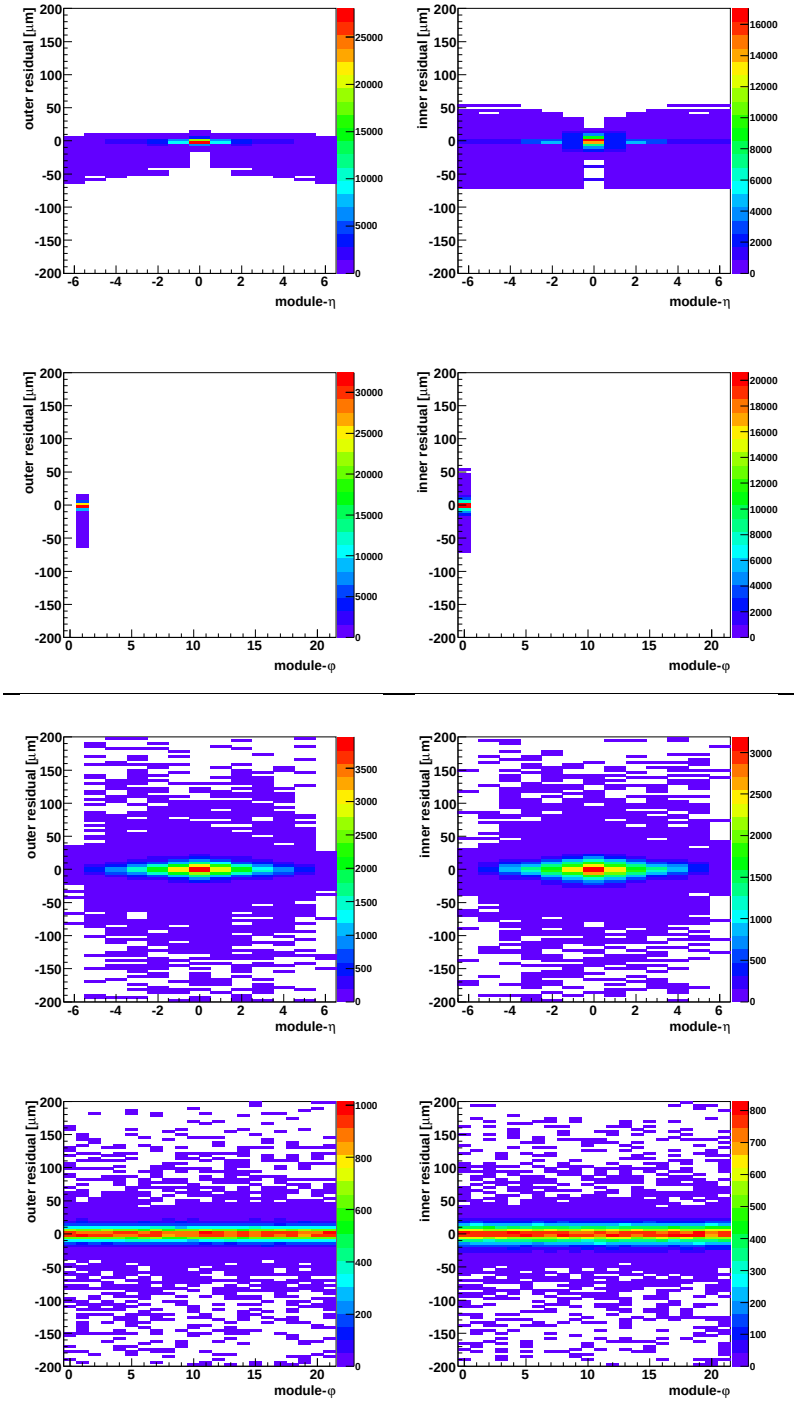

Figure A.7.: Comparison of residuals versus module coordinate for the toy MC of digitisation **(top)** and ATHENA **(bottom)**.

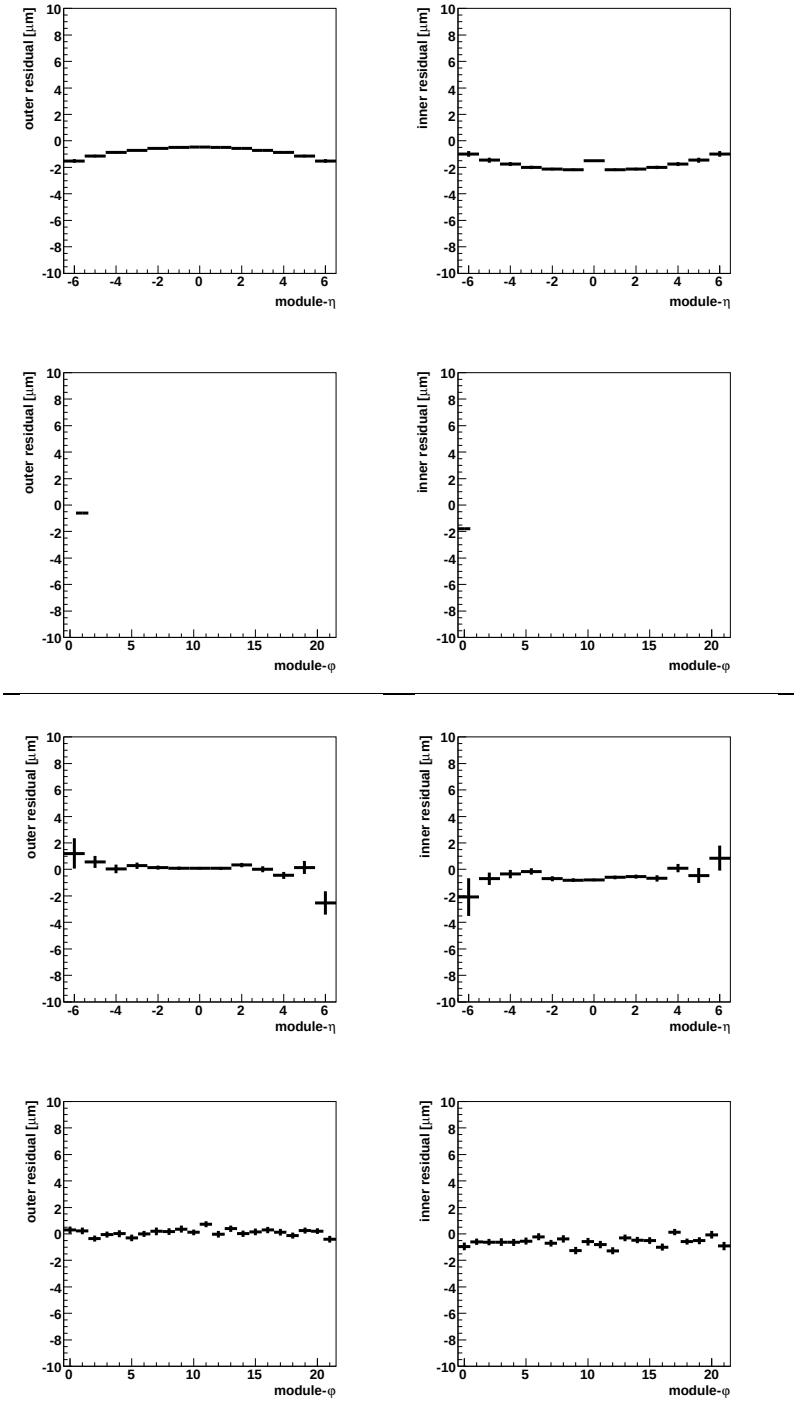

Figure A.8.: Comparison of residuals versus module coordinate plotted as profile histrograms for the toy MC of digitisation **(top)** and ATHENA **(bottom)**.

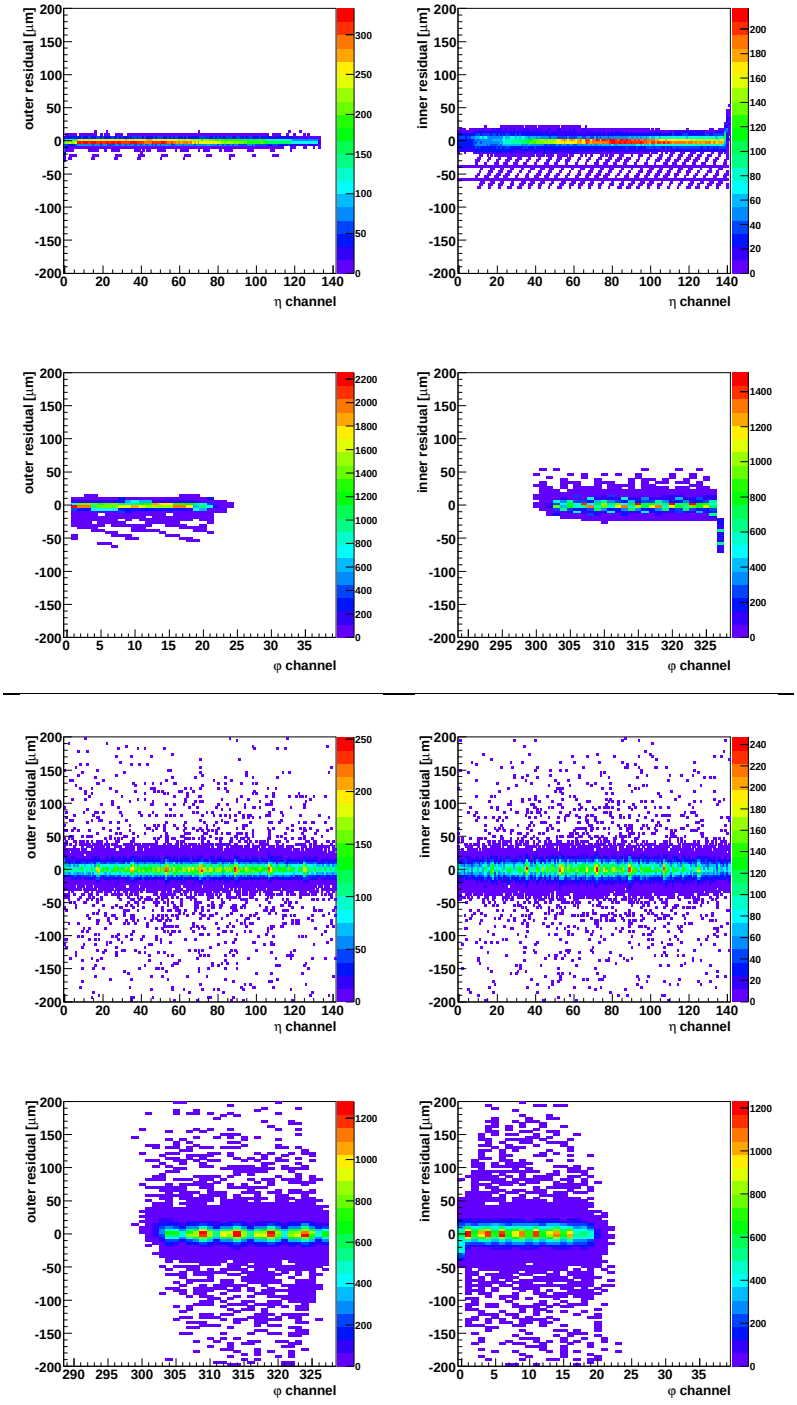

Figure A.9.: Comparison of residuals versus channel number for the toy MC of digitisation **(top)** and ATHENA **(bottom)**.

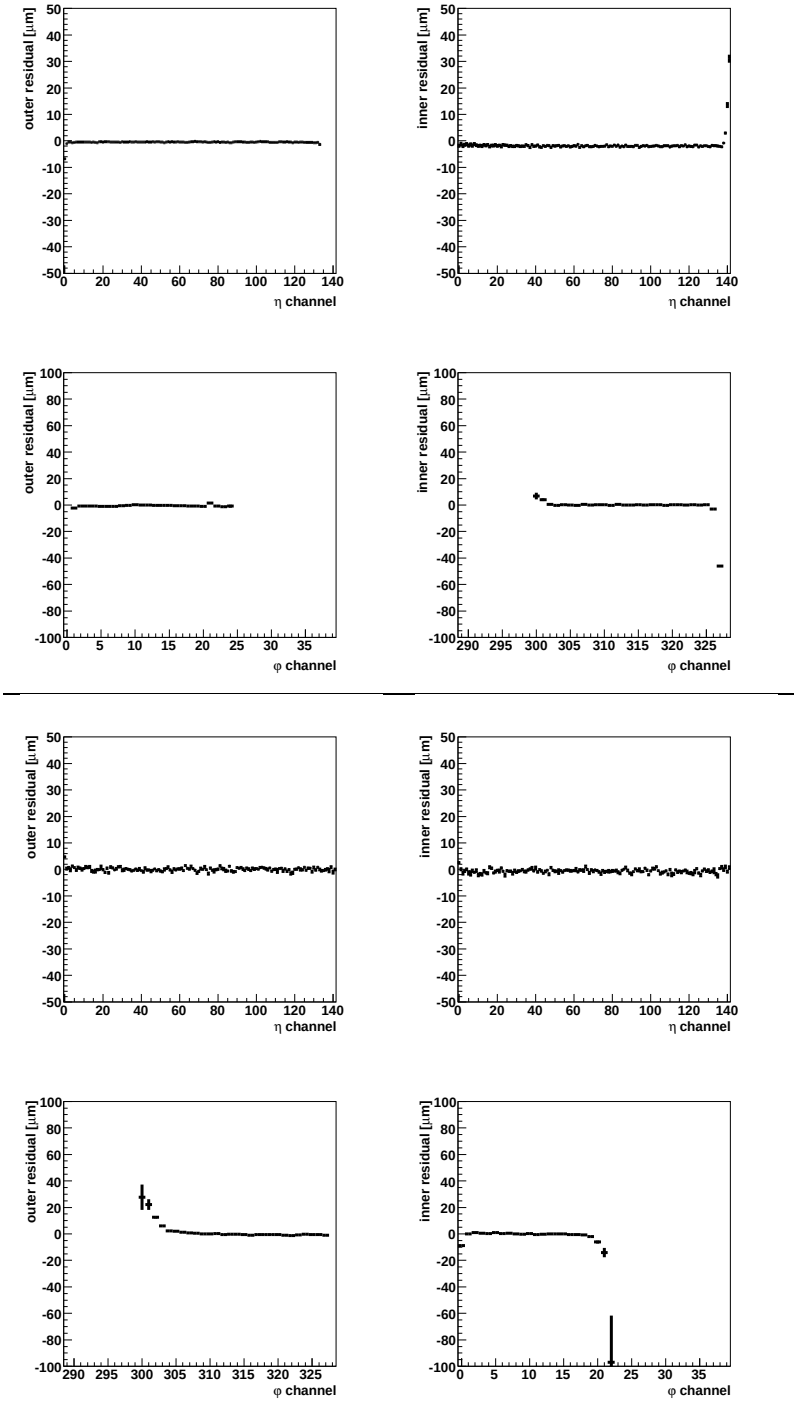

Figure A.10.: Comparison of residuals versus module coordinate as profiles for the toy MC of digitisation **(top)** and ATHENA **(bottom)**. All plots agree very well.

A.4. Impact of the Global Deformations on SCT Layer 0

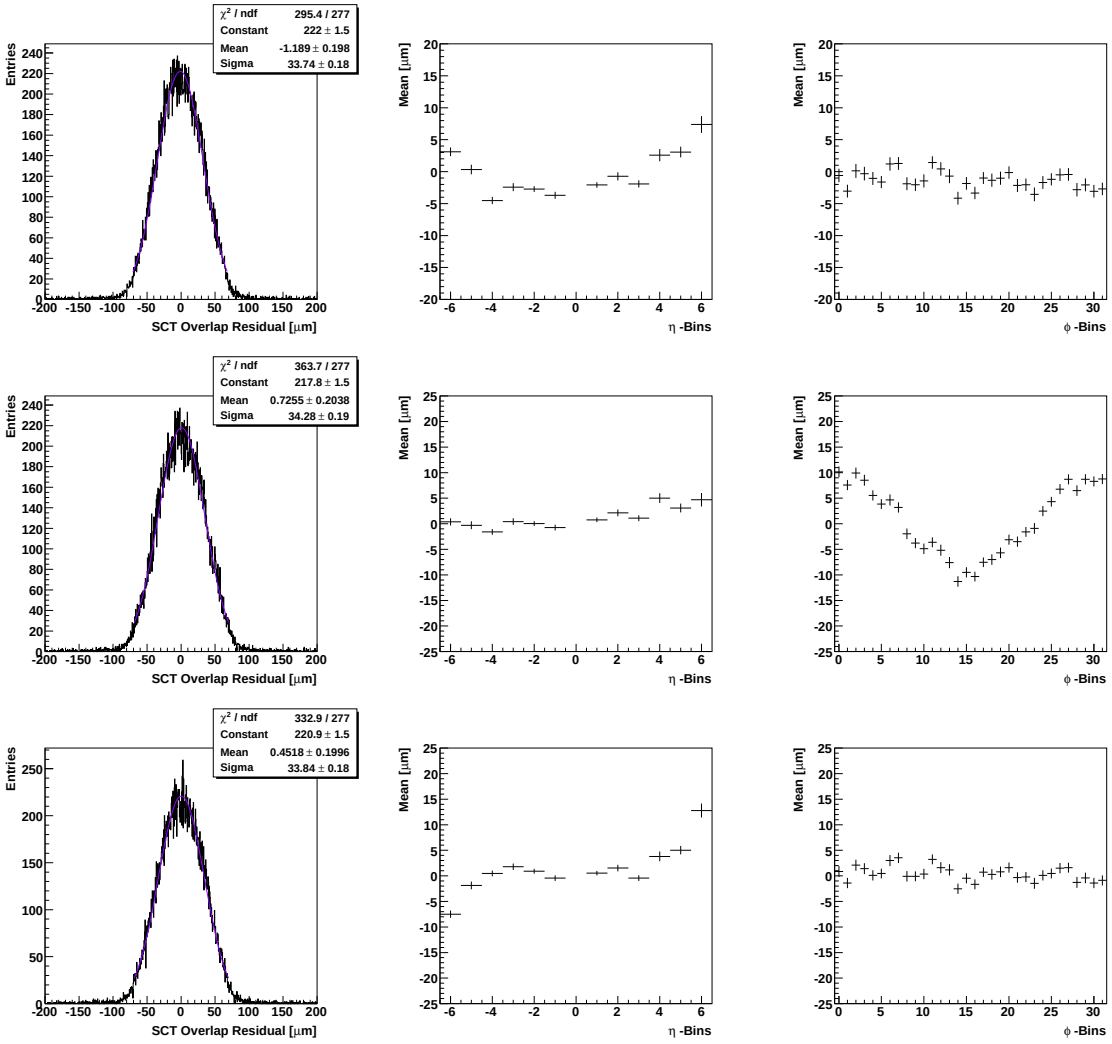

Figure A.11.: Impact of the angular dependent global deformations on SCT layer 0 exemplarily. **Top:** R-$\Delta\varphi$ **Middle:** φ-$\Delta\varphi$. **Bottom:** Z-$\Delta\varphi$. **Left:** Overlap residuals of an entire barrel. **Middle:** Overlap residual versus module-η. **Right:** Overlap residuals versus module-φ. These deformations are reflected, as they influence the module-to-module distance.

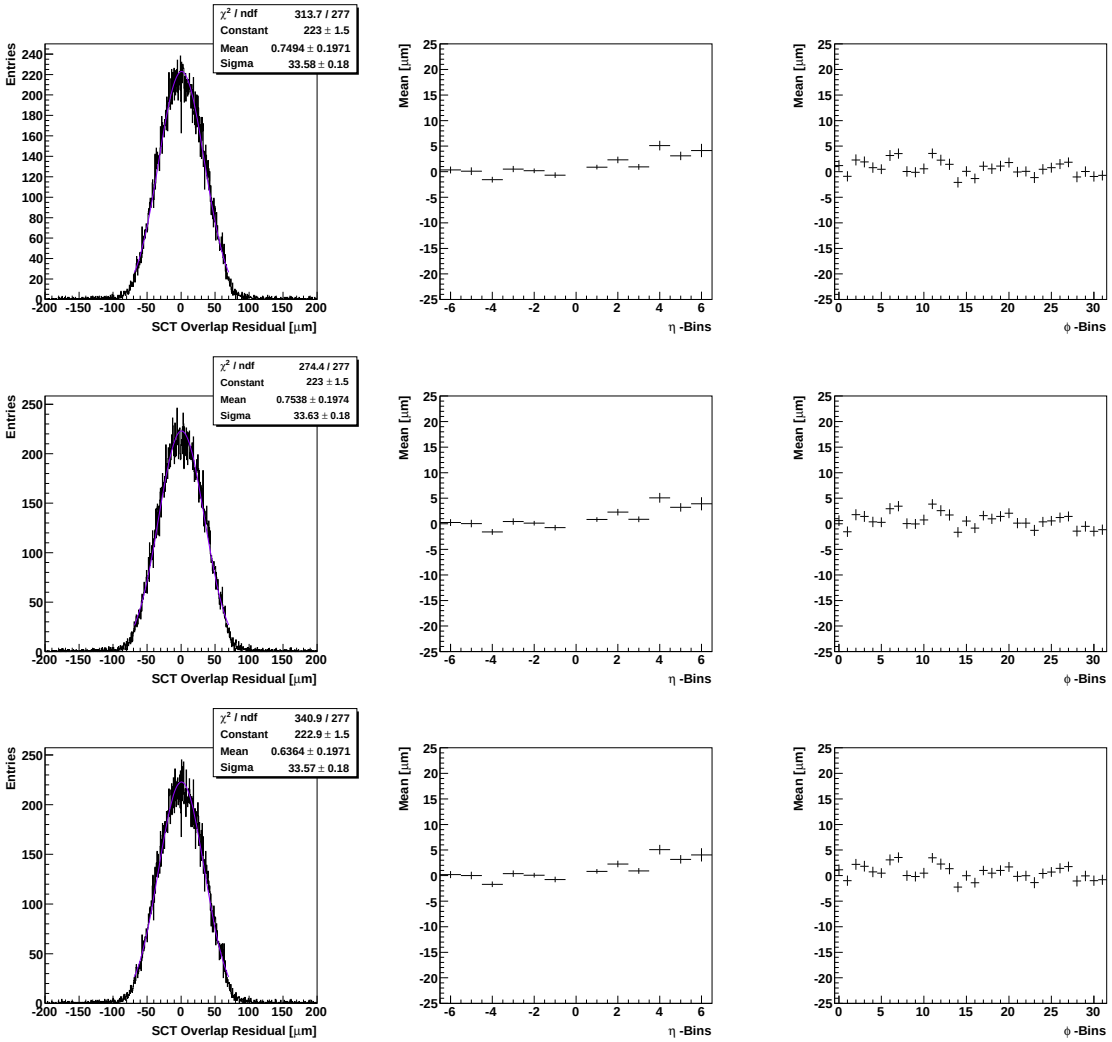

Figure A.12.: Impact of the z dependent global deformations on SCT layer 0 exemplarily. **Top:** R-ΔZ **Middle:** φ-ΔZ. **Bottom:** Z-ΔZ. **Left:** Overlap residuals of an entire barrel. **Middle:** Overlap residual versus module-η. **Right:** Overlap residuals versus module-φ. - None of these deformations is detected by R-φ overlap residuals, as they do not influence the R-φ distance of the modules.

B. List of Figures

Bibliography

[1] S. L. Glashow, *Partial Symmetries of Weak Interactions*, Nucl. Phys. **22** (1961) 579.

[2] S. Weinberg, *A Model of Leptons*, Phys. Rev. Lett. **19** (1967) 1264.

[3] A. Salam, *Elementary Particle Physics*, N. Svartholm, ed., Nobel Symposium No. 8, Almqvist & Wiksell, Stockholm.

[4] F. Halzen and A. D. Martin, *QUARKS AND LEPTONS: AN INTRODUCTORY COURSE IN MODERN PARTICLE PHYSICS*, New York, Usa: Wiley (1984) 396p.

[5] G. Kane, *The Dawn of Physics beyond the Standard Model*, Scientific American (2004) 53, Scientific American Exclusive Online Issue February 2004.

[6] P. W. Higgs, *Broken Symmetries, Massless Particles and Gauge Fields*, Phys. Lett. **12** (1964) 132.

[7] F. Englert and R. Brout, *Broken Symmetry and the Mass of Gauge Vector Mesons*, Phys. Rev. Lett. **13** (1964) 321.

[8] G. S. Guralnik, C. R. Hagen, and T. W. B. Kibble, *Global Conservation Laws and Massless Particles*, Phys. Rev. Lett. **13** (1964) 585.

[9] H. P. Nilles, *SUPERSYMMETRY, SUPERGRAVITY AND PARTICLE PHYSICS*, Phys. Rept. **110** (1984) 1.

[10] J. Wess and B. Zumino, *Supergauge Transformations in Four-Dimensions*, Nucl. Phys. **B70** (1974) 39.

[11] N. Arkani-Hamed, S. Dimopoulos, and G. R. Dvali, *The hierarchy problem and new dimensions at a millimeter*, Phys. Lett. **B429** (1998) 263, `hep-ph/9803315`.

[12] The ATLAS experiment - Mapping the Secrets of the Universe, www.atlasexperiments.org.

[13] Large Hadron Collider - LHC, lhc.web.cern.ch.

[14] O. Bruning *et al.*, *LHC design report. Vol. I: The LHC main ring*, CERN-2004-003-V-1.

[15] O. Bruning *et al.*, *LHC Design Report. 2. The LHC infrastructure and general services*, CERN-2004-003-V-2.

[16] CERN - European Organisation for Nuclear Research, www.cern.ch.

[17] The Lep Injector Study Group Collaboration, *LEP DESIGN REPORT. VOL. 1. THE LEP INJECTOR CHAIN*, CERN-LEP/TH/83-29.

[18] *LEP DESIGN REPORT: VOL. 2. THE LEP MAIN RING*, CERN-LEP-84-01.

[19] V. L. Ginzburg, L. D. Landau, *On the Theory of Superconductivity*, Zh. Eksp. Teor. Fiz. **20** (1950) 1064.

[20] The ATLAS Collaboration, W. W. Armstrong *et al.*, *ATLAS: Technical proposal for a general-purpose p p experiment at the Large Hadron Collider at CERN*, CERN-LHCC-94-43.

[21] The ATLAS Collaboration, *ATLAS: Detector and physics performance technical design report. Volume 1*, CERN-LHCC-99-14.

[22] The ATLAS Collaboration, *ATLAS detector and physics performance. Technical design report. Vol. 2*, CERN-LHCC-99-15.

[23] *CMS, the Compact Muon Solenoid: Technical proposal*, CERN-LHCC-94-38.

[24] The CMS Collaboration, G. L. Bayatian *et al.*, *CMS technical design report, volume II: Physics performance*, J. Phys. **G34** (2007) 995.

[25] The CMS Collaboration, G. L. Bayatian *et al.*, *CMS physics: Technical design report*, CERN-LHCC-2006-001.

[26] *ALICE: Technical proposal for a large ion collider experiment at the CERN LHC*, CERN-LHCC-95-71.

[27] The LHCb Collaboration, S. Amato *et al.*, *LHCb technical proposal*, CERN-LHCC-98-04.

[28] The LHCb Collaboration, *LHCb technical design report: Reoptimized detector design and performance*, CERN-LHCC-2003-030.

[29] The LHCf Collaboration, O. Adriani *et al.*, *Technnical proposal for the CERN LHCf experiment: Measurement of photons and neutral pions in the very forward region of LHC*, CERN-LHCC-2005-032.

[30] The LHCf Collaboration, O. Adriani *et al.*, *Technical design report of the LHCf experiment: Measurement of photons and neutral pions in the very forward region of LHC*, CERN-LHCC-2006-004.

[31] The TOTEM Collaboration, V. Berardi *et al.*, *TOTEM: Technical design report. Total cross section, elastic scattering and diffraction dissociation at the Large Hadron Collider at CERN*, CERN-LHCC-2004-002.

[32] The TOTEM Collaboration, V. Berardi *et al.*, *TOTEM: Technical design report - Addendum. Total cross section, elastic scattering and diffraction dissociation at the Large Hadron Collider at CERN*, CERN-LHCC-2004-020.

[33] I. Bird *et al.*, *LHC computing Grid. Technical design report*, CERN-LHCC-2005-024.

[34] D. Froidevaux and M. Vincter, *ATLAS Detector Paper - Draft 4*, (2008).

[35] S. Haywood, *Local Coordinate Frames for the Alignment of Silicon Detectors*, Tech. Rep. ATL-COM-INDET-2004 and ATL-INDET-2004-001, RAL, (July 2004).

[36] R. Schaffer and S. C. M. Bentvelsen, *Definition of Offline Readout Identifiers for the ATLAS detector*, Tech. Rep. ATL-SOFT-2001-004, CERN, Geneva, (Feb 2001), revised version number 1 submitted on 2001-05-28 13:21:00.

[37] The ATLAS Collaboration, *ATLAS inner detector: Technical design report. Vol. 1*, CERN-LHCC-97-16.

[38] The ATLAS Collaboration, *ATLAS inner detector: Technical design report. Vol. 2*, CERN-LHCC-97-17.

[39] The ATLAS Collaboration, *ATLAS magnet system: Technical design report*, CERN-LHCC-97-18.

[40] The ATLAS Collaboration, *ATLAS central solenoid: Technical design report*, CERN-LHCC-97-21.

[41] *Atlantis - Event display for ATLAS*, http://www.cern.ch/atlantis.

[42] The ATLAS Collaboration, M. S. Alam *et al.*, *ATLAS pixel detector: Technical design report*, CERN-LHCC-98-13 and CERN-LHCC-97-16.

[43] D. Dobos, *Production accompanying testing of the ATLAS Pixel module*, http://e4.physik.uni-dortmund.de/pub/EIV/Vortr

[44] The ATLAS Collaboration, *ATLAS tile calorimeter: Technical design report*, CERN-LHCC-96-42.

[45] The ATLAS Collaboration, *ATLAS liquid argon calorimeter: Technical design report*, CERN-LHCC-96-41.

[46] The ATLAS Collaboration, *ATLAS barrel toroid: Technical design report*, CERN-LHCC-97-19.

[47] The ATLAS Collaboration, *ATLAS end-cap toroids: Technical design report*, CERN-LHCC-97-20.

[48] The ATLAS Collaboration, *ATLAS muon spectrometer: Technical design report*, CERN-LHCC-97-22.

[49] ATLAS Level-1 Trigger Group, *Level-1 Trigger Technical Design Report*, (1998).

[50] ATLAS HLT/DAQ/DCS Group, *High-Level Trigger, Data Acquisition and Controls Technical Design Report*, (2003).

[51] CERN, *Proceedings of the first LHC Detector Alignment Workshop*, Geneva, (2007), CERN, Alignment Yellow Book CERN-2007-004.

[52] T. Golling, *Alignment of the silicon tracking detector using survey constraints*, ATL-INDET-2006-001.

[53] S. M. Gibson, *Monitoring the Heart of ATLAS using Frequency Scanning Interferometry*, Contributed to 8th International Workshop On Accelerator Alignment (IWAA 2004), Geneva, Switzerland, 4-7 Oct 2004.

[54] F. Heinemann, *Robust track based alignment of the ATLAS silicon detectors and assessing parton distribution uncertainties in Drell-Yan processes*, CERN-THESIS-2007-075.

[55] R. Härtel, *Iterative local χ^2 alignment approach for the ATLAS SCT detector*, Ph.D. thesis, Max-Plack-Institut für Physik, München, ("2005"), MPP-2005-174.

[56] P. Bruckmann de Renstrom *et al.*, ATL-INDET-PUB-2005-002.

[57] I. S. Duff *et al.*, *MA27 - a set of Fortran subroutines for solving sparse symmetric sets of linear equations*, AERE Harwell Laboratory, Harwell UK, 1982, Report R-10533.

[58] P. Bruckman de Renstrom, *Alignment strategy for the ATLAS tracker*, Nucl. Instrum. Meth. **A582** (2007) 800.

[59] F. Heinemann, *Track Based Alignment of the ATLAS Silicon Detectors with the Robust Alignment Algorithm*, `arXiv:0710.1166 [physics.ins-det]`.

[60] D. Hindson, *A Robust Procedure For Alignment Of The ATLAS Inner Detector Using Tracks*.

[61] T. Göttfert, *Iterative local χ^2 alignment approach for the ATLAS pixel detector*, Ph.D. thesis, Max-Plack-Institut für Physik, München, (2006), MPP-2006-118.

[62] D. N. Brown, *BaBar Si Tracker Alignment*, 1st LHC Detection Alignment Workshop 4-6 Sep 2006, Geneva, Switzerland.

[63] S. Blusk *et al.*, *Proceedings of the first LHC Detector Alignment Workshop, CERN, Geneva, Switzerland, 4-6 September 2006*, 1st LHC Detection Alignment Workshop 4-6 Sep 2006, Geneva, Switzerland.

[64] G. Duckeck *et al.*, *ATLAS computing: Technical design report*, CERN-LHCC-2005-022.

[65] R. Brun and F. Rademakers, *ROOT - An Object Oriented Data Analysis Framework*, Proceedings AIHENP'96 Workshop, Lausanne, Sep. 1996, Nucl. Inst. & Meth. in Phys. Res. A 389 (1997) 81-86. See also http://root.cern.ch.

[66] *Documentation of the Inner Detector Software packages*, https://twiki.cern.ch/twiki/bin/view/Atlas/InDetPackageDocumentation.

[67] *TWiki of PixelDigitisation*, https://twiki.cern.ch/twiki/bin/view/Atlas/PixelDigitization.

[68] *TWiki of SCTDigitisation*, https://twiki.cern.ch/twiki/bin/view/Atlas/SCTDigitizationPackage.

[69] E. Moyse and M. Elsing, *TWiki of InDetRecExample*, https://twiki.cern.ch/twiki/bin/view/Atlas/InDetRecExample.

[70] *TWiki of InDetLocalChi2AlignAlgs*, https://twiki.cern.ch/twiki/bin/view/Atlas/InDetLocalChi2AlignAlgs.

[71] T. Nikitina, F. Bergsma, and J. M. CROLET, *A program to calculate the ATLAS Magnetic field*, ATL-MAGNET-2001-001, ATL-MAGNET-2001-002 and ATL-MAGNET-2003-001.

[72] *TWiki of InnerDetectorVisualisationTool*, https://twiki.cern.ch/twiki/bin/view/Atlas/IDAlignVisualization.

Acknowledgements

The last page is dedicated to all those contributing to an Happy End of my diploma thesis.

First of all I would like to thank Prof. A. Quadt for giving me the possibility to write this diploma thesis and being part of his new group in Göttingen from the very first day. I want to say *thank you* for your steady encouragements and your individual supervision.

I wish to acknowledge Prof. Markus Klute for being so kind to take over the burden of coreferee.

Besides, I am deeply grateful to Dr. Jörn Grosse-Knetter and Dr. Kevin Kröninger for their continuous inspiring conversations and sagacious advice during my studies and finally the extensive and diligent proofreading of this thesis.

I feel thankful to Dr. Michael Uhrmacher for his support and caring encouragement. He helped me patiently throughout the whole time. Furthermore, I am especially grateful for the advice and support of my dear colleages, especially Fabian Kohn and Matthias Stein. You know who else...

Last but not least I would like to thank my family, particularly my parents and my brother, for their love, confidence, patience and their generous support during every time of my life - not to forget Askan ;-)